Inverse Problems in Structural Mechanics

by
Jing Li

Dissertation submmitted to the Faculty of
Virginia Polytechnic Institute and State University
in partial fulfillment of the requirements for the degree of

Doctor of Philosophy
in
Aerospace Engineering

Advisory Committee

Rakesh K. Kapania, Chairman
Romesh C. Batra
Raymond H. Plaut
Robert L. West
Mayuresh Patil

December 2005
Blacksburg, Virginia

Keywords: inverse problems, unitized structures, load updating, finite element models, fiber optic sensors, placement optimization, genetic algorithms, panel optimization

Inverse Problems in Structural Mechanics

Jing Li

Virginia Polytechnic Institute and State University
Blacksburg, VA 24061-0203

(ABSTRACT)

This dissertation deals with the solution of three inverse problems in structural mechanics. The first one is load updating for finite element models (FEMs). A least squares fitting is used to identify the load parameters. The basic studies are made for geometrically linear and nonlinear FEMs of beams or frames by using a four-noded curved beam element, which, for a given precision, may significantly solve the ill-posed problem by reducing the overall number of degrees of freedom (DOF) of the system, especially the number of the unknown variables to obtain an overdetermined system. For the basic studies, the unknown applied load within an element is represented by a linear combination of integrated Legendre polynomials, the coefficients of which are the parameters to be extracted using measured displacements or strains. The optimizer L-BFGS-B is used to solve the least squares problem.

The second problem is the placement optimization of a distributed sensing fiber optic sensor for a smart bed using Genetic Algorithms (GA), where the sensor performance is maximized. The sensing fiber optic cable is represented by a Non-uniform Rational B-Splines (NURBS) curve, which changes the placement of a set of infinite number of the infinitesimal sensors to the placement of a set of finite number of the control points. The sensor performance is simplified as the integration of the absolute curvature change of the fiber optic cable with respect to a perturbation due to the body movement of a patient. The smart bed is modeled as an elastic mattress core, which supports a fiber optic sensor cable. The initial and deformed geometries of the bed due to the body weight of the patient are calculated using MSC/NASTRAN for a given body pressure. The deformation of the fiber optic cable can be extracted from the deformation of the mattress. The performance of the fiber optic sensor for any given placement is further calculated for any given perturbation.

The third application is stiffened panel optimization, including the size and placement optimization for the blade stiffeners, subject to buckling and stress constraints. The present work uses NURBS for the panel and stiffener representation. The mesh for the panel is generated using DistMesh, a triangulation algorithm in MATLAB. A NASTRAN/MATLAB interface is developed to automatically transfer the data between the analysis and optimization processes respectively. The optimization consists of minimizing the weight of the stiffened panel with design variables being the thickness of the plate and height and width of the stiffener as well as the placement of the stiffeners subjected to buckling and stress constraints under in-plane normal/shear and out-plane pressure loading conditions.

Dedication

To the Almighty God Father, and His Son Jesus Christ;
To my parents, Zhenyu Li and Yulan Che,
To my mother-in-law, Guilan Zhang,
To my wife, Xiuli Lu,
To my daughters, Suo Li and Rebekah Li

"I can do all things in Christ who strengthens me..."
– BIBLE: Phillipians 4:13

Acknowledgments

I am grateful to my advisor, Dr. Rakesh K. Kapania, for giving me a valuable opportunity to work with him and to gain broad experience through many exciting projects, and for his valuable support and encouraging advice throughout the program. I also want to express my gratefulness to Drs. Raymond H. Plaut, Romesh C. Batra, Robert L. West and Mayuresh Patil for serving as committee members and giving me valuable input through the committee meetings or course work.

I have been so fortunate to have my parents, Zhenru Li and Yulan Che, my mother-in-law Guilan Zhang, and deeply grateful for their unchanging love and support. I want to express my deep thanks to my wife, Xiuli Lu, for her precious love, encouragement, and sacrifice, and my daughters, Suo and Rebekah, for their everlasting smile and good health.

Thanks are also due to many colleagues in our department throughout the program for their valuable company and encouragement, especially to Yong Yook Kim, Jeffrey M.K. Chock, Dhaval Makhecha, Sameer Mulani, Sumit Vasudeva, Hazem Soliman, and Hitesh Kapoor.

I also want to acknowledge the financial support through all years for my studies and researches from the project sponsored by a grant (CDAAH04-95-1-0175) from the Army Research Office with Dr. Gary Anderson as the grant monitor, from the project of Java Applets for Engineering Education funded by the National Science Foundation, from the assistance and funding of ADOPTECH, Inc., of Blacksburg, Virginia, through Dr. Scott Ragon, from the project funded by Virginia Tech Applied Biosciences Center (VT ABC) at Virginia Polytechnic Institute and State University through Dr. William Spillman, Jr., and from the project funded from NASA Langley and the National Institute of Aerospace for funding the project with Drs. Davis Brake, and Karen Taminger as grant monitors. Finally and uttermost, I'd thank the Almighty God and His Christ Jesus for the salvation and spiritual comfort during my hardest time.

God bless you and thank you all,

Jing Li

Table of Contents

Title Page 1

Abstract ii

Dedication iii

Acknowledgements iv

Table of Contents v

List of Figures viii

List of Tables xiv

Introduction 1
- 1.1 Inverse Problems 1
- 1.2 Regularization Methods 5
- 1.3 Present Work 9

Load Updating for Finite Element Models 11
- 2.1 An Overview 12
- 2.2 Theory 18
  - 2.2.1 Load Representation within an Element 18
  - 2.2.2 Load Updating for Nonlinear FEM 19
  - 2.2.3 Constraints on Load Distribution 23
- 2.3 Examples 26
  - 2.3.1 The Effect of Measurement Methods: Absolute Error and Relative Error 28
  - 2.3.2 The Effect of the Order of Integrated Legendre Polynomials 30
  - 2.3.3 The Effect of Element Size 32
  - 2.3.4 The Effect of Density of Measured Points 34
  - 2.3.5 The Effect of Enforcing Smoothing and C^0 Continuity 36
  - 2.3.6 An Application to a Portal Frame 37
  - 2.3.7 An Application to Highly Oscillating Load Updating 38
  - 2.3.8 Measured Strains Based Load Updating 40
  - 2.3.9 An Application to Geometrically Nonlinear Beam 40
- 2.4 Conclusions 45

Placement Optimization of Fiber Optic Sensors **48**
3.1 An Overview 49
3.2 Description of the Problem 53
  3.2.1 Objective/Sensor Performance Function 53
  3.2.2 Design Variables/Placement Representation 54
  3.2.3 Constraints 56
3.3 Procedure and Implementation 57
  3.3.1 Procedure 57
  3.3.2 Implementation 61
3.4 Placement Optimization of the Fiber Optic Sensors for a Smart Bed by GA . 62
  3.4.1 A Very Simple Breeding Algorithm 62
  3.4.2 Coding/Decoding 63
  3.4.3 Fitness Function 64
  3.4.4 Examples 65
3.5 Conclusions 67

Optimal Design of Unitized Panels with Curvilinear Stiffeners **71**
4.1 An Overview 71
4.2 Methodology, Procedure, and Capability 73
  4.2.1 Methodology 73
  4.2.2 Procedure 74
  4.2.3 Capability and Limitation 75
4.3 Mathematical Aspects of Optimization of Stiffened Panels 75
  4.3.1 Formulation of Optimization of Stiffened Panels 75
  4.3.2 Convergence of Optimization of Stiffened Panels 76
  4.3.3 NURBS Representation of Stiffened Panels 79
  4.3.4 Finite Element Meshing and Mapping 82
4.4 Numerical Studies on Optimal Blade Stiffened Panel Designs 82
  4.4.1 Orientation Effects 84
  4.4.2 Spacing Effects 88
  4.4.3 Location Effects 88
  4.4.4 Curvature Effects 88
4.5 Conclusions and Future Work 106

Summary and Conclusions **119**

Legendre Polynomials **124**

Load Coefficient Matrix at the Element Level **126**

The Derivatives of the Displacements with Respective to Load Coefficient Vector 130

The Derivatives of the Strains with Respect to Load Coefficient Vector 132

References 134

Vita 142

List of Figures

Figure 1.1 A spring-mass-damper system.. 2
Figure 2.1 Load distribution within an element as a linear combination of integrated Legendre polynomials.. 20
Figure 2.2 A need for constraints on the extracted load.. 25
Figure 2.3 A comparison of the extracted loads for a cantilever beam with absolute or relative error between the calculated and measured displacements at 9 points. The applied reference load was uniformly distributed and the extracted load within an element was also assumed to be uniformly distributed. Eight four-noded curved beam elements were used to model the beam. The extracted load with relative error of displacements was closer to the applied reference load than that with absolute error of displacements.. 29
Figure 2.4 Extracted load for a cantilever beam subjected to a uniform reference load as a function of number of integrated Legendre polynomials. Polynomials up to degree 3 extracted the load perfectly. Higher-order polynomials gave a relatively large oscillating error around the reference load.. 31
Figure 2.5 Extracted load for a cantilever beam as a function of number of elements. The load within each element was assumed to be uniformly distributed. 33
Figure 2.6 Extracted load for a cantilever beam as a function of number of measured points. The applied reference load was uniformly, linearly or Sinusoidally distributed, but the load within each of the elements was assumed to be uniformly distributed.. 35
Figure 2.7 Constraining the extracted load through the enforcement of load smoothing within an element and C^0 between two adjacent elements: $\lambda_S, \lambda_{C^0} = 1 \times 10^3$ continuity. The applied reference load was linearly distributed but a linear combination of first 4 integrated Legendre polynomials (highest degree is 3) was used to represent the load distribution over an element for load extraction. Eight elements were used to model the beam.. 37
Figure 2.8 Extracting in-plane and out-plane loads for a portal frame.. 38

Figure 2.9 Extracting highly oscillating load for a cantilever beam. The applied reference load (RL) was sinusoidally distributed with unit mean value. The extracted load (EL) was assumed uniformly distributed within an element. (a) The RL had 3 sine waves. 60 elements were used. The EL agreed well with the RL. (b) The RL had 6 sine waves. 120 elements were used. The EL agreed well with the RL at first 3 sine waves near the fixed end but tended to be close to the unit mean value of the RL at the other 3 sine waves near the free end. (c) The applied load had 12 sine waves and unit mean value. 240 (120) elements were used. The EL agreed well with the RL at only 1.5 sine waves near the fixed end but tended to be close to the unit mean value of the RL near the free end. Results using both 120 and 240 elements are almost identical.. 39

Figure 2.10 Extracting loads of different distributions for a cantilever beam with measured bending strains at 3 Gaussian points in each of the 8 elements. Load within each element was assumed to be uniform.. 41

Figure 2.11 Extracting uniform self-weight type load for a cantilever beam. Eight finite elements were used to model the beam.. 43

Figure 2.12 Extracting uniform snow loads of type II-n (non-conservative consideration) as compared with type II-c (conservative consideration) for a cantilever beam. Eight finite elements were used to model the beam.. 44

Figure 2.13 Extracting uniform pressure load for a cantilever beam with different choices of displacement measurements. Eight finite elements were used. The unknown axial displacements are set to zero in the figure. The TD were measured at all the 25 nodes. TD: transverse displacements; RL: reference load; AD: axial displacements. DS: design stepsize; LUI: load updating iterations.. 46

Figure 3.1 A schematic diagram of the smart bed. The distributed sensing fiber optic cable is stitched on the bed surface.. 52

Figure 3.2 A possible fiber optic sensor placement represented by a NURBS curve.. 55

Figure 3.3 Chart for optimal placement of the fiber optic sensor.. 58

Figure 3.4 Body pressure and deformation of the soft cored mattress. The pressure P has a unit of N/cm^2.. 60

Figure 3.5 A placement of a fiber optic sensor for a smart bed represented by a NURBS curve with 6 control points. Adopted from Fig. 3.7b.. 63

Figure 3.6 Placement optimization of a fiber optic sensor for a smart bed by GA.. . 65

Figure 3.7 A 3-D view of the initial placement and updated placement. The perturbed (dashed) and unperturbed (solid) fiber curve shapes of the optimal placement of the fiber optic sensor. 68

Figure 3.8 Placement optimization of a fiber optic sensor for a smart bed by GA.. . 69

Figure 3.9 A 3-D view of the initial placement and updated placement. The perturbed (dashed) and unperturbed (solid) fiber curve shapes of the optimal placement of the fiber optic sensor.. 70
Figure 4.1 A curved panel with arbitrarily oriented stiffeners and its finite element mesh.. 73
Figure 4.2 NURBS representation for stiffeners' reference curves.. 80
Figure 4.3 NURBS representation for panel's reference surface.. 80
Figure 4.4 The meshing and mapping of a stiffened panel with a central hole.. . . . 83
Figure 4.5 Geometrical dimensions ($a = 2.54$m; $b = 2.54$m), pure shear loading ($Q_{\mathrm{xy}} = 250$kN/m), and simply supported conditions of a blade stiffened panel. Both stiffeners and plate are made out of aluminum. Initial size and bounds: $t_0 = w_0 = 0.005$m; $h_0 = 5w_0$; $t_{\mathrm{b}} = w_{\mathrm{b}} = [0.0001, 0.1]$m; $h_{\mathrm{b}} = [0.0001, 0.5]$m.. . . . 85
Figure 4.6 Effects of orientations of the stiffeners on the optimal designs. Orientation I: $M_{\mathrm{min}} = 224$kg.. 86
Figure 4.7 Effects of orientations of the stiffeners on the optimal designs. Orientation II: $M_{\mathrm{min}} = 144$kg.. 87
Figure 4.8 Effects of spacing of the stiffeners on the optimal designs. Spacing II: $M_{\mathrm{min}} = 101$kg.. 89
Figure 4.9 Effects of location of the stiffeners on the optimal designs. Location I: $M_{\mathrm{min}} = 144$kg; Location II: $M_{\mathrm{min}} = 186$kg.. 90
Figure 4.10 One design parameter α controls the motions of two mid control points $\mathbf{x^1}$ and $\mathbf{x^2}$ starting from $\mathbf{x_0^1}$ and $\mathbf{x_0^2}$ and by $\alpha\mathbf{d^1}$ and $\alpha\mathbf{d^2}$ for stiffeners 1 and 2, respectively.. 92
Figure 4.11 Effects of curvature of the stiffeners on the optimal designs. $\alpha = -0.3$: $M_{\mathrm{min}} = 240$kg.. 93
Figure 4.12 Effects of curvature of the stiffeners on the optimal designs. $\alpha = 0.0$: $M_{\mathrm{min}} = 220$kg.. 94
Figure 4.13 Effects of curvature of the stiffeners on the optimal designs. $\alpha = 0.8$: $M_{\mathrm{min}} = 178$kg.. 95
Figure 4.14 Diagram of minimum mass vs. shape design parameter α. Two minima are found. One corresponds to straight stiffeners at about $\alpha = 0.0$ with minimum mass $M_{\mathrm{min}} = 220$kg. The global optimal shape corresponds to curvilinear stiffeners at about $\alpha = 0.8$ with a minimum mass $M_{\mathrm{min}} = 178$kg, which is the minimum of the two minima.. 96

Figure 4.15 Geometrical dimensions ($a = 2.54$m; $b = 2.54$m), bi-normal loading ($N_{\mathrm{x}} = 250$kN/m; $N_{\mathrm{y}} = 0.2N_{\mathrm{x}}$), and simply-supported conditions of a blade stiffened panel. Both stiffeners and plate are made out of aluminum. Initial size and bounds: $t_0 = w_0 = 0.005$m; $h_0 = 5w_0$; $t_{\mathrm{b}} = w_{\mathrm{b}} = [0.0001, 0.1]$m; $h_{\mathrm{b}} = [0.0001, 0.5]$m.. 97

Figure 4.16 Location 1: The end points of the two stiffeners are close to the upper/lower edges of the panel and $13/15b$ apart from each other. One design parameter α controls the motions of two mid control points $\mathbf{x^1}$ and $\mathbf{x^2}$ starting from $\mathbf{x_0^1}$ and $\mathbf{x_0^2}$ and by $\alpha_1\mathbf{d^1}$ and $\alpha_2\mathbf{d^2}$ for stiffeners 1 and 2, respectively.. . . . 98

Figure 4.17 Location I: effects of curvature of the stiffeners on the optimal designs.. . 99

Figure 4.18 Location I: Diagram of minimum mass vs. shape design parameter α. The global optimal shape is achieved at about $\alpha = 1.60$ with a minimum mass $M_{\mathrm{min}} = 245$kg. The maximum number of iterations for size optimization is set to be 50 and 100.. 100

Figure 4.19 Location II: The end points of the two stiffeners are close to the upper/lower edges of the panel and $7/15b$ apart from each other. One design parameter α controls the motions of two mid control points $\mathbf{x^1}$ and $\mathbf{x^2}$ starting from $\mathbf{x_0^1}$ and $\mathbf{x_0^2}$ and by $\alpha_1\mathbf{d^1}$ and $\alpha_2\mathbf{d^2}$ for stiffeners 1 and 2, respectively. Also see Fig. 4.16.. 101

Figure 4.20 Location II: Diagram of minimum mass vs. shape design parameter α. The global optimal shape is achieved at about $\alpha = 0.10$ with a minimum mass $M_{\mathrm{min}} = 197$kg (compared with straight stiffeners $\alpha = 0.0$ with $M_{\mathrm{min}} = 205$kg). The maximum number of iterations for size optimization is set to be 100.. . . . 102

Figure 4.21 Location III: The end points of the two stiffeners are close to the upper/lower edges of the panel and $5/15b$ apart from each other. One design parameter α controls the motions of two mid control points $\mathbf{x^1}$ and $\mathbf{x^2}$ starting from $\mathbf{x_0^1}$ and $\mathbf{x_0^2}$ and by $\alpha_1\mathbf{d^1}$ and $\alpha_2\mathbf{d^2}$ for stiffeners 1 and 2, respectively. Also see Fig. 4.16.. 103

Figure 4.22 Location 3: Diagram of minimum mass vs. shape design parameter α. The global optimal shape is achieved at about $\alpha = 0.0$ with a minimum mass $M_{\mathrm{min}} = 185$kg. The maximum number of iterations for size optimization is set to be 100.. 104

Figure 4.23 One design parameter α controls the shapes of the NURBS curves of four stiffeners, which are initially straight ($\alpha = 0.0$) and evenly spaced.. 105

Figure 4.24 A comparison of diagrams of minimum mass vs. shape design parameter α before and after the improvement of the convergence. After the improvement of the convergence, three local minima are found. One corresponds to straight stiffeners at about $\alpha = 0.0$ with a minimum mass $M_{\text{min}} = 213$kg which is also the global minimum. The other two local minima correspond to curvilinear stiffeners at about $\alpha = 0.275$ with a minimum mass $M_{\text{min}} = 223$kg, and at about $\alpha = 0.875$ with a minimum mass $M_{\text{min}} = 235$kg.. 106
Figure 4.25 A comparison of optimal designs before and after the improvement of the convergence.. 107
Figure 4.26 A comparison of the first four buckling modes before and after the improvement of the convergence.. 108
Figure 4.27 A comparison of the design histories before and after the improvement of the convergence.. 109
Figure 4.28 One design parameter α controls the shapes of the NURBS curves of four stiffeners, which are initially straight ($\alpha = 0.0$) and evenly spaced.. 110
Figure 4.29 Variation of minimum mass vs. shape design parameter α. The global optimal shape is achieved at about $\alpha = 0.0$ with a minimum mass $M_{\text{min}} = 190$kg. An inclusion of a central hole of radius 0.3m results in curvilinear stiffeners as the global optimal placement, achieved at about $\alpha = -0.0725$ with a minimum mass $M_{\text{min}} = 182$kg.. 111
Figure 4.30 A comparison of optimal designs before and after the inclusion of the central cutout of radius 0.3m.. 112
Figure 4.31 A comparison of first four buckling modes before and after the inclusion of the central cutout of radius 0.3m.. 113
Figure 4.32 A comparison of design histories before and after the inclusion of the central cutout of radius 0.3m.. 114
Figure 4.33 Geometrical dimensions ($a = 2.54$m; $b = 2.54$m), bi-normal and shear loading ($N_{\text{x}} = 250$kN/m; $N_{\text{y}} = 0.2N_{\text{x}}$; $Q_{\text{xy}} = 0.5N_{\text{x}}$; $P_{\text{y}} = 0$), and simply supported conditions of a blade stiffened panel. Both stiffeners and plate are made out of aluminum. Initial size and bounds: $t_0 = w_0 = 0.005$m; $h_0 = 5w_0$; $t_{\text{b}} = w_{\text{b}} = [0.0001, 0.1]$m; $h_{\text{b}} = [0.0001, 0.5]$m.. 115
Figure 4.34 Design parameter α_1 controls the motions of two mid control points $\mathbf{x^1}$ and $\mathbf{x^2}$ starting from $\mathbf{x_0^1}$ and $\mathbf{x_0^2}$ by $\alpha_1\mathbf{d_1^1}$ and $\alpha_1\mathbf{d_1^2}$ for stiffeners 1 and 2, respectively. Design parameter α_2 controls the motions of two mid control points $\mathbf{x^3}$ and $\mathbf{x^4}$ starting from $\mathbf{x_0^3}$ and $\mathbf{x_0^4}$ by $\alpha_2\mathbf{d_2^3}$ and $\alpha_2\mathbf{d_2^4}$ for stiffeners 3 and 4, respectively.. . 115

Figure 4.35 Design space of two design parameters: $\alpha_1 = X$ and $\alpha_2 = Y$, with corresponding minimum mass: $M_{\text{min}} = Z$. Two local minima are found as shown as the dark squares inside the circles from 17 discrete points on the 11×11 grids. The maximum number of iterations for size optimization is set to be 100.. 116
Figure 4.36 Two local minima vs. two design parameters.. 117
Figure 4.37 First four buckling modes for minimum 1 and minimum 2.. 118

List of Tables

Table 2.1 $E_{\mathrm{load}}^{\mathrm{Ext}}$ vs. absolute and relative displacement measurements.. 30
Table 2.2 $E_{\mathrm{load}}^{\mathrm{Ext}}$ vs. the degree of Integrated Legendre polynomial within one element.. 31
Table 2.3 $E_{\mathrm{load}}^{\mathrm{Ext}}$ vs. the number of elements (N_{elm}).. 32
Table 2.4 $E_{\mathrm{load}}^{\mathrm{Ext}}$ vs. the number of measured points (N_{m}).. 36
Table 3.1 Latex Mattress Core Fact Sheet.. 59
Table 3.2 Latex Mattress Core Fact Sheet.. 60

Chapter 1
Introduction

Driven by the needs from applications in both industry and other sciences, the field of inverse problems has undergone a tremendous growth during the last two decades (Engl and Kugler, 2003). However, studies on inverse problems in structural mechanics can be traced back to as far as 1904 when Michell (1904) dealt with the optimum layout of a plane truss. The work by Schmitt (1960) is frequently viewed as the start of modern structural optimization in the 1960's when computer-aided structural analysis and numerical optimization techniques became accessible. Though the studies on modern structural optimization has been undertaken for more than three decades, the terminology of inverse problems has not been widely used.

1.1 Inverse Problems

Inverse problems arise whenever one searches for causes of observed or desired effects (Engl and Kugler, 2003). Accordingly, direct or forward problems are to find the effects with given causes.

In the field of structural mechanics, the causes more often refer to structural and load parameters, and the effects are structural responses. Therefore, structural analysis for responses under given structures and loads are usually called direct or forward problems, while structural optimizations and identifications for structural and load parameters that cause the observed or desired responses are inverse problems.

To illustrate, refer Fig. 1.1 for a spring-mass-damper dynamic system, which can be described in the form of linear dynamic state equation, noticing the time t derivative notations: $\dot{x} = \frac{\partial x}{\partial t}$ and $\ddot{x} = \frac{\partial^2 x}{\partial t^2}$ for any entity x:

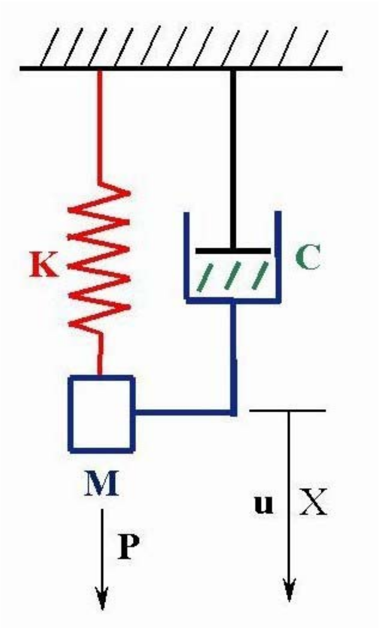

Figure 1.1: A spring-mass-damper system.

$$\mathbf{M}\ddot{\mathbf{u}} + \mathbf{C}\dot{\mathbf{u}} + \mathbf{K}\mathbf{u} = \mathbf{P} \tag{1.1}$$

with initial conditions for displacement $\mathbf{u}$ and velocity $\dot{\mathbf{u}}$:

$$\mathbf{u}|_{t=t_0} = \mathbf{u_0}; \quad \dot{\mathbf{u}}|_{t=t_0} = \mathbf{v_0} \tag{1.2}$$

Then, as examples, we can define one of the simplest forward problems as:

- **Forward problem 1**: Given the mass $\mathbf{M}$, damping $\mathbf{C}$, spring constant or system stiffness $\mathbf{K}$, initial conditions as in Eq. (1.2), and the external load $\mathbf{P}$, find the displacement response $\mathbf{u}$ for $t \geq t_0$.

and some inverse problems:

- **Inverse problem 1**: Given the displacement response $\mathbf{u}$ for $t \geq t_0$ and $\mathbf{v}_0$, and the external load $\mathbf{P}$, find the mass $\mathbf{M}$, damping $\mathbf{C}$, and system stiffness $\mathbf{K}$.
- **Inverse problem 2**: Given the displacement response $\mathbf{u}$ for $t \geq t_0$ and $\mathbf{v}_0$, as well as the mass $\mathbf{M}$, damping $\mathbf{C}$, and system stiffness $\mathbf{K}$, find the external load $\mathbf{P}$.

Inverse problem 1 is often viewed as a formulation of structural parameter identification (Trivailo et al., 2004) or structural model updating (Mottershead and Friswell, 1993; Friswell and Mottershead, 1995; Ahmadian et al., 1998; Avitabile, 2000). Inverse problem 2 is a formulation for load parameter identification or load updating (Chock and Kapania, 2003; Chock and Kapania, 2004).

Though many inverse problems in structural mechanics are formulated on the continuous setting, and evaluated on the discrete setting based on FEM or boundary element methods (BEM) (Bonnet and Constantinescu, 2005), both of the above inverse problem formulations are discrete formulations (Mroz and Garstecki, 2005) or based on discrete linear model equations (Hansen and O'Leary, 1993), for example, finite element models or methods (FEM) (Mottershead and Friswell, 1993; Friswell and Mottershead, 1995; Gladwelly, 1997; Avitabile, 2000; Chock and Kapania, 2003; Chock and Kapania, 2004; Maincon, 2004a; Maincon, 2004b; Maree and Maincon, 2004; Barnardo and Maincon, 2004; Trivailo et al., 2004; Mroz and Garstecki, 2005).

The solutions of most inverse problems lack uniqueness, which violates the *second* of the three Hadamard well-posed conditions (Engl and Kugler, 2003):

1. for all admissible data, a solution exists,
2. for all admissible data, the solution is unique and
3. the solution depends continuously on the data.

A violation of any of the three conditions (first two describe the identifiability and third one is about stability) makes the inverse problems ill-posed or ill-conditioned. Non-uniqueness is sometimes an advantage, and allows to choose among several strategies for a desired effect (Engl and Kugler, 2003). For instance, an infinite number of the solutions of inverse problems is useful in many design problems as it gives one the freedom to find the optimal solutions among all possible solutions when further desired effects, such as the requests to minimize or maximize some cost or objective function E subjected to certain constraints, are provided. Then, inverse problems 1 and 2 can be further formulated into two optimization problems:

- **Inverse problem 1a**: Given the displacement response $\mathbf{u}$ and other possible constraints for $t \geq t_0$ and $\mathbf{v}_0$, and the external load $\mathbf{P}$, find the optimal mass $\mathbf{M}$, damping $\mathbf{C}$, and system stiffness $\mathbf{K}$ to minimize or maximize $E = E(\mathbf{M}, \mathbf{C}, \mathbf{K})$
- **Inverse problem 2a**: Given the displacement response $\mathbf{u}$ and other possible constraints for $t \geq t_0$ and $\mathbf{v}_0$, as well as the mass $\mathbf{M}$, damping $\mathbf{C}$, and system stiffness $\mathbf{K}$, find the optimal external load $\mathbf{P}$ minimize or maximize $E = E(\mathbf{P})$.

Inverse problem 1a includes a conventional structural optimization formulation subjected to a constraint on the displacement response. Therefore, we have established the idea that structural optimization is a special application field of inverse problems in structural mechanics. Inverse problem 2a covers a seemingly new optimization formulation where the design variables are loads or load parameters, instead of structural parameters. In fact, actual load updating or identification is often formulated as some form of an optimization problem with load or load parameters as design variables employed to minimize, for example, the error between the given observed displacement response based on measurement and the calculated or predicted displacement response of a structural (FEM) model under an approximated load.

Mroz and Garstecki (2005) gave some interesting inverse problem formulations for optimal loading conditions in the design and identification of structures, which is a kind of mixed formulation of inverse problems 1a and 2a.

An inverse problem is not only often formulated as a numerical optimization problem, but also has some kind of numerical optimization technique as a solution approach. Ring (1999), Ewing et al. (1999), Rattray et al. (1999), Avitabile (2000), and Chock and Kapania (2003) were concerned with or used least squares formulation. For the solutions of their inverse problems, Dunn (1976), Chiroiu et al. (2000), Kim and Kapania (2004), Trivailo et al. (2004), and Trivailo et al. (2004) used Neural Networks and Genetic Algorithms; Brakhage (1987), Hanke (1995), Rieder (1999), Burger and Muhlhuber (2002), Chock and Kapania (2003), and Feijoo et al. (2004) used gradient based methods.

It should also be noted that in general the solutions of the optimization problems such as inverse problem 1a or 2a are still nonunique. The number of optimization solutions can be both finite and infinite. In the former case, some global optimization techniques are often needed. In the latter case, there is a need to use further priori information to add some constraints to obtain a unique solution.

1.2 Regularization Methods

In many practical inverse problems, however, non-uniqueness of the solutions or other ill-conditioned solutions is not desired. In practice, one has only data with noise due to errors in the measurements and inaccuracies of the model itself (Engl and Kugler, 2003). Then, in case of a violation of the *third* Hadamard condition (*i.e.* the solution depends continuously on the data), even a small error in data will make algorithms developed for well-posed problems fail if the instability is not desired, since data and round-off errors may be amplified by an arbitrarily large factor (Engl and Kugler, 2003).

In order to overcome these instabilities one has to use regularization methods, which in general terms replace an ill-posed problem by a family of neighboring well-posed problems (Engl and Kugler, 2003) or filter out the influence of noise (Hansen and O'Leary, 1993).

To illustrate, consider a parameter identification problem with an observable entity y of dimension m, which is in general a nonlinear function of an unknown parameter x of dimension n to be identified:

$$y \equiv y_0 + e = f(x) \tag{1.3}$$

or in the linear case $f(x) = Tx$:

$$Tx = y_0 + e \equiv y \tag{1.4}$$

Here, T is a linear operator of dimension $m \times n$, y_0 is the true data, and e is the unknown noise.

Well-known regularization methods for linear inverse problems are Tikhonov regularization and the truncated singular value decomposition (SVD) (Hansen and O'Leary, 1993; Engl and Kugler, 2003). We can illustrate both methods using the SVD of matrix T. A non-negative real number σ is a **singular value** for T (its conjugate is T^*) if there exist non-zero vectors u of dimension m and v of dimension n such that

$$Tv = \sigma u \quad \text{and} \quad T^* u = \sigma v \tag{1.5}$$

Then, the theorem of SVD states that

$$T = \sum_{i=1}^{n} \sigma_i u_i v_i^T \tag{1.6}$$

Here, the **left** and **right** singular vectors u and v are orthonormal, and the singular values σ_i are nonnegative and non-increasing numbers, *i.e.*, $\sigma_1 \geq \sigma_2 \geq \cdots \geq \sigma_n \geq 0$ (Hansen and O'Leary, 1993; Engl and Kugler, 2003). Common for all discrete ill-posed problems is that the matrix T has a cluster of singular values at zero and that the size of this cluster increases when the dimension m or n is increased (Hansen and O'Leary, 1993).

Using the SVD of T, the least squares solution to Eq. (1.4), *i.e.* the one obtained by solving the unconstrained minimization problem:

$$\min_x \|Tx - y\|_2 \tag{1.7}$$

can be written in the form

$$x_{\text{LSQ}} = \sum_{i=1}^{n} \frac{\alpha_i}{\sigma_i} v_i \tag{1.8}$$

where $\alpha_i = u_i^T y$ (Hansen and O'Leary 1993).

It is obvious from Eq. (1.8) that a direct use of the least squares solution x_{LSQ} leads to the trouble that error in the directions corresponding to small singular values is greatly magnified and overwhelms the information contained in the directions corresponding to larger singular values. To overcome this problem, it is necessary to incorporate filter factors $0 \leq f_i \leq 1$, to obtain the modified solution:

$$x_{\text{filtered}} = \sum_{i=1}^{n} f_i \frac{\alpha_i}{\sigma_i} v_i \tag{1.9}$$

The most popular regularization method is the one due to Tikhonov and Arsenin (1977), which turns to find the solution x_λ to solve the minimization problem

$$\min_x (\|Tx - y\|_2^2 + \lambda^2 \|x\|_2^2) \tag{1.10}$$

which is equivalent to choosing the filter factor:

$$f_i = \frac{\sigma_i^2}{\lambda^2 + \sigma_i^2} \tag{1.11}$$

Here, the parameter λ controls how much weight is given to minimization of $\|x\|_2$ relative to minimization of the residual norm.

Another widely used method is the truncated SVD, where one simply truncates the summation in Eq. (1.8) at an upper limit $k \leq n$, before the small singular values start to dominate (Hansen and O'Leary, 1993), or equivalently speaking, let the small singular values ("high frequencies") be filtered out by a "low-pass filter" (Engl and Kugler, 2003).

In addition to noisy-data problems, the Tikhonov regularization method is often used for the class of non-unique solution problems due to *rank-deficient* or even *underdetermined* LSQ problems (Schulze and Sachs, 2002; Eriksson and Gulliksson, 2003), where the number of the unknown variables n is larger than that of the data points m.

Noticing Eq. 1.3, the nonlinear counterpart of Eq. 1.7 is

$$\min_x \|f(x) - y\|_2 \tag{1.12}$$

the corresponding LSQ minimization formulation with the Tikhonov regularization is

$$\min_x (\|f(x) - y\|_2^2 + \lambda^2 \|x\|_2^2) \tag{1.13}$$

which is equivalent to the *constrained* minimization problem:

$$\begin{aligned} &\min \|x\|_2^2 \\ \text{s.t.} \quad &\min_x \|f(x) - y\|_2 \end{aligned} \tag{1.14}$$

For the underdetermined LSQ problem, Eq. 1.13 or 1.14 can be solved by some iterative algorithm, *e.g.* the inexact Gauss-Newton method (Schulze and Sachs, 2002) or truncated Gauss-Newton method (Eriksson and Gulliksson, 2003).

1.3 Present Work

While structural mechanics includes elasticity, plasticity, plates and shells, vibrations, aeroelasticity, finite element methods, structural stability, optimal design, fracture mechanics and composite materials, etc., in the current work, however, we address three inverse problems in a discrete setting.

The first problem (Chapter 2) is load updating for finite element models. The theory part includes the extracted load representation within an element, load updating for nonlinear FEM, and constraints on load distribution. Through a relative *model order analysis*, the benefits for solving load updating problems using the relative deformation measurement, the polynomials of lower orders, the elements of larger sizes, and the deformation of denser measured points are studied for linear responses under the applied loads of different types. It is confirmed that using the reduced number of unknown variables to obtain an *overdetermined inverse problem* helps get unique and stable extracted loads. Various applications are given.

The second one (Chapter 3) is placement optimization of a fiber optic sensor for an Integrated Smart-bed^{TM} (Spillman Jr. et al., 2004). A description of the problem is first given for the objective/sensor performance and constraints on the placement optimization of a distributed sensing optical fiber. The procedure and implementation are described. An example is given for the placement optimization of the fiber optic sensor for a smart bed using a very simple breeding genetic algorithm for the multiple solution problems. The reduced number of the unknown variables is realized by using the finite number of the control points of the NURBS representation for the distributed sensing fiber optic cable.

The third one (Chapter 4) is stiffened panel optimization. An integrated approach is adopted to use the available capabilities. The mathematical aspects include the formulation and convergence of the stiffened panel optimization. Numerical studies are made on optimal blade stiffened panel designs. The effects of the orientation, spacing, location and curvature of the stiffeners are studied. The slow and unstable convergence due to the ill-conditions is solved mainly by reducing the condition number of the Hessian for the objective, and some scaling and shifting to both the objective and constraint functions to have a balanced weights or multipliers for an extended Lagrangian formulation.

A brief literature review is given in the individual chapters of the three application fields.

Chapter 2
Load Updating for Finite Element Models

A measurement-based load updating method for finite element models subjected to static loads was studied using a four-noded curved beam element for large displacements/ rotations and a gradient-based variable metric optimizer. Finite element analysis was used to numerically calculate the geometrically linear and nonlinear responses and their sensitivities under a given load. The optimizer was used to recursively update the load so that it minimized the square of the difference between the calculated and pre-filtered/noise-free measured (displacement or strain) data. For the basic studies, the extracted load was represented within an element by a linear combination of integrated Legendre polynomials, the coefficients of which were taken as design variables of the least-squares problem. Through a relative model order analysis, the benefits for solving load updating problems using the relative deformation measurement, the polynomials of lower orders, the elements of larger sizes (because of using the high precision four-noded beam element), and the deformation of denser measured points were studied for linear responses under the applied loads of different types. It was confirmed that using the reduced number of unknown variables to obtain an *overdetermined inverse problem* helps get unique and stable extracted loads. Though this conclusion was verified mainly through illustrative examples for a cantilever beam, it was generally applicable to other load updating or inverse problems. Further examples were given for a 3D portal frame load updating, extracting highly oscillating loads, and a strain-based cantilever beam load updating. The final examples were load updating for geometrically nonlinear finite element models under under self-weight, snow and/or pressure loads.

2.1 An Overview

Finite element analysis (FEA) has long been one of the generally accepted tools for structural analysis. While differences between real testing and FEA are usually reduced using system identification, much effort has been focused on the increasing accuracy of the mathematical model of the structure from the point of view of updating the finite element model (FEM) of the structure itself under given applied loads.

However, simply updating the FEM itself is not sufficient to satisfactorily reduce the differences between the observed experimental data and numerically calculated results based on FEA if the applied loads are not exactly known. Also, operational loads, such as self-weight, snow, waves, winds, etc., either dynamic or static, are usually not simply or directly measurable. Therefore, it is an appealing alternative to use the indirect or inverse method to determine or update the approximate applied loads based on the actually measured responses of the structure under realistic working conditions by identifying load parameters of the established load model. In other words, we seek to reduce those differences by modifying not the FEM of the structural system, but the loading that the structure is subjected to such that the experimental and the finite element responses match in the least-squares sense (Rattray et al., 1999; Avitabile, 2000; Chock and Kapania, 2003).

The load updating is a special application of system identifications in the growing field of inverse problems, which arise whenever one searches for causes of observed or desired effects (Engl and Kugler, 2003). Therefore, an examination of the literature in terms of inverse problems aids us in determining the most appropriate methodology for load updating.

In most formulations, the load identification process requires the inversion of the global matrix, which tends to be very ill conditioned. That is, very small errors in measurements propagate into large errors in estimated forces, especially at frequencies close to the resonance and ant-resonance conditions (Starkey and Merrill, 1989). On the other hand, in many practical inverse problems, one aims to retrieve a model that has infinitely many DOFs from a finite amount of data, which leads to the non-uniqueness of the solutions of the *rank-deficient* or *underdetermined* problems (Schulze and Sachs, 2002; Eriksson and Gulliksson, 2003). Therefore, solving an inverse problem entails more than estimating a model: any inversion is not complete without a description of the class of models that is consistent with the data (Snieder, 1998).

The process to overcome this difficulty is called regularization, which is to replace an ill-posed problem by a family of neighboring well-posed problems (Engl and Kugler, 2003) or filter out the influence of noise (Hansen and O'Leary, 1993).

The singular-value decomposition (SVD) technique (Elliott et al., 1988; Chock and Kapania, 2003) along with the pseudo-inverse technique (Fabunmi, 1986) provides the fundamental theory and methods to overcome ill-conditioning for most linear inverse problems. The pure SVD method gives a direct solution of a direct least-squares formulation. Associated with the SVD technique are two well-known regularization methods for linear inverse problems, the Tikhonov regularization (Tikhonov and Arsenin, 1977) and the truncated singular value decomposition (SVD) (Hansen and O'Leary, 1993; Engl and Kugler, 2003). The Tikhonov regularization is to add a constraint term to the pure least-squares formulation, an approach that can be readily extended to the solution to the nonlinear inverse problems. The truncated SVD method is to truncate off all the terms of zero or close-to-zero singular values.

Smoothing or filtering either the (noisy) data or the (oscillating) solution (Louis, 1999), using over-specified or overdetermined boundary data for complete data (Bonnet and Constantinescu, 1996) and many boundary measurements (Eller, 1996), etc., are alternative and intuitive approaches to regularize the ill-posed inverse problems, and overcome oscillating, arbitrary and/or unique solution problems. A prior information (Sabatier, 1995; Kaipio et al., 1999) and a richly measured or experimental data helps one to establish unique results or solve identification problems.

A regularization effect can already be obtained by a finite-dimensional approximation of the problem, where the approximation level plays the role of the regularization parameter (Engl and Kugler, 2003). At least for severely ill-posed problems the dimension of the problem has to be low in order to keep the total extracted error small (Engl and Kugler, 2003). The number of zero singular values increases when the size of the inverse problem increases (Hansen and O'Leary, 1993). For this reason, the formulation of the inverse problems, for example, load updating or identification on the discrete setting, such as based on FEM, is advantageous. The FEM often includes a large number of degrees-of-freedom (DOF), although most of them are not necessarily needed, especially those to which no forces are applied and those for which no responses are measured. To estimate the loads, the FEM has to be reduced by model reduction techniques so that responses need only be measured at a limited number of sites (Chen and Geradin, 1996).

For almost all inverse problems, optimization is not only a formulation, but also a solution technique. Ewing et al. (1999), Rattray et al. (1999), Ring (1999), Avitabile (2000), and Chock and Kapania (2003), etc., used least-squares formulation, which is to define an error that characterizes the quality of the model with respect to the experimental data and then to minimize this error. In solving their inverse problems, Dunn (1976), Chiroiu et al. (2000), Trivailo et al. (2004), and Trivailo et al. (2004), etc., used the Neural Network and Genetic Algorithms; Hanke (1995), Rieder (1999), Burger and Muhlhuber (2002), Chock and Kapania (2003) and Feijoo et al. (2004), etc., used gradient based methods.

While a nonlinear inverse problem is usually solved by the iterative algorithms (Schulze and Sachs, 2002; Eriksson and Gulliksson, 2003; Engl and Kugler, 2003), including various optimization methods, its ill-posedness may be more severe than for linear problems as nonlinear error propagation is a difficult problem (Snieder, 1998). In the field of elasticity or structures, examples of handling nonlinear inverse problem were given by Ewing et al. (1999) for nonlinear beam cross-sectional property estimation, Chiroiu et al. (2000) for material constants extraction, Hasanov and Mamedov (1994) for identifying elasto-plastic properties of a plate, and Ring (1999) for load identification.

The identification of applied loads using measured response is not a new concept. We can easily list some early works in the literature. Pilkey and Kalinowski (1972) deal with identification of shock and vibration forces. Hillary and Ewins (1984) were concerned with the use of strain gauges in force determination and frequency response function measurements. Gregory et al. (1986) studied experimental determination of the dynamic forces acting on non-rigid bodies. Stevens (1987) presented an overview on force identification problems. Wang et al. (1987) coped with force identification from structural response. Starkey and Merrill (1989) addressed the ill-conditioned nature of indirect force-measurement techniques.

Besides, the following earlier and recent works may present a clear picture in the field of load updating or identification for structures.

Park and Park (1994) dealt with transient response of an impacted beam and indirect impact force (location and time history) identification using wave propagation theory and strain measurements.

Chen and Geradin (1996) identified the dynamic force for beamlike structures by dividing the entire structure into substructures according to the excitation locations and the measured response sites, and then represented each substructure by an equivalent element. Therefore, the resulting model only retained the DOFs associated with the excitation and the measured responses and the DOFs corresponding to the boundaries of the structures. They tried to avoid the processes of modal parameter extraction, global matrix inversion, and model reduction.

Johnson (1998c) used system informatics to derive necessary and sufficient conditions to ensure convergence of the loads determined by solving the underlying inverse problem. On the basis that a system is a superposition of signals, Johnson (1998b) developed a force and moment identification method using basis functions chosen to represent desired characteristics of time variations of loadings in a general class of linear (linearized) dynamic and vibration problems with multiple-inputs and multiple-measurements. Johnson (1998a) applied the above developed methodologies to the identification of the unknown, immeasurable static load distributions on beams, from measurements of beam static deflections. He noted the difficulties in identifying a system near the applied boundary conditions and presented a method for inverse problem solutions.

Ring (1999) identified the unknown load for a steel-concrete composite beam using the measured inclination (or slope) along the axis of the beam. A nonlinear, non-smooth constitutive relation was used to model the partial breaking of the pile at points where the bending moment exceeds a critical value. A two-step approach for the inverse problem was considered. In the first step the broken and unbroken parts of the beam were determined from the solution of a regularized least-squares problem, where a total variation type regularization term was used. In the second step a linearly constrained least-squares problem was solved. Existence, stability and convergence results were presented.

Law and Fang (2001) used the dynamic programming technique to overcome a common weakness of large fluctuations in the identified load results. The forces in the state-space formulation of the dynamic system are identified in the time domain using a recursive formula based on several distributed sensor measurements, and responses of the structure are reconstructed using the identified forces for comparison. Like all inverse problems, the computation is ill-conditioned. However, the dynamic programming technique inherently provides bounds to the ill-conditioned forces.

Chock and Kapania (2003) addressed the importance of load updating for FEM and its application in engineering. They gave a relatively extensive survey of the load updating relevant literature in the time domain as the literature for static load updating was rare. They applied the achievements in time domain to the static load updating problem, and specially dealt with the load updating for linear FEM of one-dimensional beam problems. The classical least-squares fitting method was used to minimize the error between the measured and analytical displacements. The load distribution was taken element-wise and assumed to be the linear combination of integrated Legendre polynomials with the coefficients as the known parameters to be identified. The conditioning number of the resulting system equations was examined and provided a solution method more robust through the use of singular value decomposition. This work was extended from a one-dimensional beam to a two-dimensional plate and initial results on the plate were discussed (Chock and Kapania, 2004).

Our current work presents load identification/updating for geometrically nonlinear FEM of beams and frames subjected to static loading, modeled by using a four-noded curved beam element (Kapania and Li, 2003b; Kapania and Li, 2003a). Using this element makes it possible to have a system of lower dimension as it requires fewer elements to predict the responses in higher precision and makes solving the hard nonlinear inverse problems easier for the given but limited data points if the number of the unknown load parameters is proportional to the number of elements.

The optimizer L-BFGS-B (Byrd et al., 1995; Zhu et al., 1994), a limited-memory quasi-Newton code for large-scale *bound-constrained* or unconstrained optimization, is used to solve the *pre-conditioned* least-squares problem. Though the *bound-constraints* on the design variables could play an important role in the regularization, this capability is not addressed for the current studies. A unique solution for an underdetermined system, however, is obtained numerically using this iteration-based optimizer by starting from an approximate uniform load determined by the priori information. If no priori information is known, the approximate load is assumed to vanish. Starting from a uniform load with a small design stepsize can prevent the procedure from stopping at a wildly oscillating solution.

Simplified static load models for self-weight, snow and pressure loads (Kapania and Li, 2003a) with uniform, linear or sinusoidal distribution are used for assumed operational loads at the global level. For the basic studies on the load updating, the extracted applied load is represented *elementwise* by a linear combination of the so-called integrated Legendre polynomials, though an *across-element* representation of the load is recommended for further studies to avoid the oscillations in the solution by reducing the unnecessary inverse problem model DOFs. The coefficients of integrated Legendre polynomials are the parameters to be extracted using measured displacements or strains.

We assume that the measured data are noise-free, and therefore do not directly use the general Tikhonov-like regularization though we could use it for the underdetermined system to have a unique solution. For the basic studies, however, we address the benefits for solving the load updating problems using the relative measurement method, the fewer four-noded beam elements, polynomials of lower order, and richer measured data, smoothing, and enforcing C^0 continuity to reduce the relative model order to the extent that an *overdetermined inverse problem* is obtained.

Illustrative examples of linear and nonlinear FEM are given for beams in planar loading cases and a portal frame for a 3-D loading case.

2.2 Theory

2.2.1 Load Representation within an Element

We assume that a load density function $p(\xi)$ ($\xi \in [0,1]$) over the beam element (Fig. 2.1a) can be represented by a linear combination of a set of basis functions $P_\alpha(\xi)$:

$$p(\xi) = \sum_{\alpha=1}^{N_c} c_\alpha P_\alpha(\xi); \tag{2.1}$$

here c_α are unknown load coefficients.

Though increasing the number, N_c, of basis functions over an element will allow a more accurate prediction of the element loading, it has its limits due to the accuracy of the element used. In this study, we follow the work by Chock and Kapania (2003), and use integrated Legendre polynomials as basis functions to represent the load distribution within an element. Refer to Fig. 2.1(b) and Appendix A for the shapes and definitions of the first seven integrated Legendre polynomials, respectively.

2.2.2 Load Updating for Nonlinear FEM

In general, for our geometrically nonlinear FEM in the 3-D case, we can start with the state equation of a nonlinear structural system (Kapania and Li, 2003a)

$$\mathbf{R}(\mathbf{a},\mathbf{c},\lambda) = \mathbf{q}_{\text{int}}(\mathbf{a}) - \lambda\mathbf{q}_{\text{ext0}}(\mathbf{a},\mathbf{c}) = 0. \tag{2.2}$$

where $\mathbf{R}$ is the residual vector, $\mathbf{q}_{\text{int}}$ the nodal internal force vector, $\mathbf{q}_{\text{ext0}}$ the nodal external load vector calculated at the applied load level, λ the proportional nodal loading factor; $\mathbf{a} = \mathbf{a}(\mathbf{c},\lambda)$ the nodal displacement vector, and $\mathbf{c}$ the load (force) coefficient vector, which is further determined by the unknown load design (coefficient) vector $\mathbf{x}$ with independent components. Now, we have the global entities in component forms:

$$\mathbf{R} = \begin{bmatrix} R_1 \\ R_2 \\ \vdots \\ R_{N_a} \end{bmatrix}, \quad \mathbf{q}_{\text{int}} = \begin{bmatrix} q_{\text{int}1} \\ q_{\text{int}2} \\ \vdots \\ q_{\text{int}N_a} \end{bmatrix}, \quad \mathbf{q}_{\text{ext0}} = \begin{bmatrix} q_{\text{ext01}} \\ q_{\text{ext02}} \\ \vdots \\ q_{\text{ext0}N_a} \end{bmatrix}, \quad \delta\mathbf{a} = \begin{bmatrix} \delta a_1 \\ \delta a_2 \\ \vdots \\ \delta a_{N_a} \end{bmatrix}, \quad \text{and} \quad \mathbf{x} = \begin{bmatrix} x_1 \\ x_2 \\ \vdots \\ x_{N_x} \end{bmatrix} \tag{2.3}$$

Note that $N_a \equiv N_{\text{dof}}$, the total DOFs of the finite element system; N_x is the total number of the independent load (force) coefficients or unknown load design variables.

Let $\mathbf{a}_{\text{m}}$ represent the measured displacement response and $\mathbf{a}$ the calculated displacement

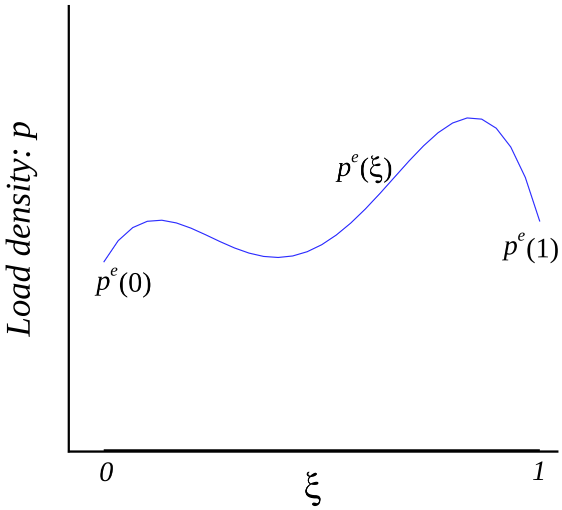

(a) Load density (p) distribution along a beam element axis (ξ).

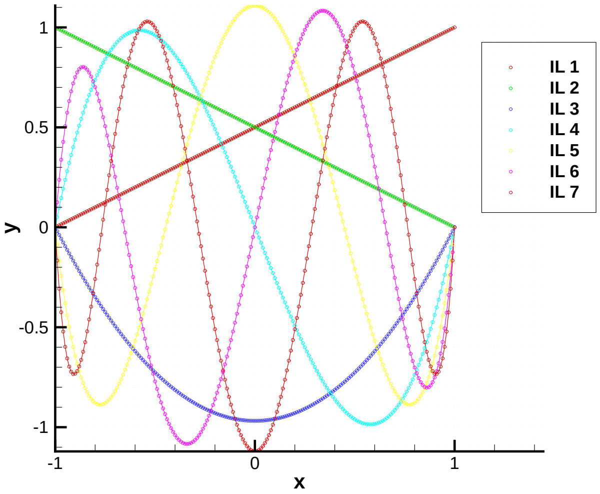

(b) First 7 Integrated Legendre Polynomials.

Figure 2.1: Load distribution within an element as a linear combination of integrated Legendre polynomials.

response. The square of the error, E_a, is given as

$$E_a = \frac{1}{2m}\mathbf{e}^{\mathrm{t}}\mathbf{e} \tag{2.4}$$

where the vector $\mathbf{e}$ is defined as

$$\mathbf{e} = \mathbf{a} - \mathbf{a}_{\mathrm{m}} \tag{2.5}$$

and m is the number of the measured data. Since the response can be measured only at a limited number of points, the dimensions of vectors $\mathbf{a}$ and $\mathbf{a}_{\mathrm{m}}$ will be different. We have to reduce the dimension of $\mathbf{a}$ to that of $\mathbf{a}_{\mathrm{m}}$ if we consider $\mathbf{a}_{\mathrm{m}}$ to be fully populated. Thus we can use a transformation matrix $\mathbf{T}$ onto $\mathbf{a}$, so that Eq. (2.4) becomes

$$E_a = \frac{1}{2m}\|\mathbf{Ta} - \mathbf{a}_{\mathrm{m}}\|_2^2 = \frac{1}{2m}\mathbf{e}^{\mathrm{t}}\mathbf{e} \tag{2.6}$$

where the vector $\mathbf{e}$ is defined as

$$\mathbf{e} = \mathbf{Ta} - \mathbf{a}_{\mathrm{m}} = \begin{bmatrix} a_{I_1} - a_{\mathrm{m}I_1} \\ a_{I_2} - a_{\mathrm{m}I_2} \\ \vdots \\ a_{I_m} - a_{\mathrm{mI}_m} \end{bmatrix} \tag{2.7}$$

where subscript indices I_1, I_2, ..., I_m give the corresponding locations at the array $\mathbf{a}$. An alternative way to measure the error is in the relative sense,

$$\bar{\mathbf{e}} = \begin{bmatrix} \frac{a_{I_1}}{a_{\mathrm{m}I_1}} - 1 \\ \frac{a_{I_2}}{a_{\mathrm{m}I_2}} - 1 \\ \vdots \\ \frac{a_{\mathrm{I}m}}{a_{\mathrm{m}I_m}} - 1 \end{bmatrix} \tag{2.8}$$

which makes smaller measured displacements and their gradients treated equally, or they would be ignored because of being truncated off due to the limited machine precision. $\bar{\mathbf{e}}$

relates to $\mathbf{e}$ by

$$\mathbf{e} = \mathbf{D}_{a_\mathrm{m}}\bar{\mathbf{e}}; \quad \text{or} \quad \bar{\mathbf{e}} = \mathbf{D}_{a_\mathrm{m}}^{-1}\mathbf{e} \tag{2.9}$$

where

$$\mathbf{D}_{a_\mathrm{m}} = \begin{bmatrix} a_{\mathrm{m}I_1} & 0 & \cdots & 0 \\ 0 & a_{\mathrm{m}I_2} & \cdots & 0 \\ \vdots & \vdots & \ddots & \vdots \\ 0 & 0 & \cdots & a_{\mathrm{m}I_m} \end{bmatrix}; \quad \text{or} \quad \mathbf{D}_{a_\mathrm{m}}^{-1} = \begin{bmatrix} \frac{1}{a_{\mathrm{m}I_1}} & 0 & \cdots & 0 \\ 0 & \frac{1}{a_{\mathrm{m}I_2}} & \cdots & 0 \\ \vdots & \vdots & \ddots & \vdots \\ 0 & 0 & \cdots & \frac{1}{a_{\mathrm{m}I_m}} \end{bmatrix} \tag{2.10}$$

Now, the least-squares problem of the load updating for the nonlinear FEM is to find the load (force) coefficient vector $\mathbf{x}$ that will

$$\text{minimize} \quad E = E_a \tag{2.11}$$

which requires that the variation of E with respect to $\mathbf{x}$ vanish, noticing Eq. (C.10) in Appendix C:

$$\delta_x E = \frac{1}{m}\mathbf{e}^\mathrm{t}\delta_x\mathbf{e} = \frac{1}{m}\mathbf{e}^\mathrm{t}\mathbf{T}\delta_x\mathbf{a} = \frac{1}{m}E_{,\mathbf{x}}\delta\mathbf{x} = \mathbf{0} \tag{2.12}$$

or equivalently, the sensitivity of the square of the displacement response error with respect to load (force) coefficient vector $\mathbf{c}$ or $\mathbf{x}$ to vanish:

$$E_{,\mathbf{x}} = \mathbf{e}^\mathrm{t}\mathbf{e}_{,\mathbf{x}} = \mathbf{0} \tag{2.13}$$

$$\mathbf{e}_{,\mathbf{x}} = \mathbf{T}\mathbf{a}_{,\mathbf{x}} \tag{2.14}$$

where $\mathbf{a}_{,\mathbf{x}} = \lambda\mathbf{K}_\mathrm{T}^{-1}\mathbf{q}_{\mathrm{ext0},\mathbf{x}}$, as given in Eq. (C.11) of Appendix C, is the sensitivity of the displacement vector $\mathbf{a}$ with respect to the load (force) coefficient vector $\mathbf{x}$, $\mathbf{K}_\mathrm{T}$ is the tangent stiffness matrix, and $\mathbf{q}_{\mathrm{ext0},\mathbf{x}}$ is the global load (force) coefficient matrix, assembled from element force coefficient matrices as given in Eqs. (B.15-B.21) of Appendix B.

For linear FEM, $\mathbf{K}_\mathrm{T}^{-1}$ is constant and therefore $\mathbf{e}_{,\mathbf{x}}$ is constant with respect to the load (force) coefficients. Equation (2.13) can be transformed to a linear equation system with symmetric coefficient matrix. For the geometrically nonlinear FEM, however, the relationships between responses and loads are no longer proportional, *i.e.*, $\mathbf{K}_{\mathrm{T}}^{-1}$ and $\mathbf{e}_{,\mathbf{x}}$ are no longer constant. Therefore, one needs to recursively solve a nonlinear system state equation within an unconstrained nonlinear programming problem or sequential unconstrained nonlinear programming problems as described in Eq. (2.11). In each load updating step, one must re-analyze the geometrically nonlinear problem for both structural responses and their sensitivities with respect to the load (force) coefficients.

The *ARCHCODE*, a FORTRAN FEA code with the four-noded curved beam element first implemented in Kapania and Li (2003a), is extended and used to predict the linear and geometrically nonlinear responses and their sensitivities with respect to the load coefficients.

2.2.3 Constraints on Load Distribution

The load updating problem usually has an infinite number of solutions due to the rank-deficient and underdetermined nature of the inverse problem. Most of the solutions may not be practical or useful for the realistic applications at hand. Therefore, it is often necessary to set certain constraints on the load distribution. For example, if we know beforehand that the load over an element should be smooth or close to a linear distribution, and/or the load across two adjacent beam elements should be continuous or almost continuous, we can enforce load smoothing within an element and/or C^0 continuity across two adjacent elements. Then, the objective function of the scaled (Banks, 2002) and mixed (Ewing et al., 1999) least-squares problem in Eq. (2.11) becomes

$$E = \lambda_a E_a + \lambda_{\mathrm{T}} E_{\mathrm{T}} + \lambda_{\mathrm{S}} E_{\mathrm{S}} + \lambda_{\mathrm{C}^0} E_{\mathrm{C}^0} \tag{2.15}$$

where

$$E_T = \frac{1}{2N_{\text{elm}}} \sum_{e=1}^{N_{\text{elm}}} \int_0^1 [p^e(\xi) - p^{e*}(\xi)]^2 \mathrm{d}\xi \tag{2.16}$$

is the general term for the Tikhonov regularization to handle both the noisy data problem and the nonunique solutions problem, and reflects the average value of the difference between the predicted load distribution $p^e(\xi)$ and the approximate one $p^{e*}(\xi)$[1] (Banks, 2002; Eriksson and Gulliksson, 2003);

$$E_{\text{S}} = \frac{1}{2N_{\text{elm}}} \sum_{e=1}^{N_{\text{elm}}} \int_0^1 [p^e(\xi) - (1-\xi)p^e(0) - \xi p^e(1)]^2 \mathrm{d}\xi \tag{2.17}$$

is the smoothing term, and reflects the average value of the extracted load error $h^e(\xi)$ compared to the linear distribution over an element, as seen in Fig. 2.2 (a), and

$$E_{C^0} = \frac{1}{2(N_{\text{elm}}-1)} \sum_{e=1}^{N_{\text{elm}}-1} [p^e(1) - p^{e+1}(0)]^2 \tag{2.18}$$

reflects the average load discontinuity between two adjacent elements, as seen in Fig. 2.2 (b). λ_a is the least-squares scale factor, and λ_{T}, λ_{S}, and λ_{C^0} are the corresponding multipliers or regularization factors for the Tikhonov regularization term E_{T}, smoothing term E_{S}, and C^0 continuity term E_{C^0}, respectively. Note that E_{S} and E_{C^0} are special cases of the general Tikhonov regularization term E_{T}.

Though both the effect of the noise in the measured data can be filtered out and a smooth unique solution can be obtained using the general Tikhonov regularization, in this study, however, the noise in the measured data is not considered as we address the benefits for solving the load updating problems using the relative measurement, fewer four-noded beam elements, polynomials of lower order, and richer measured data, solution smoothing (Louis, 1999), and enforcing C^0 continuity.

---

[1] For a classical Tikhonov regularization method, the approximate applied load term is assumed to be $p^{e*}(\xi) = 0$. If an approximate applied load is known from a priori information, the resulted extracted load may be closer to the actual applied load for a given regularization effect.

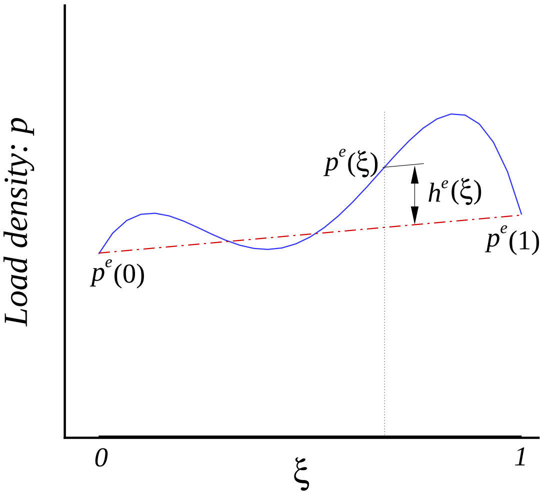

(a) Linear load density (p) distribution along a beam element axis (ξ) with unexpected large oscillation. $h(\xi)$ is the oscillation-like extracted load error at ξ.

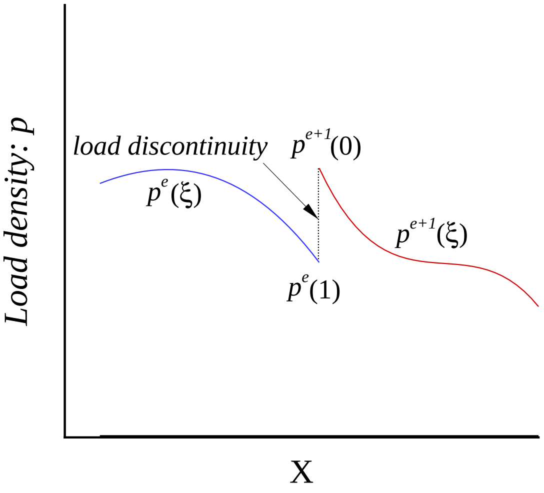

(b) Load (p) discontinuity between two adjacent beam elements. X is the global coordinate of the beam axis.

Figure 2.2: A need for constraints on the extracted load.

The optimizer *L-BFGS-B* (version 2.1) (Byrd et al., 1995; Zhu et al., 1994), a limited-memory quasi-Newton code for large-scale *bound-constrained* or unconstrained optimization, is used to solve the scaled and mixed least-squares problem Eq. 2.15. Though the *bound-constraints* on the design variables could play an important role in the regularization, this capability is not addressed for the current studies. A unique solution for the underdetermined system (when a Tikhonov regularization is not used) is obtained numerically using this iteration-based optimizer by starting from an approximate *uniform load* determined by the priori information. If no priori information is known, the approximate load is assumed to *vanish*. Starting from a uniform load with a small design stepsize can prevent the procedure from stopping at a wildly oscillating solution.

2.3 Examples

In all the numerical examples for the solutions of the LSQ problem Eq. 2.15 by the optimizer *L-BFGS-B*, the initial design variables are uniformly set to *zero*, which means the load updating procedure starts at a *zero* level load.

Unless mentioned otherwise, no Tikhonov regularization is used, *i.e.*, $\lambda_{\mathrm{T}} = 0$, $\lambda_{\mathrm{S}} = 0$, and $\lambda_{\mathrm{C}^0} = 0$.

The procedure terminates if 1) the total number of the function E and the gradient $E_{,\mathbf{x}}$ evaluations exceeds 999 or 2) the *projected gradient* $\mathrm{proj}E_{,\mathbf{x}}$ (Zhu et al., 1994; Byrd et al., 1995) is small enough: $|\mathrm{proj}E_{,\mathbf{x}}|/(\lambda_a + |E|) < \varepsilon_g$, or 3) the function value E is small enough: $|E|/\lambda_a \leq \varepsilon_f$. Then, the procedure is considered converged. The parameters are chosen as follows except when stated otherwise: $\lambda_a = 1 \times 10^{14}$, $\varepsilon_g = 1 \times 10^{-14}$, $\varepsilon_f = 1 \times 10^{-3}$, and the machine precision of the computer (Intel Pentium III, 600MHz, 128MB RAM) is $\varepsilon_{\mathrm{M}} = 2.22 \times 10^{-16}$. Referring to Eq. 2.15, we know that E is the scaled least squares. λ_a is the scalar of the squared difference between the calculated and measured deformations. ε_g

and ε_f are, respectively, the relative tolerances of proj$E_{,\mathbf{x}}$ with respect to $\lambda_a + |E|$ and E with respect to the scalar λ_a.

In addition to the above termination criteria, for nonlinear examples, the procedure stops when the step size $\|\mathbf{x}_{\text{current}} - \mathbf{x}_{\text{previous}}\|_2 \leq \varepsilon_{\text{step}} = 1 \times 10^{-3}$.

We will use the vertical (and horizontal for nonlinear case) nodal displacements under the reference load as the measured displacements and extract the load distribution with given direction. In the load updating procedure, the load distribution within an element is represented by the linear combination of up to six integrated Legendre polynomials while within the four-noded curved beam FEA procedure, the load distribution is always represented by cubic Lagrangian interpolation of the four nodal values.

In the results of all the examples, described in the following, X, Y and Z are the position coordinates of the beam or frame in a 3-D space. Displacements share the same scale as the position coordinates. When properly scaled, load density p and/or bending strain κ may share the same axis as the position coordinates. For example, $Y(p\times 10^{-1})$ or $Y(p\times 10^{-1}, \kappa\times 10^{-2})$ means that $p \times 10^{-1}$ or $\kappa \times 10^{-2}$ share the same scale as position or displacement coordinate Y: 10 units of p and/or 100 units of κ equal 1 unit of Y.

For the *model order analysis*, instead of a standard ANOVA (Analysis of Variance) (Miller et al., 1997; Bates and Watts, 1988; Walpole and Myers, 1989), the *relative model order* or *relative number of the unknown variables* is used and defined as the ratio of the *number of the independent unknown* load coefficients N_{x} to the *number of measured data* N_{m}:

$$N_{\text{m}}^{\text{x}} = \frac{N_{\text{x}}}{N_{\text{m}}} = \frac{N_{\text{elm}}(1 + \text{degree of IL polynomials})}{N_{\text{m}}} \tag{2.19}$$

When $N_{\text{m}}^{\text{x}} < 1$, the inverse problem is potentially *overdetermined with a unique solution*; but when $N_{\text{m}}^{\text{x}} > 1$, the inverse problem is *underdetermined with non-uniqueness* of the solutions. The extracted *load error variance* is defined as the average extracted load error over the beam length:

$$E_{\text{load}}^{\text{Ext}} = \frac{1}{L} \sum_{e=1}^{N_{\text{elm}}} \int_0^1 [p_{\text{ext}}^e(\xi) - p_{\text{ref}}^e(\xi)]^2 \mathrm{d}\xi \tag{2.20}$$

where p_{ext}^e and p_{ref}^e are extracted load density and reference applied load density over element e, respectively.

The basic studies are made for *a planar uniform cantilever beam subjected to distributed load*: the load density p has units of (EI/L^3). $L = 0.5$. Three kinds of load distribution of reference load will studied: uniformly, linearly, and/or sinusoidally distributed.

2.3.1 The Effect of Measurement Methods: Absolute Error and Relative Error

This example was used to compare the extracted loads obtained using two different displacement measurements. One was the absolute measurement, and the other was the relative measurement. As shown in Fig. 2.3 and Table 2.1, the load updating problem remains *overdetermined* (the relative model order $N_{\text{m}}^{\text{x}} = \frac{N_{\text{x}}}{N_{\text{m}}} = 8/9$) though the 9 measured displacement components are only taken at the two ends of the beam and 7 joint points of the 8 beam elements. It implies that there is a unique LSQ solution.

As seen in Fig. 2.3, when the absolute displacement a_i is used, the displacement error $a_i - a_{\text{m}i}$ and its gradient $a_{i,x}$ with respect to the load x close to the fixed end are smaller. This would make the load stop at a low level x. When the relative displacement $a_i/a_{\text{m}i}$ is used, however, its gradient $a_{i,x}/a_{\text{m}i}$ with respect to the load x is larger if $a_{\text{m}i}$ is smaller. This would make the load stop at a higher level $x/a_{\text{m}i}$. It is concluded that calculating the error between the calculated and measured displacements in the relative sense (Eq. 2.8) is better than in the absolute sense (Eq. 2.7). By increasing the accuracy from $\varepsilon_g = 1 \times 10^{-9}$ to $\varepsilon_g = 1 \times 10^{-14}$ (which is closer to the machine precision $\varepsilon_{\text{M}} = 2.22 \times 10^{-16}$), the extracted load agrees perfectly with the reference applied load.

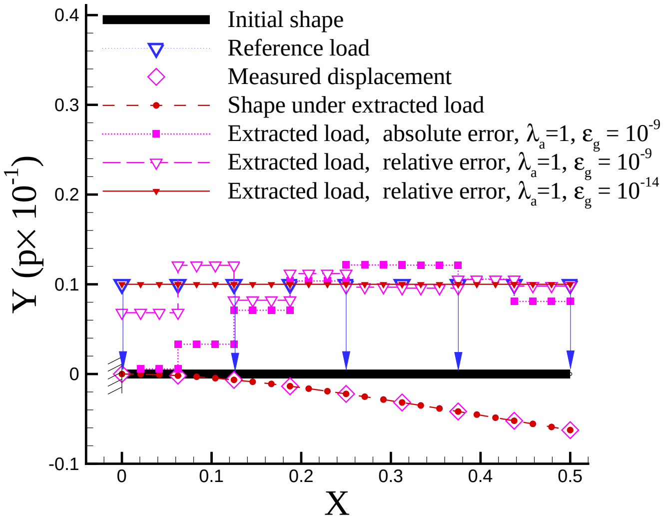

Figure 2.3: A comparison of the extracted loads for a cantilever beam with absolute or relative error between the calculated and measured displacements at 9 points. The applied reference load was uniformly distributed and the extracted load within an element was also assumed to be uniformly distributed. Eight four-noded curved beam elements were used to model the beam. The extracted load with relative error of displacements was closer to the applied reference load than that with absolute error of displacements.

Table 2.1: $E_{\text{load}}^{\text{Ext}}$ vs. absolute and relative displacement measurements.

Measurement method	Absolute displacement	Relative displacement $\varepsilon_g = 1 \times 10^{-9}$	Relative displacement $\varepsilon_g = 1 \times 10^{-14}$
$N_{\text{m}}^{\text{x}} = \frac{N_{\text{x}}}{N_{\text{m}}}$	8/9	8/9	8/9
$E_{\text{load}}^{\text{Ext}}$	6.229×10^{-2}	2.219×10^{-2}	1.225×10^{-10}

In all the examples that fellow, the relative measurement is used.

2.3.2 The Effect of the Order of Integrated Legendre Polynomials

Since the extracted load within an element is represented by a linear combination of integrated Legendre polynomials, a numerical investigation was made on a single elemented cantilever beam of 4 nodes and 4 measured displacement components to see the effect of different orders of the polynomials on the extracted load for a uniformly distributed reference load, as shown in Fig. 2.4 and Table 2.2. The results show that when the order of polynomials is small enough as to make the problem determined or overdetermined, *i.e.*, $N_{\text{m}}^{\text{x}} = \frac{N_{\text{x}}}{N_{\text{m}}} \leq 1$, the applied load can be better extracted. An increase in the order of polynomials does not always result in a better extracted load. Instead, a higher order of polynomials introduces more unknowns, tends to make the problem underdetermined, and results in oscillating extracted loads.

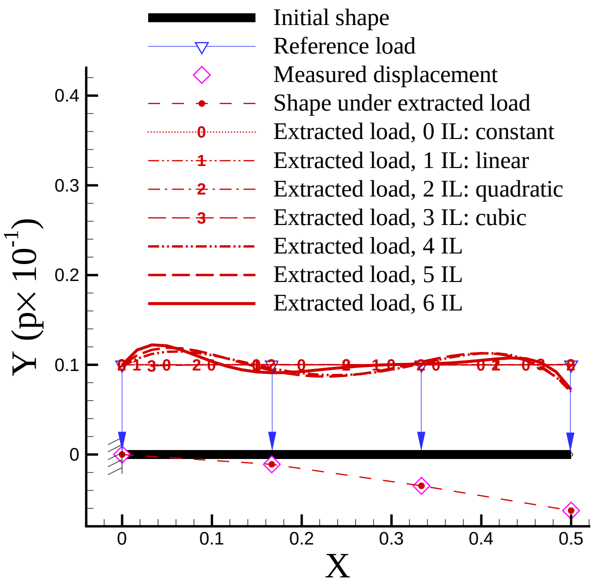

Figure 2.4: Extracted load for a cantilever beam subjected to a uniform reference load as a function of number of integrated Legendre polynomials. Polynomials up to degree 3 extracted the load perfectly. Higher-order polynomials gave a relatively large oscillating error around the reference load.

Table 2.2: $E_{\text{load}}^{\text{Ext}}$ vs. the degree of Integrated Legendre polynomial within one element.

Degree of IL	0	1	2	3	4	5	6
$N_{\text{m}}^{\text{x}} = \frac{N_{\text{x}}}{N_{\text{m}}}$	1/4	2/4	3/4	4/4	5/4	6/4	7/4
$E_{\text{load}}^{\text{Ext}}$ (Uniform load)	0.000	0.000	0.000	8.864 $\times 10^{-4}$	1.436 $\times 10^{-2}$	1.565 $\times 10^{-2}$	1.294 $\times 10^{-2}$

2.3.3 The Effect of Element Size

Refer to Fig. 2.5 and Table 2.3. The extracted loads for applied reference loads with uniform, linear and sinusoidal distributions were investigated as functions of the number of elements used. The number of elements used was 1, 2, 4 and 8, respectively. The extracted load within an element was assumed constant. In all the cases shown in the figure and table, the measured data were taken only at 4 points except for Fig. 2.5(d). It appears that the problem is determined or overdetermined for all cases except for the case of 8 elements and better extracted loads are expected. However, as the constant extracted loads of fewer elements cannot better represent the non-uniform load distributions, the extracted load errors tend to be dominant.

Table 2.3: $E_{\text{load}}^{\text{Ext}}$ vs. the number of elements (N_{elm}).

N_{elm}	1	2	4	8
$N_{\text{m}}^{\text{x}} = \frac{N_{\text{x}}}{N_{\text{m}}}$	1/4	2/4	4/4	8/4
$E_{\text{load}}^{\text{Ext}}$ (Uniform load)	0.000	0.000	0.000	0.000
$E_{\text{load}}^{\text{Ext}}$ (Linear load)	2.575×10^{-2}	1.187×10^{-2}	1.300×10^{-2}	1.357×10^{-2}
$E_{\text{load}}^{\text{Ext}}$ (Sine load)	2.190×10^{-2}	3.501×10^{-2}	1.771×10^{-2}	1.532×10^{-2}

Therefore, an increase in the number of finite elements does not help in extracting a load

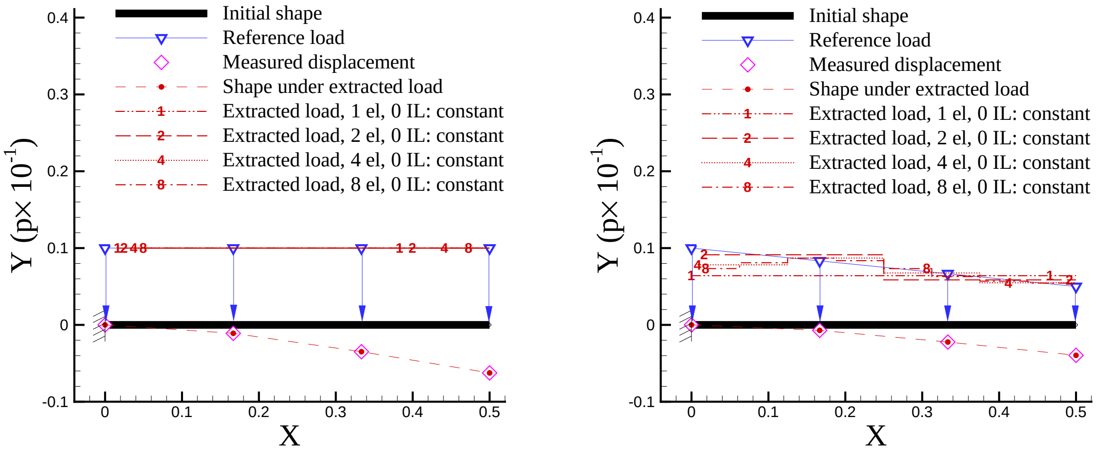

(a) Constant reference load.

(b) Linear reference load.

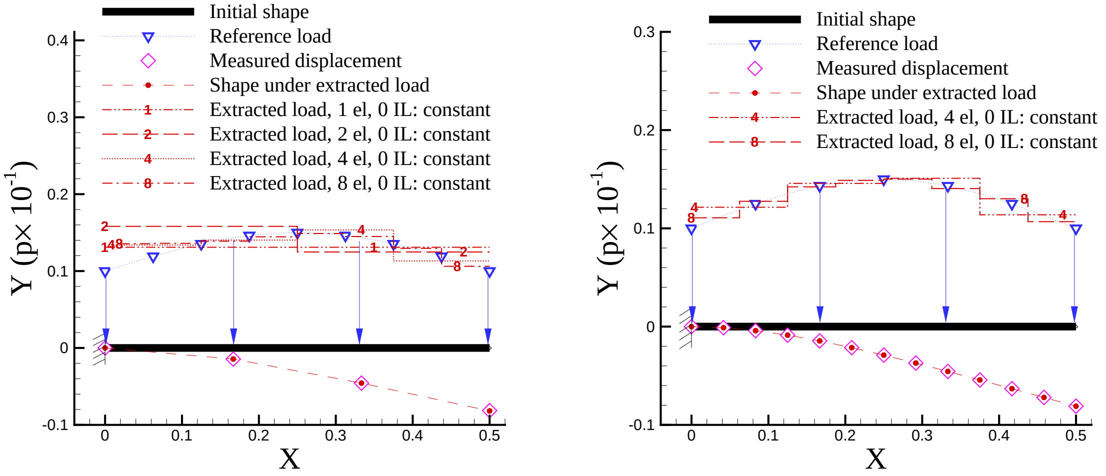

(c) Sinusoidal reference load.

(d) Sinusoidal reference load (13 measured points for displacements).

Figure 2.5: Extracted load for a cantilever beam as a function of number of elements. The load within each element was assumed to be uniformly distributed.

closer to the reference load though it has a potential to better represent the non-uniform distribution of an applied load. Instead, the minimum number of elements that meets the requirement of the accuracy of FEA may get the extracted load closest to the reference load for a given number and distribution of measured points over the beam. This makes using a high precision four-noded beam element advantageous because one can use fewer elements to obtain a regularization effect by turning the problem to be an overdetermined one.

Increasing the number of elements seemingly tends to improve the quality of the extracted load far off the supporting boundaries. In fact, the better extracted load was obtained more due to a better representation of the load distribution. The extracted load got worse near the boundaries as the number of elements increased due to the limited number of the measured points. This conclusion is seemingly contrary to the previous observation (Chock and Kapania, 2003) that aimed at reducing the boundary effect (Johnson, 1998a; Chock and Kapania, 2003) by increasing the number of elements near the boundaries. In fact, the reduced boundary effect was more due to an increase in the *noise-free* measured data (and reduced model order) near the boundaries. Compare Fig. 2.5(c) and Fig. 2.5(d).

2.3.4 The Effect of Density of Measured Points

Generally speaking, the more information about the structural model, load, and response is known, the better the extracted load tends to be. Therefore, we expect that an increase of the local and global density of *noise-free* measured points does help in bringing the extracted load closer to the reference load (under which the measured data are taken).

The extracted loads for the uniformly, linearly and sinusoidally distributed reference loads, respectively, with constant extracted load within an element are presented as functions of the number of measured points in Fig. 2.6 and Table 2.4 (for linear reference load), in which eight elements were used and the number of measured points is 4, 7, 13, and 25, respectively. Obviously, more measured points tend to improve the quality of the extracted

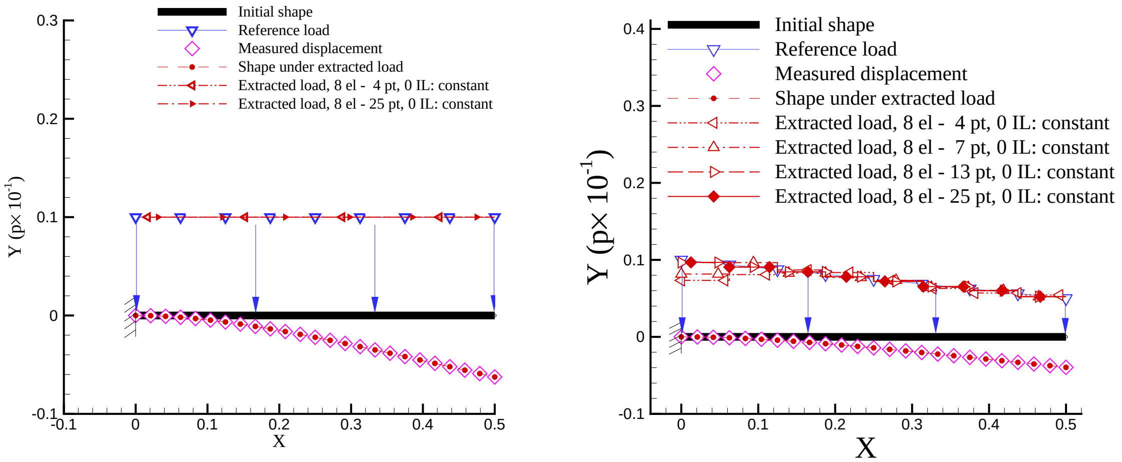

(a) Constant reference load

(b) Linear reference load: Full beam.

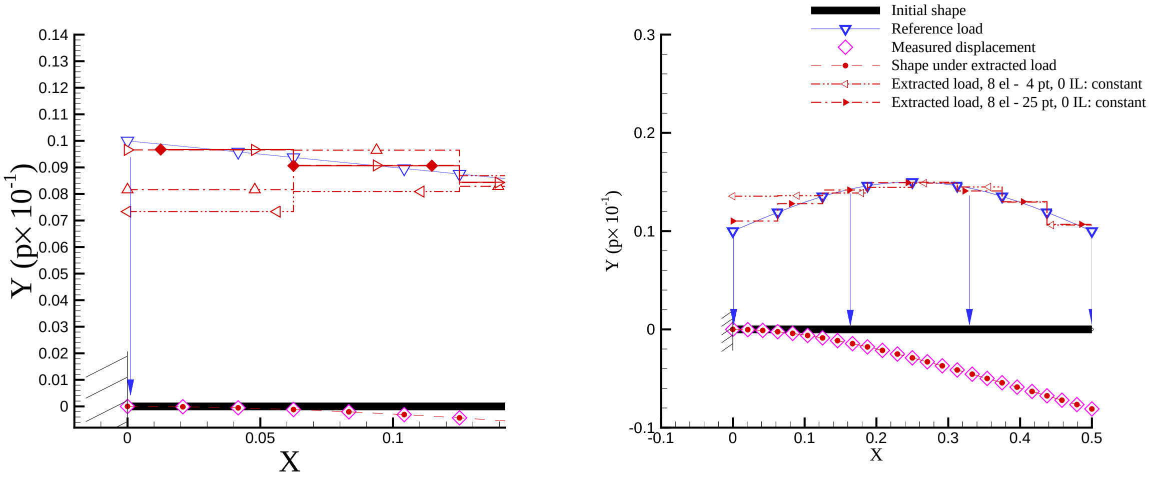

(c) Linear reference load: Close-up at fixed end.

(d) Sinusoidal reference load

Figure 2.6: Extracted load for a cantilever beam as a function of number of measured points. The applied reference load was uniformly, linearly or Sinusoidally distributed, but the load within each of the elements was assumed to be uniformly distributed.

load, especially near the boundaries, without increasing the number of elements, which tends to reduce the problem to be overdetermined or more overdetermined ($N_{\mathrm{m}}^{\mathrm{x}} < 1$).

Table 2.4: $E_{\mathrm{load}}^{\mathrm{Ext}}$ vs. the number of measured points (N_{m}).

N_{m}	4	7	13	25
$N_{\mathrm{m}}^{\mathrm{x}} = \frac{N_{\mathrm{x}}}{N_{\mathrm{m}}}$	8/4	8/7	8/13	8/25
$E_{\mathrm{load}}^{\mathrm{Ext}}$ (Linear load)	1.357 $\times 10^{-2}$	8.766 $\times 10^{-3}$	2.706 $\times 10^{-3}$	2.705 $\times 10^{-3}$

2.3.5 The Effect of Enforcing Smoothing and C^0 Continuity

When a polynomial of higher order is assumed within an element for extracting a load, the resulting extracted load will have unexpected oscillation within an element and discontinuity between two adjacent elements. Therefore, it may be useful to enforce C^0 continuity and load smoothing. The illustrative example was a planar uniform cantilever beam subjected to linearly distributed load. Refer to Fig. 2.7. Eight four-noded beam elements ($N_{\mathrm{elm}} = 8$) were used. The $N_{\mathrm{m}} = 25$ measured displacement components were taken from all of the available nodes ($N_{\mathrm{node}} = 3N_{\mathrm{elm}} + 1 = 25$). The first 4 integrated Legendre polynomials were used for the extracted load representation within an element. Therefore, the problem is underdetermined at the begining as the relative model order $N_{\mathrm{m}}^{\mathrm{x}} = \frac{N_{\mathrm{x}}}{N_{\mathrm{m}}} = 8 \times (1+3)/25 = 32/25 > 1$. When only the C^0 continuity is enforced, it equivalently adds $N_{\mathrm{elm}} - 1 = 7$ constraints to the model. This only brings the model to appear barely determined $N_{\mathrm{m}}^{\mathrm{x}} = (32-7)/25 = 1$. Although the load discontinuity disappears, the extracted load oscillation still exists. It implies that the problem remains ill-posed. When both the C^0 continuity and

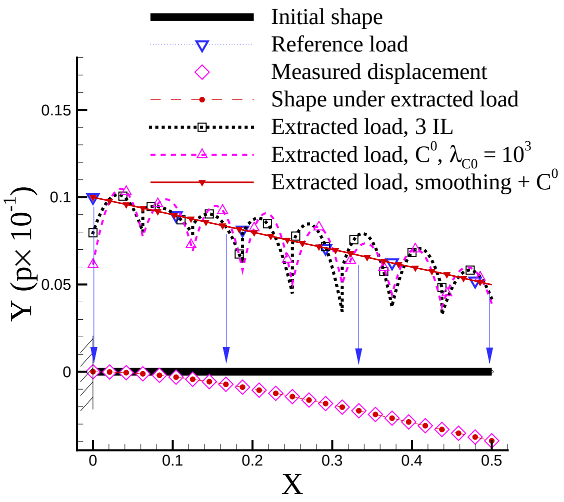

Figure 2.7: Constraining the extracted load through the enforcement of load smoothing within an element and C^0 between two adjacent elements: $\lambda_S, \lambda_{C^0} = 1 \times 10^3$ continuity. The applied reference load was linearly distributed but a linear combination of first 4 integrated Legendre polynomials (highest degree is 3) was used to represent the load distribution over an element for load extraction. Eight elements were used to model the beam.

load smoothing are enforced, it equivalently adds $N_{\text{elm}} - 1 + N_{\text{elm}} = 15$ constraints to the model. This brings the model to appear overdetermined $N_{\text{m}}^{\text{x}} = (32 - 15)/25 = 17/25 < 1$. Both the load discontinuity and oscillation disappear!

2.3.6 An Application to a Portal Frame

After the basic studies on the load updating for finite element models were for a cantilever beam using the four-noded beam element, the proposed approach and recommendations were applied to extract loads acting on a portal frame with a height of unit length and a span of 2 units. The load density p has units of EI/h^3 where h is the height of the frame. Note that both the applied load and deformation are out of plane. One element was used for each of the two columns (under linearly distributed load with 1 unit of load at one end and 0.5 at the other end) and two elements were used for the top beam (under

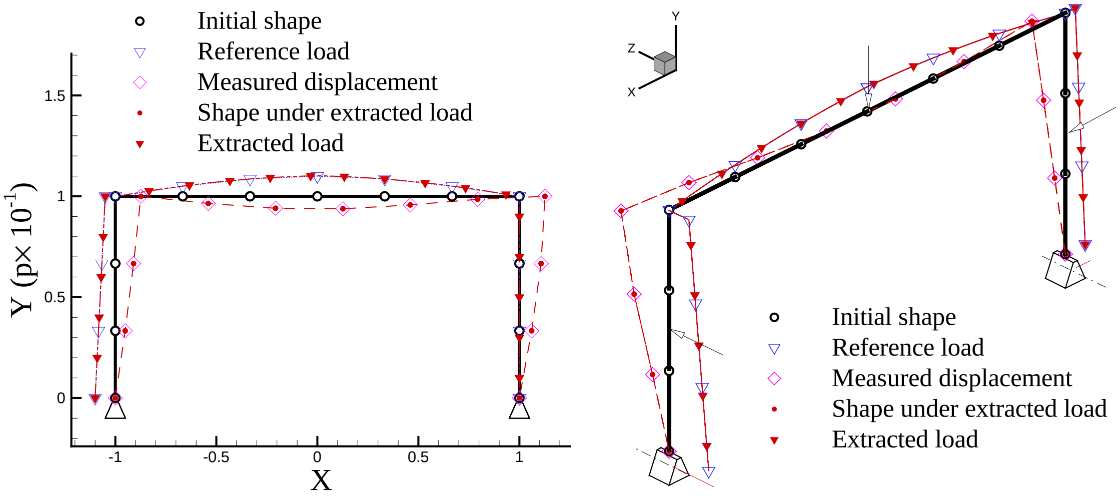

(a) 2D view.

(b) 3D view.

Figure 2.8: Extracting in-plane and out-plane loads for a portal frame.

sinusoidally distributed load with zero mean value and amplitude of 0.5 unit). Quadratically distributed load was assumed to be acting on each element. Therefore, the relative model order $N_{\mathrm{m}}^{\mathrm{x}} = \frac{N_{\mathrm{x}}}{N_{\mathrm{m}}} = 4 \times (1+2)/13 = 12/13 < 1$, which means it is an overdetermined problem. The results in Fig. 2.8 show that the extracted load agreed well with the applied reference load.

2.3.7 An Application to Highly Oscillating Load Updating

It is interesting to see the performance of the load updating for FEM under *non-noisy* but highly varying load. The example being investigated was a planar uniform cantilever or simply supported beam subjected to sinusoidally waved distributed load; the load density p has units of EI/L^3. $L = 0.5$.

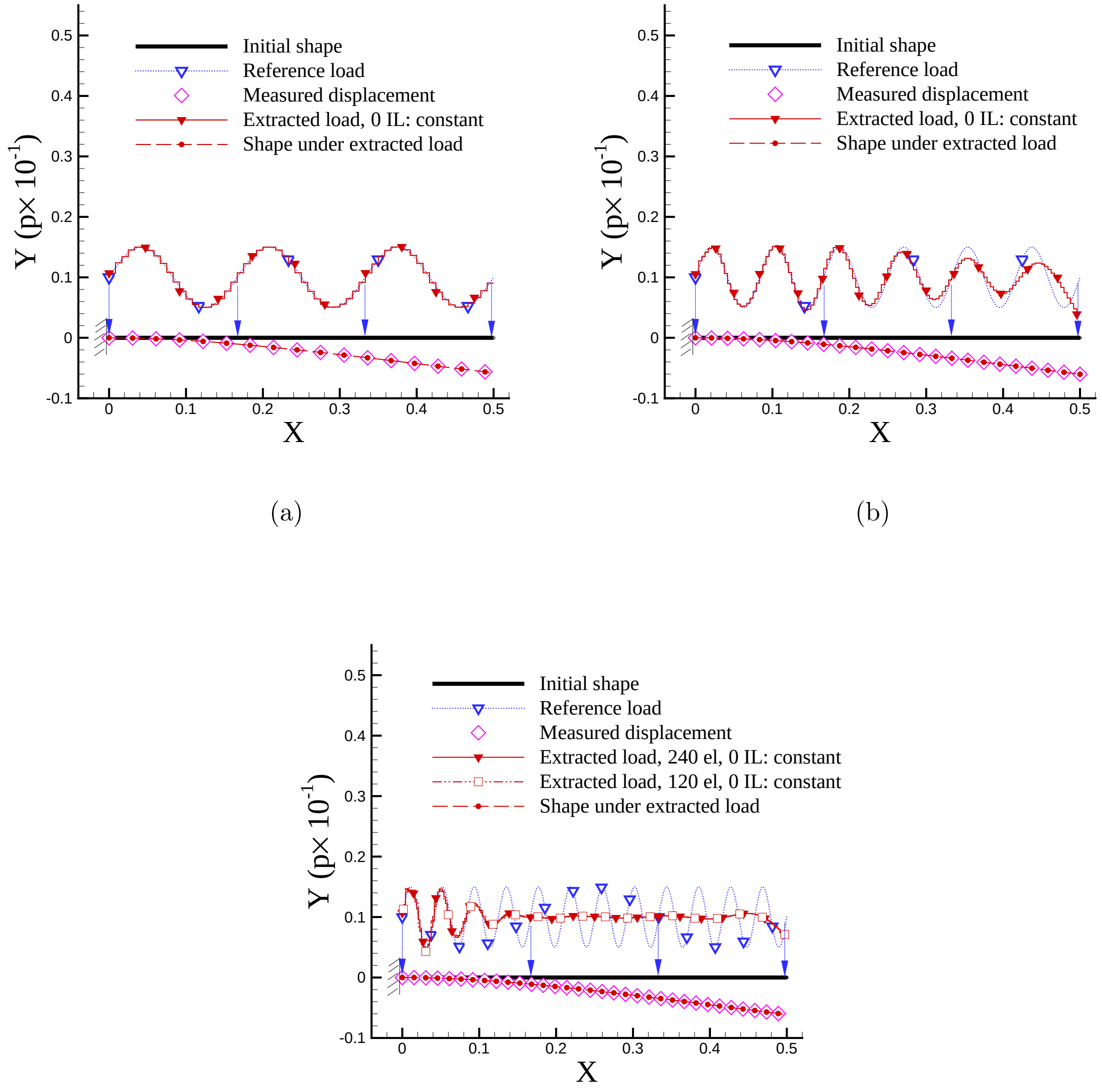

(a)

(b)

(c)

Figure 2.9: Extracting highly oscillating load for a cantilever beam. The applied reference load (RL) was sinusoidally distributed with unit mean value. The extracted load (EL) was assumed uniformly distributed within an element. (a) The RL had 3 sine waves. 60 elements were used. The EL agreed well with the RL. (b) The RL had 6 sine waves. 120 elements were used. The EL agreed well with the RL at first 3 sine waves near the fixed end but tended to be close to the unit mean value of the RL at the other 3 sine waves near the free end. (c) The applied load had 12 sine waves and unit mean value. 240 (120) elements were used. The EL agreed well with the RL at only 1.5 sine waves near the fixed end but tended to be close to the unit mean value of the RL near the free end. Results using both 120 and 240 elements are almost identical.

For all the cases shown in Fig. 2.9, a constant extracted load was assumed for each four-noded beam element and the measured displacement components were taken at all available nodes. As a large number of elements was used, the relative model order was $N_{\mathrm{m}}^{\mathrm{x}} \approx 1/3 < 1$. It means the problem is very overdetermined.

The results for the cantilever beam show that the load updating using the four-noded beam element is able to extract the applied load for moderately waved load, but only good to extract the mean value of the highly waved load. In other words, the load updating tends to extract the average part of the applied load but filters out the highly oscillating part of the load. This numerical "damping" effect may be contributed to the truncated errors due to the limited machine precision. Figure 2.9 shows the results for the cantilever beam.

2.3.8 Measured Strains Based Load Updating

A planar uniform cantilever beam subjected to distributed load: the load density p has units of EI/L^3. $L = 0.5$. The measured data were the bending strains taken at 3 Gaussian points of each of the 8 four-noded beam elements. Therefore, the relative model order was $N_{\mathrm{m}}^{\mathrm{x}} = 8/(8 \times 3) = 1/3 < 1$, implying an overdetermined problem. The sensitivities of the strains with respect to the assumed load coefficients were calculated according to the method explained in Appendix D. While the uniformly distributed load was assumed within a single element, the applied reference load was uniformly, linearly and sinusoidally distributed, respectively, as shown in Fig. 2.10. The results show that the extracted load agreed well with the applied load.

2.3.9 An Application to Geometrically Nonlinear Beam

Thus far, we have extracted loads acting on beams and frames assuming that the beam or the frame behaves linearly. The approach was also used to extract loads under which the

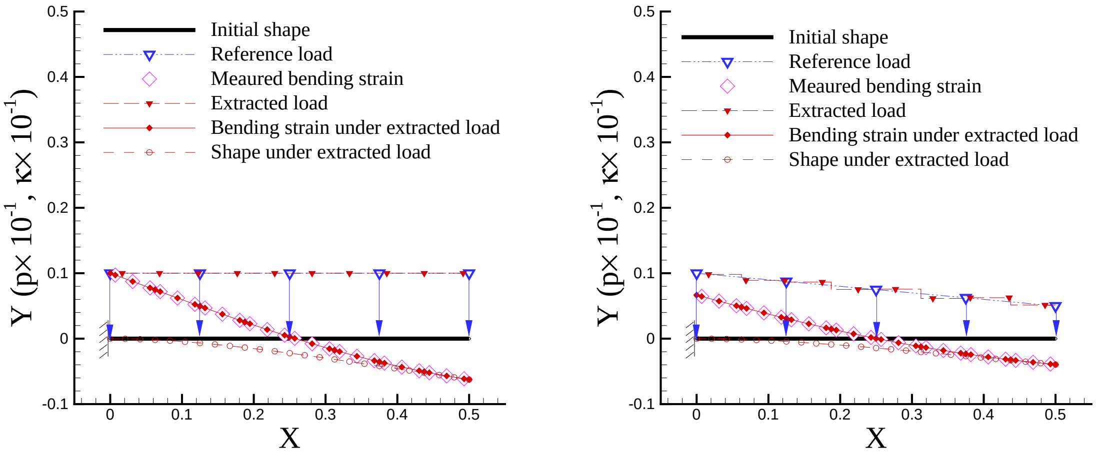

(a) Uniformly distributed.

(b) Linearly distributed.

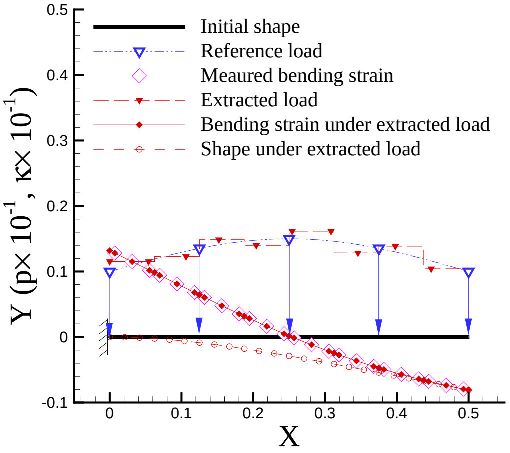

(c) Sinusoidally distributed.

Figure 2.10: Extracting loads of different distributions for a cantilever beam with measured bending strains at 3 Gaussian points in each of the 8 elements. Load within each element was assumed to be uniform.

response can be nonlinear. The finite element used in this study is capable of simulating geometrically nonlinear behavior. The capability to extract loads that lead to a nonlinear behavior was investigated for a cantilever beam subjected to self-weight, snow load, and pressure load. For a nonlinear behavior, the axial displacement of the beam cannot be ignored, while it is ignored for a linear case. It should, however, be pointed out that it would be rather difficult to measure the axial displacement. Therefore, we investigated the role of measuring the axial displacement along with the transverse displacement.

The example being investigated was a planar uniform cantilever beam subjected to uniformly distributed load: the load density $p = 5$ has units of EI/L^3. $L = 0.5$.

In all cases, a uniform extracted load was assumed for each of eight four-noded beam elements. The measured displacements were taken from all the 25 nodes. The problem was overdetermined for all cases as the relative model order $N_{\mathrm{m}}^{\mathrm{x}} \leq 8/(8 \times 3 + 1) \approx 1/3 < 1$. The full Newton-Raphson approach (Kapania and Li, 2003b) with 10 equal load steps was used to solve the geometrically nonlinear problem.

Self weight load

For self-weight type load, the extracted load agrees well with the reference applied load when transverse displacement alone is taken as measured data, which is as good as when both transverse and axial displacement are used (see Fig. 2.11).

Snow load

For snow type load (type II-n as compared with type II-c) (Kapania and Li, 2003a), the extracted load agrees well also with the reference applied load when transverse displacement alone is taken as the measured data, which is as good as when both transverse and axial displacement are used (Fig. 2.12).

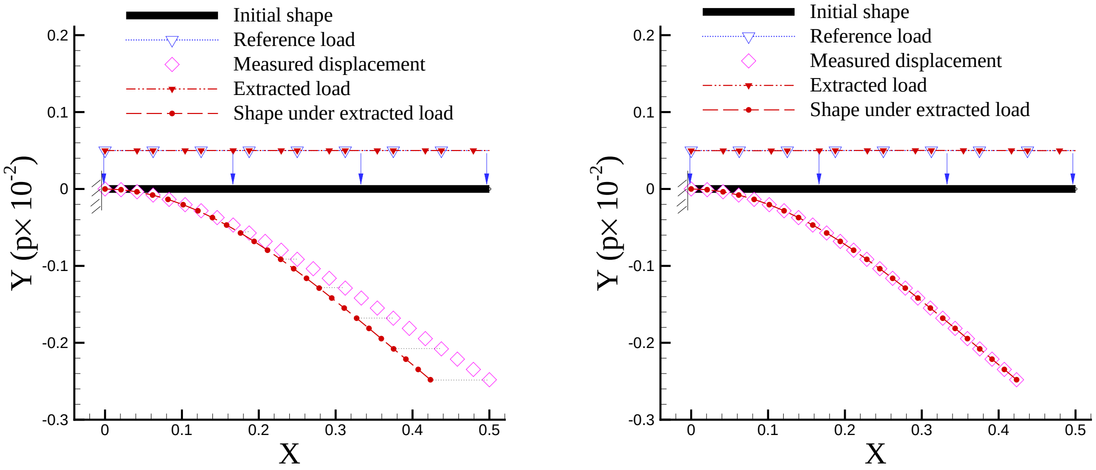

(a) The applied load was extracted using transverse displacements only (the unknown axial displacements are set to zero in the figure) of all the 25 nodes. The extraction required 45.59 seconds of CPU time, 28 nonlinear finite element analyses and 21 load updating iterations, stopping when the design step size was 0.00019.

(b) The applied load was extracted using both transverse and axial displacement components of all the 25 nodes. The extraction required 45.58 seconds of CPU time, 15 nonlinear FEA and 11 load updating iterations, stopping when the design step size was 0.00063.

Figure 2.11: Extracting uniform self-weight type load for a cantilever beam. Eight finite elements were used to model the beam.

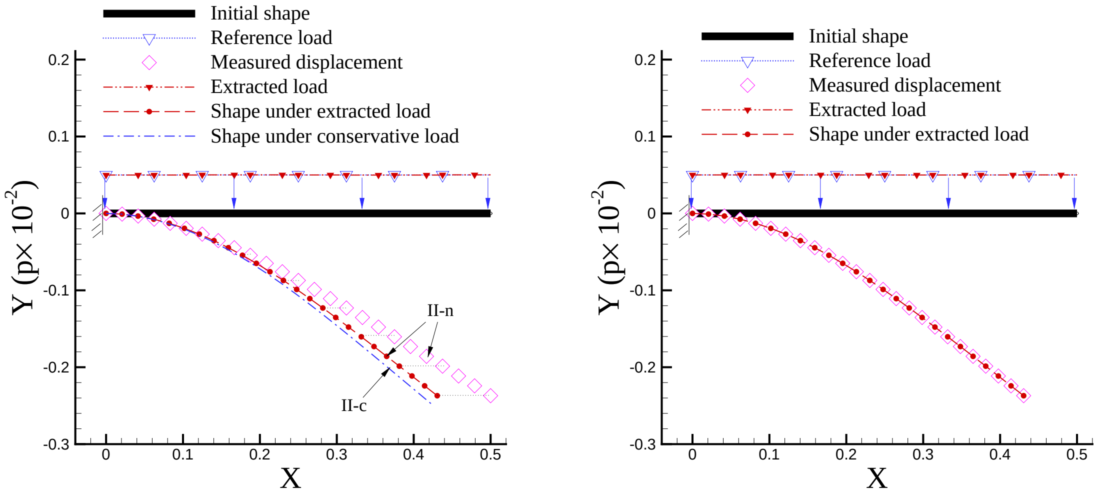

(a) The applied load was extracted using transverse displacements only (the unknown axial displacements are set to zero in the figure) of all the 25 nodes. The extraction required 57.30 seconds of CPU time, 23 nonlinear FEA and 17 load updating iterations, stopping when the design step size was 0.00045.

(b) The applied load was extracted using both transverse and axial displacement components of all the 25 nodes. The extraction required 44.26 seconds of CPU time, 16 nonlinear FEA and 12 load updating iterations, stopping when the design step size was 0.0006.

Figure 2.12: Extracting uniform snow loads of type II-n (non-conservative consideration) as compared with type II-c (conservative consideration) for a cantilever beam. Eight finite elements were used to model the beam.

Pressure load

For pressure type load, we found that when only transverse displacement was taken as the measured data, the load updating procedure failed to converge to a satisfactory solution for the given load level (Fig. 2.13a). However, simply adding an axial measured displacement at the free end (Fig. 2.13b), the extraction not only converged to the expected solution, but the extracted results are also as good as when both the transverse and axial displacements at all the 25 points are taken as the measured data (Fig. 2.13c).

2.4 Conclusions

The load updating for geometrically linear and nonlinear beams/frames with the given *noise-free* measured deformation has been studied by the use of a four-noded curved beam element and the optimizer L-BFGS-B.

For the basic studies, the extracted load was represented within an element by a linear combination of integrated Legendre polynomials, the coefficients of which were taken as design variables of the least-squares problem.

Through a relative model order analysis, the benefits for solving load updating problems using the relative deformation measurement, the polynomials of lower orders, the elements of larger sizes (because of using the high precision four-noded beam element), and the deformation of denser measured points were studied for linear responses under the applied loads of different types.

It was confirmed that using the reduced number of unknown variables to obtain an overdetermined inverse problem helps get unique and stable extracted loads. Though this conclusion was verified mainly through illustrative examples for a cantilever beam, it was generally applicable to other load updating or inverse problems.

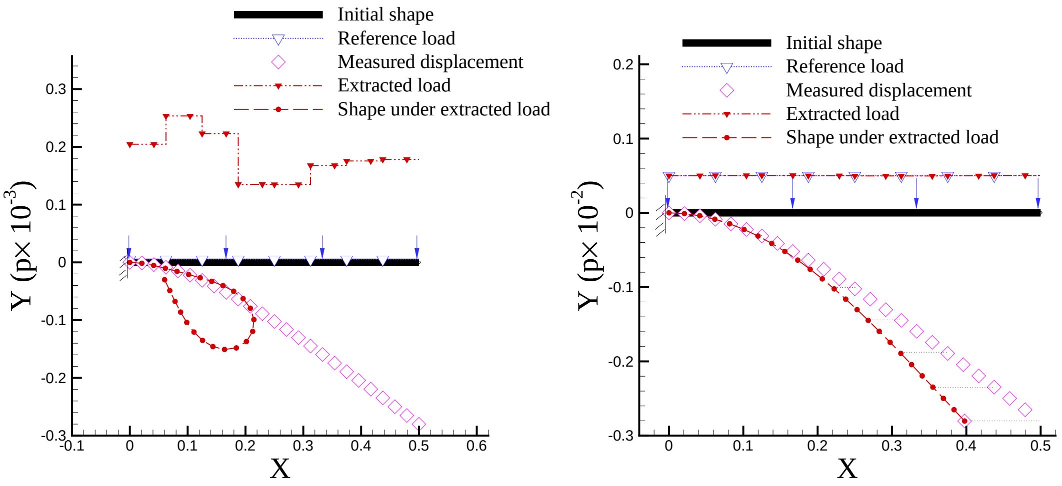

(a) The RL failed to be extracted using TD only. It stopped when DS was 1.114×10^{-12} but the objective did not converge to zero though each nonlinear FEA converged!

(b) The RL was extracted using TD and AD measured only at the free-end. It took 28.98 seconds of CPU time, 18 FEA and 14 LUI, stopping when DS was 0.00079.

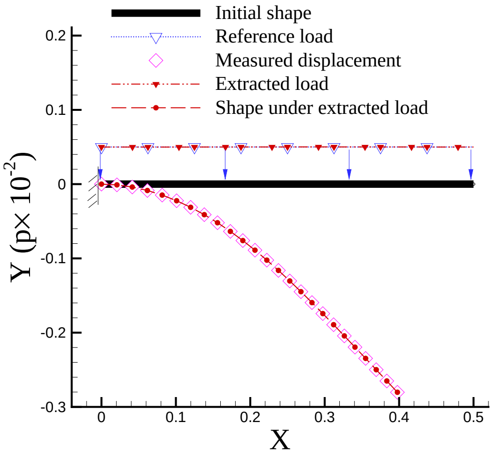

(c) The RL was extracted using all TD and AD. It took 32.96 seconds of CPU time, 20 FEA and 12 LUI, stopping when DS was 0.00065

Figure 2.13: Extracting uniform pressure load for a cantilever beam with different choices of displacement measurements. Eight finite elements were used. The unknown axial displacements are set to zero in the figure. The TD were measured at all the 25 nodes. TD: transverse displacements; RL: reference load; AD: axial displacements. DS: design stepsize; LUI: load updating iterations.

Application examples were given for a 3D portal frame load updating, extracting highly oscillating loads, and a strain-based cantilever beam load updating, and load updating for geometrically nonlinear finite element models under under self-weight, snow and/or pressure loads.

The extraction of highly varying applied load shows that the load updating for FEM using the four-noded beam element is able to extract moderate waved load, but only extract the average part of the load and filter off the highly oscillating part. This damping effect is due to the truncated error of numerical implementation.

For a linear FEM, using only transverse components of the displacements are enough to extract the applied load of a cantilever beam or simply-supported beam. However, for a geometrically nonlinear FEM, both transverse and axial components of the displacement at the measured points have to be used for a higher load level, especially for pressure load.

Present conclusions may be applied to the measurement based load updating for general finite element models when the measured data are pre-smoothed or the noise in the data is pre-filtered off.

Chapter 3
Placement Optimization of Fiber Optic Sensors

We address the methodology and implementation for the placement optimization of a distributed sensing fiber optic sensor using a simple breeding Genetic Algorithm (GA). The sensor consists of an infinite number of infinitesimal sensors continuously connected together, and its total output is proportional to the absolute value of the first time derivative of the integrated spatial perturbation along the fiber. For the placement optimization, the sensor performance is simplified as the full length integration of the absolute curvature change of the fiber optic cable due to the perturbation on the deformed shape of the fiber optic cable. The sensing optical fiber curve is represented by Non-Uniform Rational B-Splines (NURBS). The coordinates of the control points of the NURBS curve are the design variables, coded as genes of a chromosome string in the GA. The constraints include the maximum length and maximum initial curvature of the fiber optic cable. As an application example for a clinical smart bed, the deformation of the fiber optic cable is calculated from the deformation of the mattress surface by the assumption that the fiber optic cable remains adhered to the mattress surface, while the deformation of the foam-cored mattress is calculated using the finite element code MSC.NASTRAN under given body pressure distributions. An interactive Java tool was developed for the implementation of the placement optimization of the fiber optic sensor. Illustrative examples are presented to demonstrate the validity of the approach and usefulness of the tool. Though the specific example is for clinical use, the fiber optic sensor and associated placement methodology can also be used in pilot/passenger seats and structures for flight vehicles.

3.1 An Overview

Sensor placement or sensor location design is an important issue that engineers must address in solving problems like identification, analysis, control, and health monitoring of various structures. Such structures include aerospace crafts, bridges, and offshore platforms, as well as human bodies in clinical areas. There are often many limitations in sensor placement. For example, the number of available sensors is limited and their positions essentially fixed in service (Abdullah et al., 2001; Guo et al., 2004). In such situations, sensor placement becomes a critical issue which governs the success and failure of the target purpose.

Though there are many types of sensors/actuators for structural health management technology for non-aerospace and aerospace vehicles including fiber optic sensors, active and passive acoustic sensors, electromagnetic sensors, wireless sensing systems, MEMS, and nanosensors (Prosser, 2003), the algorithms for optimal placement of actuators and sensors appear to be very similar regardless of the application (Padula and Kincaid, 1999). All can be posed as selecting a subset of locations from a large set of candidate locations (Padula and Kincaid, 1999). Therefore, it is useful to review some literature on sensor placement in other fields for the sensor placement of the specific kind.

Methods have been developed to optimally place sensors to address the identification and control of dynamic structures by Udwadia and Garba (1985) and Lim (1991), etc. Kammer (1991b) proposed an effective independence algorithm based on the contribution of each sensor location to the linear independence of the identified modes. The initial candidate set of sensor locations was quickly reduced to the number of available sensors. Kammer (1991a) dealt with the effect of sensor error on sensor placement. He also reported many earlier work on the optimal placement of sensors for identification and control from a control dynamics standpoint, and some smaller amount of work considering optimal sensor placement for identification from a structural dynamics point of view. Kammer and Brillhart (1994) studied optimal sensor placement for modal identification using system-realization methods. The sensor placement method maximized spatial independence and signal strength of targeted mode shapes by maximizing the determinant of an associated Fisher information matrix. Hemez and Farhat (1994) extended the effective independence method in an algorithm where sensor placement was achieved in terms of the strain energy contribution of the structure.

Miller (1998) computed a Gaussian quadrature formula using the functional gain as a weight function, and thought that the nodes of the quadrature formula gave the optimal locations for sensors. Hiramoto et al. (2000) used the explicit solution of the algebraic Riccati equation to determine the optimal sensor/actuator placement for active vibration control. Wouwer et al. (2000) presented an optimality criterion for the selection of optimal sensor locations in distributed parameter systems; the criterion was based on a measure of independence of the sensor responses. For fault detection, Worden and Burrows (2001) used a number of different methods to determine an optimal sensor distribution based on the curvature data.

Due to their capability to handle discrete design variables and search for global solutions without using gradient information, GAs have been widely used in sensor placement type problems (Padula and Kincaid, 1999; Abdullah et al., 2001; Guo et al., 2004), sometimes combined with gradient-based methods (Padula and Kincaid, 1999; Abdullah et al., 2001). Abdullah et al. (2001) addressed the necessity to use GAs for placement of sensors/actuators on civil structures, members of which are usually discrete and therefore discrete locations are available for sensors/actuators. Guo et al. (2004) presented an improved GA for the global and constrained optimization of sensor locations for structural health monitoring systems. The performance function was based on damage detection. To overcome the inefficiency due to infeasible solutions to the problem, some improved strategies were used, such as crossover based on identification code, mutation based on two gene bits, and improved convergence. They concluded that the improved GA is faster than the penalty function method and the forced mutation method.

In the early GA researches, genetic representation of a chromosome or a solution was limited to binary digits (Holland, 1975; Michalewicz, 1994; Houck et al., 1995), but problem representation has been the subject of much investigation (Houck et al., 1995). It has been shown that more natural representations are more efficient and produce better solutions (Michalewicz, 1994). One useful representation of an individual or chromosome for function optimization involves genes or variables from an alphabet of floating point numbers with values within the variables' upper and lower bounds. Michalewicz (1994) has done extensive experimentation comparing real-valued and binary GAs and shows that the real-valued GA is an order of magnitude more efficient in terms of CPU time. He also shows that a real-valued representation moves the problem closer to the problem representation which offers higher precision with more consistent results across replications (Michalewicz, 1994). Along this line, Zhang et al. (2000) presented a novel float-encoded GA and applied it to the optimal control of flexible smart structures bonded with piezoelectric actuators and sensors. The performance function was based on the maximization of dissipation energy due to a control action. The optimization algorithm allowed an integrated determination of actuator and sensor locations and feedback gains.

Padula and Kincaid (1999) provided a survey of actuator and sensor placement problems from a wide range of engineering disciplines (both aerospace and non-aerospace engineerings) and a variety of applications. Combinatorial optimization methods are recommended as a means for identifying sets of actuators and sensors that maximize performance. Frecker (2003) reviewed the work done in this area since 1999 to 2003, in addition to optimization strategies for topology design of actuators, actively controlled structures, and drive electronics design.

This study addresses the placement optimization of a distributed sensing fiber optic sensor for its potential usage in human-machine systems, such as pilot/passenger seats, and structures for flight vehicles though it was initially developed by Spillman Jr. et al. (2004) for a clinical smart bed. The fiber optic sensor is used to both sense the movement and determine the posture of the human body. For the clinical smart bed, for example, the

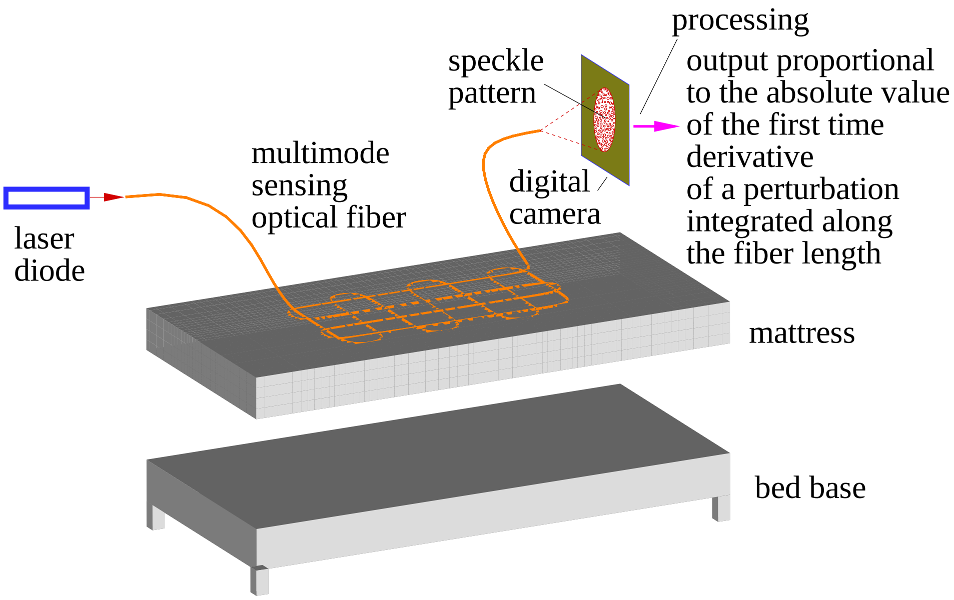

Figure 3.1: A schematic diagram of the smart bed. The distributed sensing fiber optic cable is stitched on the bed surface.

sensor can be used to monitor the movement of a patient and determine whether or not the patient is lying on his/her sides, stomach or back. The sensor can be even used to measure the breathing and heart rates. Proven to be a success as a concept, it requires a design methodology and tool to optimally place the fiber optic sensor to maximize its performance. Figure 3.1 is a schematic diagram of the distributed sensing fiber optic sensor on the smart bed. The output of the distributed sensing fiber optic sensor, which consists of an infinite number of infinitesimal sensors continuously connected together, is proportional to the absolute value of the first time derivative of the integrated spatial perturbation along the fiber, as presented by Spillman Jr. et al. (2004) and shown in Fig. 3.1. For placement optimization purpose, the sensor performance is simplified to be the integrated absolute curvature change of the fiber optic cable with respect to a perturbation due to the body movement of a patient lying on it.

The fiber optic cable is represented by a NURBS curve (Farin, 1990) that is uniquely determined by a finite number of control points. This make it possible to convert the placement optimization of an infinite number of sensors to the placement optimization of a finite number of control points of a NURBS curve. Therefore, one can successfully use the popular GAs (Markus et al., 1997; Faupel, 1998; Gürdal et al., 1999) to obtain the optimal placement of the distributed sensing fiber optic senor.

We model the smart bed as an elastic mattress core and ignore the flexible cover. The initial and deformed geometries of the bed due to the body weight and movement of the patient are calculated, using the finite element analysis tool, MSC.NASTRAN, from the given body pressure distribution (Nicol and Rusteberg, 1993). The deformations of the fiber optic cable are then extracted from the deformations of the mattress.

An interactive Java tool is developed to implement the above ideas. Illustrative examples are given to demonstrate the validity of the presented method.

Though the specific example is for clinical use, the fiber optic sensor and associated placement methodology can also be used in pilot/passenger seats and structures for flight vehicles. The other potential use is the placement of Fiber Bragg Grating (FBG) sensors for health monitoring structures in both aerospace engineering (Davisy et al., 1996) and civil engineering (Udd et al., 1998; Lin et al., 2005).

3.2 Description of the Problem

3.2.1 Objective/Sensor Performance Function

The concept of the distributed sensing fiber-optic sensor is based on mode *angle shifting* of a multimodal optical fiber. When the fiber pattern on the smart bed is perturbed by the motion, due to either respiration or heartbeat, the *radius of the annulus* (a ring-like output light signal figure projected on a flat surface) increases. As a result, if a special fiber is used that only intercepts a portion of the annular or speckle pattern of this light and allows this intercepted light to pass to a detector, an output signal will result in continuing information about the perturbation that caused the change in the signal, See Fig. 3.1. This output, *e.g.* the change in the *radius of the annulus*, is proportional to the absolute value of the first time derivative of the integrated spatial perturbation along the fiber (Spillman Jr. et al., 2004). That is, the whole output of this distributed sensing optical fiber is the sum of the outputs of an infinite number of infinitesimal fiber segments. The contribution of each infinitesimal fiber segment to the output is proportional to its spatial perturbation that is the angular change of the fiber segment.

For the placement optimization of the sensor, the experimentally verified physical law for the sensor output (Spillman Jr. et al., 2004) is simplified as: the *sensor performance function* is the sum of the absolute *angular change* $\mathrm{d}\theta = ||\Delta\kappa(s)||_2 \mathrm{d}s$ over an infinite number of the infinitesimal fiber segments ds'. That is, the performance of the whole distributed sensing fiber optic sensor is the integration of the absolute curvature change due to a given spatial perturbation over the whole fiber length L:

$$\Delta\bar{\theta} = \int_0^L ||\Delta\kappa(s)||_2 \mathrm{d}s \tag{3.1}$$

where $\Delta\kappa(s) = \Delta\kappa_x(s)\mathbf{i}_x + \Delta\kappa_y(s)\mathbf{i}_y$ is the curvature (vector) change of the fiber segment ds, as the dominant spatial perturbation.

3.2.2 Design Variables/Placement Representation

Since a distributed sensing fiber optic sensor consists of an infinite number of infinitesimal sensing fiber segments, the placement of those infinite number of sensors seems to be extremely hard. We can, however, transfer the placement of an infinite number of sensors to the placement of a finite number of the *control points* - "dummy sensors", if we represent

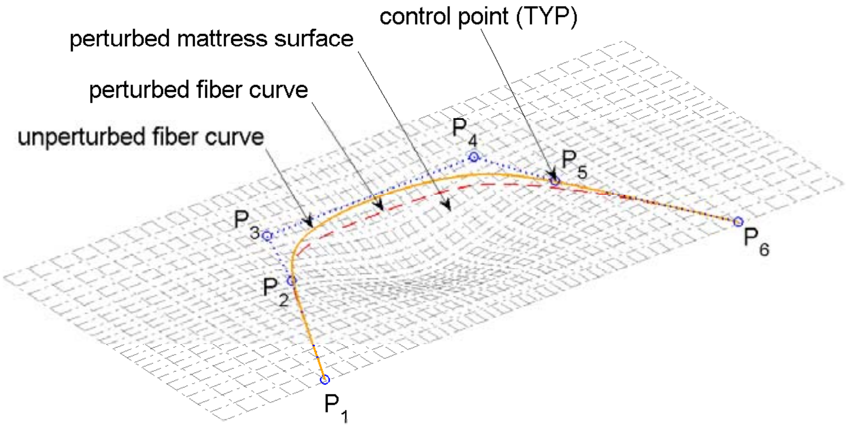

Figure 3.2: A possible fiber optic sensor placement represented by a NURBS curve.

the fiber curve using a NURBS curve, which can be expressed mathematically by

$$\mathbf{C}(s) = \frac{\sum_{i=0}^{n} N_{i,p}(s) w_i \mathbf{P_i}}{\sum_{i=0}^{n} N_{i,p}(s) w_i} \tag{3.2}$$

where p and q are the polynomial degrees, $N_{i,p}$ and $N_{j,q}$ are the B-Spline basis functions, $\mathbf{P_i}(s) = X_i(s)\mathbf{i}_x + Y_i(s)\mathbf{i}_y$ are the *control points*, the weights w_i of $\mathbf{P}_i$ are the last coordinate of homogeneous point $\mathbf{P}_i^w$ [1] (Farin, 1990). Refer to Fig. 3.2 for a fiber optic sensor placement represented by a NURBS curve with only 6 control points.

---

[1] There are two different conventions for representing the control points in terms of their 4D coordinates (x, y, z, w):
Homogeneous, in which the coordinates represent the point's position in 4D space. Thus the point's 3D position is $(x/w, y/w, z/w)$.
Weighted Euclidean, in which the coordinates are already considered to have been divided through. Thus the first three components (x, y, z) directly represent the point's position in 3D space and the fourth w represents its weight.

3.2.3 Constraints

Geometrical constraints

For a given placement of the sensing fiber, there is a geometric constraint on it, that is, the optical fiber cable remains in contact with the mattress surface. Although the actual fiber optic cable may slip on the mattress, it is assumed that the fiber cable remains adhered to the mattress for simplicity in this study.

The mattress surface is assumed to be initially flat. The mattress surface and the fiber optic sensor curve on it deform after the patient lies down on the bed. The deformed mattress surface can be assumed to be a general surface that can be represented by a NURBS surface or be determined from FEA for a given body pressure.

The deformed mattress surface is further changed due to a dynamic perturbation, such as the respiration and heart beat of the patient. This deformed surface after perturbation can be further determined from FEA for the given pressure perturbation.

For a fixed local curvature change of the deformed mattress surface, the longer the fiber is, the larger the total curvature change will tend to be. Therefore, we might consider using a longer fiber optic cable to get a better performance of the sensor. However, we need to put a constraint on the maximum length due to cladding mode lost or laser power limit; *e.g.* we can set $L \leq L_{max}$, where L_{max} is usually on the order of several meters.

Physical and mechanical constraints

Because the optical fiber and mattress membrane are very thin, the lateral (shearing and bending) stiffnesses of the fiber and mattress cover are negligible. Since the mattress cover is easy to wrinkle, the in-plane stiffness of the cover may also be ignored. This assumption makes it possible to perform only one FEA for a given body pressure distribution during the whole optimization process since a change in placement of the fiber optic cable will not change the deformed shape of the mattress surface. This makes using a global searching GA possible.

A *micro bend* design may be useful to enhance the sensor performance. However, the initial curvature or radius of the sensing fiber is subject to the limitation due to *bending losses* (Udd, Schulz, Seim, Corones, and Laylor 1998).

3.3 Procedure and Implementation

3.3.1 Procedure

Refer to Fig. 3.3 for a simplified flow chart of the procedure for the optimal placement of the fiber optic cable.

Step 1. Choose a mattress model

Two main classes of bed mattresses are spring cored and foam-filled cored, respectively. Practically speaking, the covers of all mattresses are woven of certain materials. For this study, we choose a core material with material data given in Table 3.1 to model the mattress of a standard size 198cm × 91.5cm × 16.5cm (78” × 36” × 6.5”).

Step 2. Determine the body pressures due to the self-weight and perturbation by measurement or numerical simulation

The self-weight induced body pressure and perturbed body pressure on the mattress surface can either be determined by experimental measurements or by numerical simulations. For

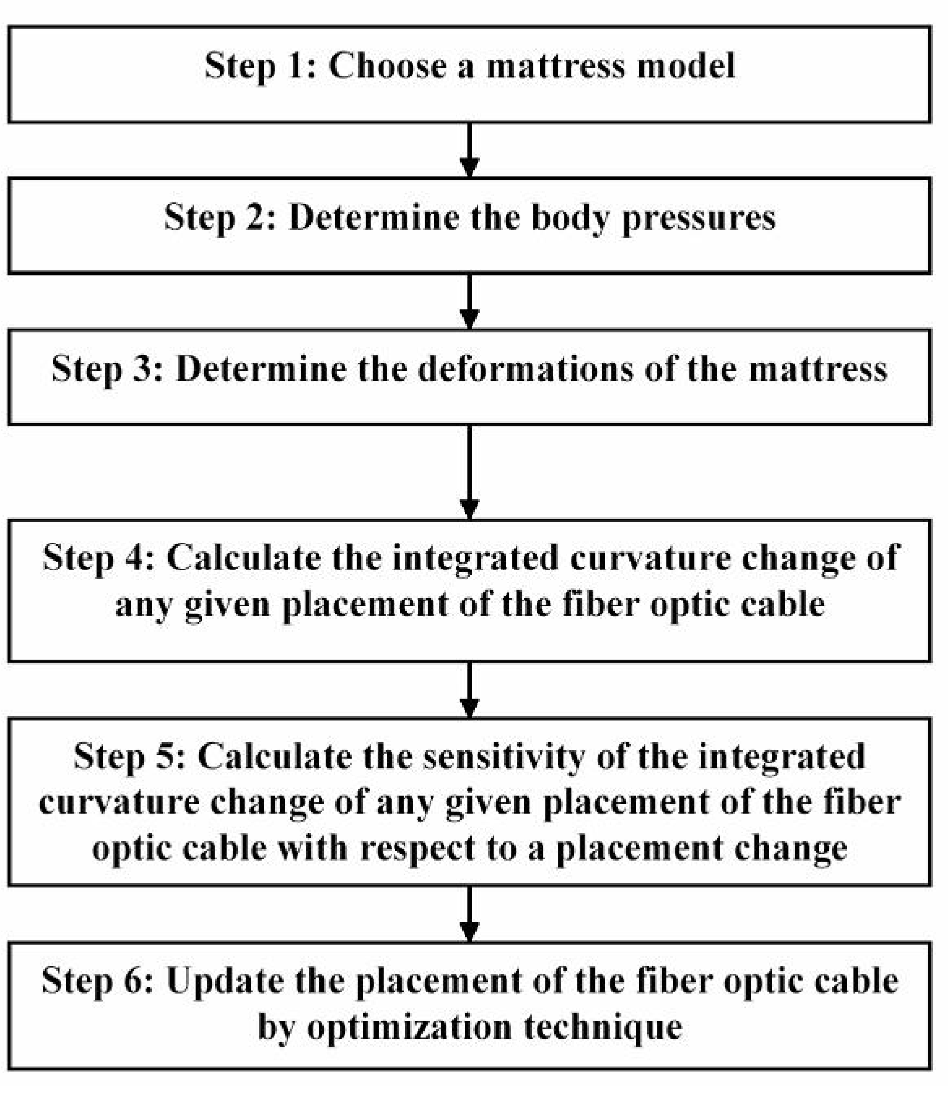

Figure 3.3: Chart for optimal placement of the fiber optic sensor.

Table 3.1: Latex Mattress Core Fact Sheet.
Standard Hardness Specifications for Mattress Cores

Hardness Range	(ILD= Indentation Load Deflection)
Soft	20-24 ILD
Medium	25-29 ILD
Firm	30-34 ILD
Extra Firm	35-39 ILD
Super Firm	40-44 ILD

Hardness range measurements based on ASTM D-1055
Source: http://www.flobeds.com/mattspec.htm

illustrative purpose and initial study, we can assume a simple body pressure distribution (Nicol and Rusteberg, 1993) on the mattress, for example, given in the form of a NURBS surface within a given area, which can practically model all kinds of pressure distributions.

Our numerical studies showed that the contribution of the initial deformation of the mattress to the sensor performance is small. Therefore, we only consider the perturbed body pressure for linear analysis.

Step 3. Determine the deformations of the mattress subjected to the body pressures by MSC.NASTRAN

A linear analysis was performed to obtain the deformation of the mattress subjected to a given pressure distribution pattern with unit maximum value. FEM model: $70 \times 30 \times 4 = 8,400$ brick elements for the mattress core; the cover is ignored. Mattress core hardness is assumed to be soft and taken from Table 3.1 and transferred into Young's modulus as in Table 3.2.

Applied pressure and mattress deformation are shown in Fig. 3.4 and Table 3.2.

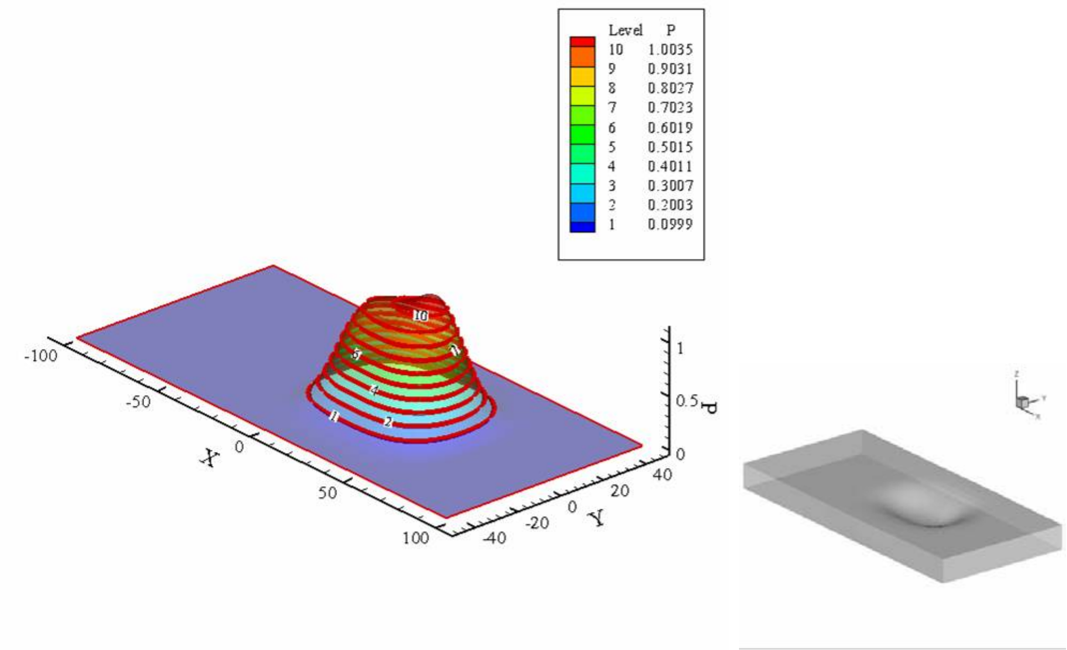

(a) Body pressure.

(b) Deformation.

Figure 3.4: Body pressure and deformation of the soft cored mattress. The pressure P has a unit of N/cm^2.

Table 3.2: Latex Mattress Core Fact Sheet.

Mattress core hardness and calculated maximum deformations
under the assumed body pressure (with the maximum value of 1.00N/cm^2)

Hardness Range	E = Young's Modulus (N/cm^2)	Maximum deflection (cm)	Maximum nominal strain
Soft	1.213	15.0	0.909
Medium	1.493	12.2	0.739
Firm	1.765	10.3	0.624
Extra Firm	2.041	8.92	0.541
Super Firm	2.317	7.86	0.476

Note:
(1) *The typical values of Young's modulus E are calculated from Table 3.1*
(2) *Poisson's ratio* $\nu = 0.3$ *for latex rubber foam is from Fig. 12 of Roberts and Garboczi (2002).*

Step 4. Calculate the integrated curvature change of any given placement of the fiber optic cable due to the body pressure perturbation

Assume that the fiber cable remains adhered to the mattress surface without slipping. Then, we can easily extract the relevant fiber curve deformations from the initial and perturbed mattress deformations. We can thereafter calculate the sensor performance, *i.e.*, the integrated curvature change, for given design variables – the locations of control polygons of the NURBS curve.

Step 5. Calculate the sensitivity of the integrated curvature change of any given placement of the fiber optic cable with respect to a placement change by finite difference method

This step is to calculate the design sensitivity of the objective function with respect to design variables. However, we ignore this step as we are using GAs.

Step 6. Update the placement of the fiber optic cable by optimization technique

An optimizer (Gürdal et al., 1999) is used to update the placement of the fiber optic cable and give a better design than the previous one. A GA (Faupel, 1998) is chosen as the optimizer.

3.3.2 Implementation

The interactive design tool "Java Tool for the Placement of Fiber Optic Sensors" is developed in Java, aiming at the implementation of Steps 4, 5 and 6 of the procedure: for any given initially deformed mattress surface and any given placement of the fiber optic cable constrained on the mattress, we shall be able to calculate the integrated curvature change of the fiber optic cable due to any perturbation of the mattress surface and its sensitivity with respect to a design change, so that we are able to update the placement of the fiber optic cable to a better design both manually and by the optimization technique, *e.g.* GA.

3.4 Placement Optimization of the Fiber Optic Sensors for a Smart Bed by GA

To demonstrate the current capability of the interactive Java tool for the placement optimization of fiber optic sensors, an illustrative example is given here.

The Genetic Algorithm optimizer, GAJIT, the Java package kindly provided by Faupel (1998), is used to optimize the placement of the fiber curve.

3.4.1 A Very Simple Breeding Algorithm

Not addressing efficiency in this study, we only use a very simple breeding algorithm in GAJIT to illustrate applying GAs to a NURBS curve design as follows:

- Remove a percentage of the least fit designs through culling;
- Preserve a percentage of the most fit designs unchanged (elitism);
- Then breed the elite and the remainder at random to fill out the rest of the next generation.

The relevant parameters for the GA used here are:

- Culling rate: percentage deemed unfit for reproduction;

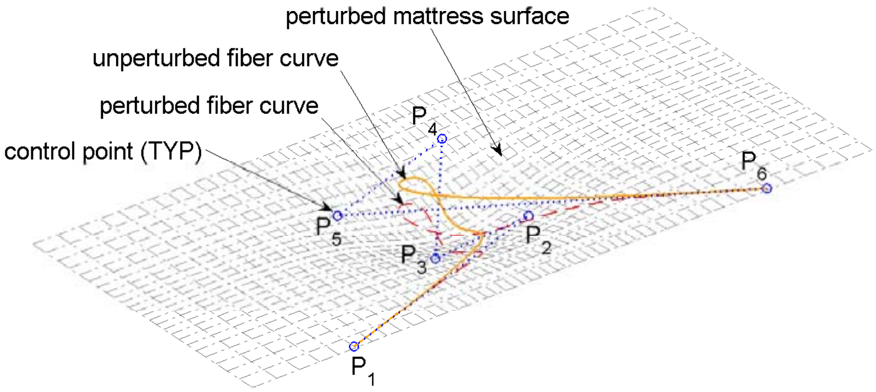

Figure 3.5: A placement of a fiber optic sensor for a smart bed represented by a NURBS curve with 6 control points. Adopted from Fig. 3.7b.

- Elite rate: percentage of population carried forward unchanged from each generation;
- Weight: the weighting it has for the chances of it being selected.

3.4.2 Coding/Decoding

A typical GA is only suitable for discrete design variables. To apply a GA to an optimization problem of continuous design variables, we can approximate the continuous design variables using discrete ones.

For the placement of the fiber optic sensor, we choose two components (X, Y) of the (4 out of 6 in Fig. 3.5) control points of the fiber NURBS curve as design variables (the two ends are fixed). The scaled coordinate components are $-1 \leq \bar{X} = 2X/L_{\text{mattress}} \leq 1$ and $-1 \leq \bar{Y} = 2Y/W_{\text{mattress}} \leq 1$, where L_{mattress} and W_{mattress} are the length and width of the mattress, respectively. We code the design variables

$\bar{\mathbf{X}}_{10} = [0.0968 \quad -0.4194 \quad -0.2258 \quad -0.4839 \quad 0.1613 \quad 0.5484 \quad -0.2903 \quad 0.2258]_{10}$
using the genes (*e.g.* the gene size is 5) of a chromosome represented by a binary string:
$\bar{\mathbf{X}}_2 = [10011 \quad 01011 \quad 11000 \quad 10010 \quad 01000 \quad 01100 \quad 01001 \quad 10001]_2$

Each chromosome, for example, represents one of the 20 members of the population.

Any chromosome $\bar{\mathbf{X}}_2$ has to be decoded back to its counterpart $\bar{\mathbf{X}}_{10}$ for evaluation of the fitness of the chromosome.

3.4.3 Fitness Function

The fitness function for the GA is defined in the sense of the so-called exact penalty function method:

$$\begin{aligned}\text{Fitness} \quad = \quad & \frac{\int_0^L ||\Delta\kappa(s)||_2 \mathrm{d}s}{L_{\max}} \cdot \\ & [1 - p_\kappa \max(\frac{\kappa_{0\max}}{\kappa^u_{0\max}} - 1, 0) - p_L \max(\frac{L}{L_{\max}} - 1, 0)]\end{aligned} \tag{3.3}$$

where

$$\Delta\bar{\theta} = \int_0^L ||\Delta\kappa(s)||_2 \mathrm{d}s$$

according to Eq. (3.1), is the sensitivity of the fiber topic sensor due to a given body perturbation. L and $L_{\max}$ are the current and maximum allowed lengths of the fiber curve, respectively. $\kappa_{0\max}$ and $\kappa^{\mathrm{u}}_{0\max}$ (= 0.5/cm) are the maximum and the maximum allowed initial curvatures of the fiber curve, respectively. p_L and p_κ are the corresponding penalty factors.

3.4.4 Examples

Example 1. The assumed perturbed surface is from the initial flat surface of the NURBS with 7×5 **uniformly distributed control net by an** 18.00cm **downward perturbation of the control point at the center of the mattress. Only 6 control points of the fiber NURBS curve are used, two ends of which are fixed.**

$L_{\max} = 200\text{cm}$; $p_L = 1$ and $p_\kappa = 1$; the elite rate, culling rate and weight are 0.05, 0.2 and 0.1, respectively. Figure 3.6 shows the example of the placement optimization of a fiber optic sensor for a smart bed by GA. It is shown that the initial placement of the fiber curve is

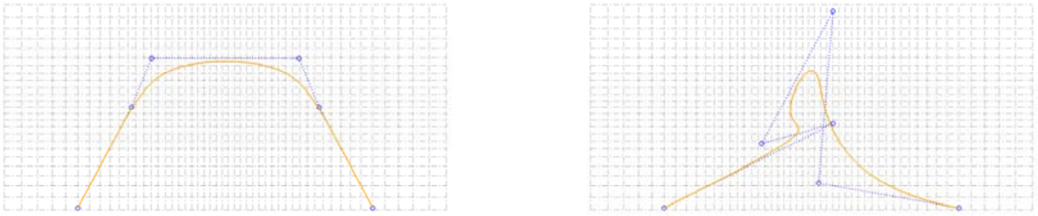

(a) An initial placement: $\Delta\hat{\theta} = 0.29$ (rad); $L = 200.55$ (cm); $\kappa_{0\max} = 0.04$ (1/cm).

(b) After 500 generations: $\Delta\hat{\theta} = 1.94$ (rad); $L = 198.58$ (cm); $\kappa_{0\max} = 0.50$ (1/cm).

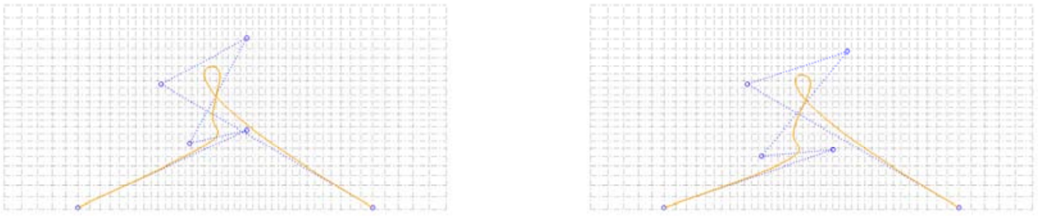

(c) After 1000 generations: $\Delta\hat{\theta} = 2.30$ (rad); $L = 207.67$ (cm); $\kappa_{0\max} = 0.49$ (1/cm).

(d) After 2000 generations: $\Delta\hat{\theta} = 2.37$ (rad); $L = 202.83$ (cm); $\kappa_{0\max} = 0.46$ (1/cm).

Figure 3.6: Placement optimization of a fiber optic sensor for a smart bed by GA.

feasible but with a lower sensitivity of 0.29rad, a length of 200.55cm, and maximum initial curvature of 0.04/cm. After 2000 generations of the GA iteration, an updated placement is achieved, with a higher sensitivity of 2.37rad, a length of 202.38cm, and maximum initial curvature of 0.46/cm. Figure 3.7 is a 3-D view of the initial placement and updated placement after 2000 generations of the GA iteration. We can see clearly that the initial placement of the fiber optic sensor is inefficient due to the fact that most of the sensing fiber is in a much less perturbed region. After 2000 generations of the GA iteration, much of the sensing fiber falls into a highly perturbed region with a higher curvature change.

Example 2. The assumed perturbed surface is obtained by a 10% scaling of the calculated deformation of the soft cored mattress under an assumed body pressure as shown in Fig. 3.4**. Only 25 control points of the fiber NURBS curve are used, two ends of which are fixed.**

$L_{\max} = 400$cm; $p_L = 4$ and $p_\kappa = 2$; the elite rate, culling rate and weight are 0.05, 0.2 and 0.1, respectively. Figure 3.8 shows the example of the placement optimization of a fiber optic sensor for a smart bed by GA. It is shown that the initial placement of the fiber curve is feasible but with a lower sensitivity of 1.01rad, a length of 358.95cm, and maximum initial curvature of 0.49/cm. After 9000 generations of the GA iteration, an updated placement is achieved, with a higher sensitivity of 1.51rad, a length of 358.95cm, and maximum initial curvature of 0.49/cm. Figure 3.9 is a 3-D view of the initial placement and updated placement after 9000 generations of the GA iteration. We can also see clearly that the initial placement of the fiber optic sensor is less efficient due to the fact that one part of the sensing fiber is in an unperturbed region. After 9000 generations of the GA iteration, that part of the sensing fiber approaches the perturbed region and the overall sensing fiber tends to form a star-like pattern in the perturbed region.

3.5 Conclusions

- The deformation of the smart bed is simulated by finite element analysis (*e.g* using MSC.NASTRAN) when the body pressure is available.
- Both deformed area of the bed surface and fiber optic cable are represented by NURBS.
- A Java tool is developed as an interactive research and design tool for the fiber optic sensor.
- The sensitivity of the fiber optic sensor is indirectly represented by the integration of the absolute curvature change over the curve length.
- The Genetic Algorithm (GA) is chosen as the optimizer for the placement optimization of the fiber optic sensor.
- The fitness function of the GA is defined in the sense of the exact penalty function method, where the length and maximum initial curvature of the fiber curve are limited by prescribed upper bounds.
- Illustrative examples are given for the demonstration of the placement optimization of the fiber optic sensor.

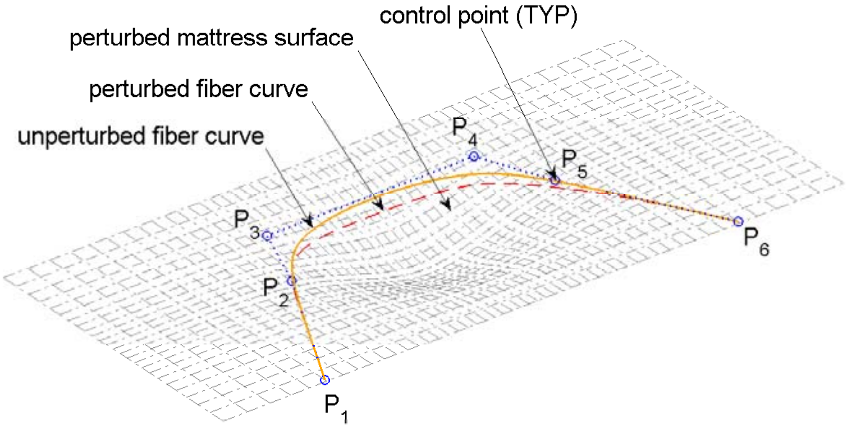

(a) An initial placement.$\Delta\hat{\theta} = 0.29$ (rad).

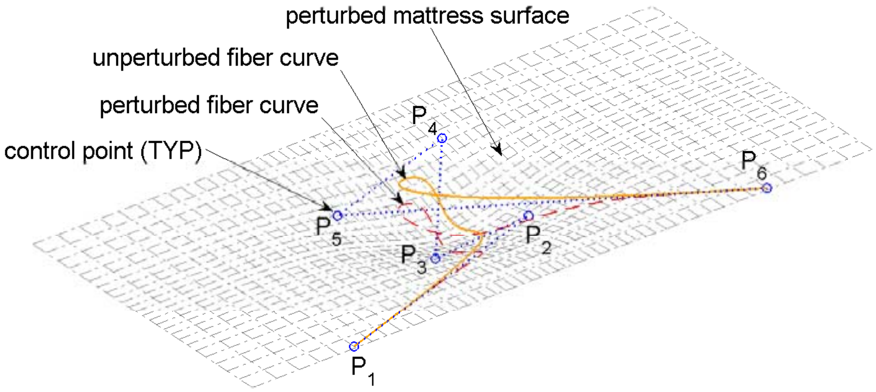

(b) An updated placement after 2000 generations of GA iteration. $\Delta\hat{\theta} = 2.37$ (rad)

Figure 3.7: A 3-D view of the initial placement and updated placement. The perturbed (dashed) and unperturbed (solid) fiber curve shapes of the optimal placement of the fiber optic sensor.

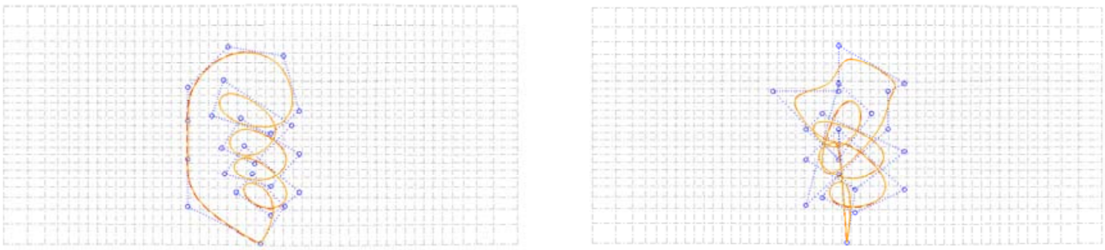

(a) An initial placement: $\Delta\hat{\theta} = 1.01$ (rad); $L = 358.95$ (cm); $\kappa_{0\max} = 0.49$ (1/cm).

(b) After 5000 generations: $\Delta\hat{\theta} = 1.32$ (rad); $L = 386.33$ (cm); $\kappa_{0\max} = 0.49$ (1/cm).

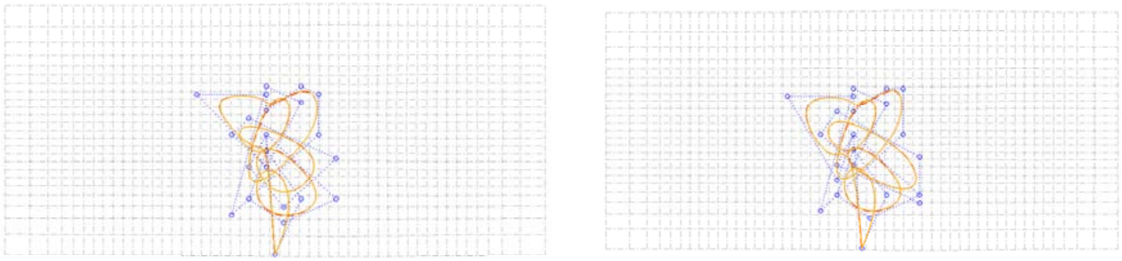

(c) After 7000 generations: $\Delta\hat{\theta} = 1.47$ (rad); $L = 386.09$ (cm); $\kappa_{0\max} = 0.49$ (1/cm).

(d) After 9000 generations: $\Delta\hat{\theta} = 1.51$ (rad); $L = 399.99$ (cm); $\kappa_{0\max} = 0.49$ (1/cm).

Figure 3.8: Placement optimization of a fiber optic sensor for a smart bed by GA.

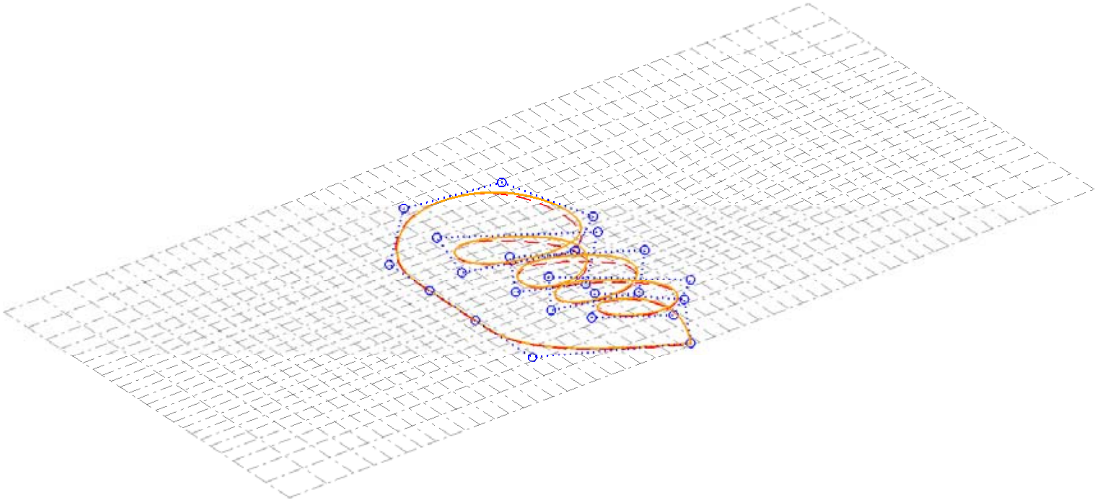

(a) An initial placement. $\Delta\hat{\theta} = 1.01$ (rad).

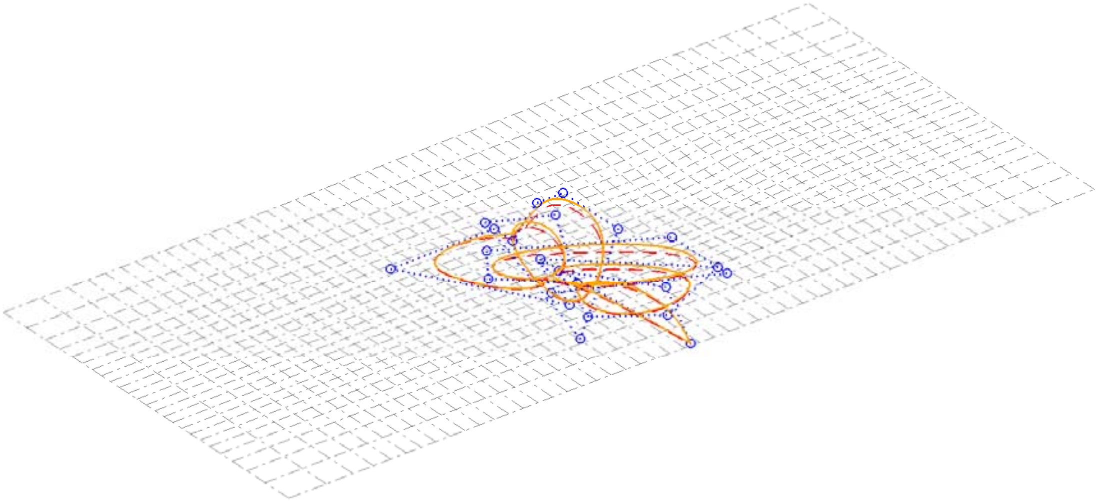

(b) An updated placement after 9000 generations of GA iteration. $\Delta\hat{\theta} = 1.51$ (rad).

Figure 3.9: A 3-D view of the initial placement and updated placement. The perturbed (dashed) and unperturbed (solid) fiber curve shapes of the optimal placement of the fiber optic sensor.

Chapter 4
Optimal Design of Unitized Panels with Curvilinear Stiffeners

In this chapter, we show many numerical results of optimal design study of stiffened panels where the reference axes of the stiffeners can be curvilinear. An integrated approach to use different capabilities in relevant fields, such as NURBS, DistMesh, and MSC.NASTRAN, etc., are adopted in the MATLAB environment. Numerical studies are made to look into the effects of certain factors on the optimal designs of stiffened panels under buckling constraints. Those factors include orientation, spacing, location, and curvature. It is observed that curvilinear placement of stiffeners is equivalent to an orientation, spacing, location and intersection placement of infinitesimal straight and connected stiffeners, and provides an enhanced design space. This enhanced design space sometimes leads to better designs than purely using straight stiffeners. This work reconfirms the necessity to use global optimization techniques to perform topology/placement/shape optimization of curvilinearly stiffened panels along with size optimization.

4.1 An Overview

Availability of high-performance computing and commercially available software, such as MSC.NASTRAN and MATLAB, is having enormous impact on the manner how structures are designed. Similarly, the ongoing revolution in computer-aided manufacturing has significantly removed the previous limitations on the design and manufacturing of a structure. For example, using Electronic Beam Freeform Fabrication (EBF3), a rapid metal deposition process that works efficiently with a variety of weldable alloys (Taminger and Hafley, 2003), allows the stiffeners of a panel to have continuously varying properties such as orientation, thickness, width, and material properties. These design parameters are mostly kept constant in earlier studies because of manufacturing constraints. Together, the software for computer-aided design, engineering and manufacturing (CAD/CAE/CAM) are bound to play a major role in the design of all future aerospace and other related structures. We envision an environment in which design and manufacturing, using modern information technology, would be integrated into one step, which also follows the modern trend for the unitized parts for flight vehicles structures (Renton et al., 2004). Here, we address the integrated capability of CAD and CAE implemented in the MATLAB environment to provide a methodology and a practical design toolbox, *EBF3paneloptimization*, for optimization of unitized panels with stiffeners, especially, manufactured by the EBF3 technique. Though the development of *EBF3paneloptimization* is still in progress, we have used it to run numerous examples to confirm the important effects of the stiffeners' orientation, spacing, location, and curvature, etc., on the optimal design of a stiffened panel.

Although our current effort has been only partially automated and mainly dealt with planar stiffened panels, the extension can be made to implement the automatic placement and size optimization of both planar and curvilinear stiffened panel as shown in Fig. 4.1, and thus provide a capability to design advanced unitized curved panels with curvilinear stiffeners. This is an extension to optimize low-cost high-performance panels that have a grid of stiffeners with a prescribed uniform or non-uniform pattern, such as isogrid and geodesically stiffened panels (Gerdon and Gürdal, 1985; Grall and Gürdal, 1992; Gürdal and Gerdon, 1993).

Advances in manufacturing and computer-aided design and engineering are making it possible to fabricate these advanced unitized structures.

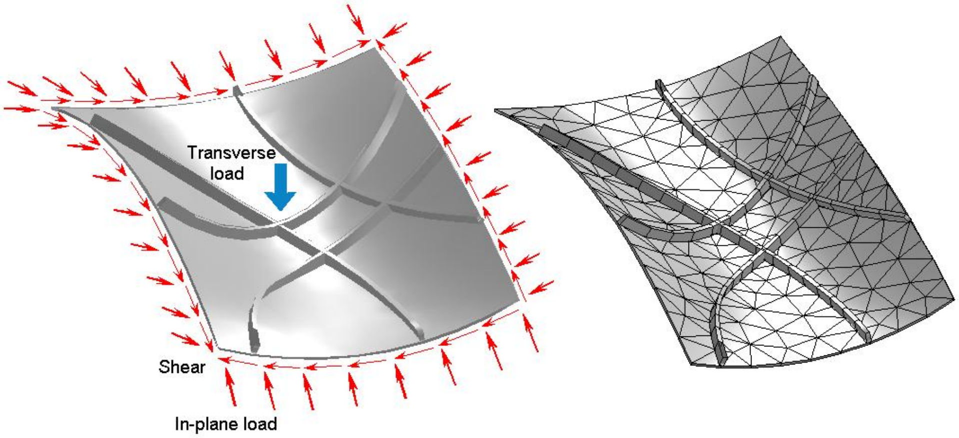

Figure 4.1: A curved panel with arbitrarily oriented stiffeners and its finite element mesh.

4.2 Methodology, Procedure, and Capability

4.2.1 Methodology

The methodology used here does not focus on developing new theories, numerical methods, and self-written in-house codes to achieve the solution to the stiffened panel optimization, as that would only limit the capability of solving various practical problems. Instead, we seek an integration of the advanced capabilities in CAD/CAE/CAM in the versatile MATLAB environment to develop the proposed tool to design and fabricate advanced unitized structures.

4.2.2 Procedure

The present work implemented NURBS (Non-Uniform Rational B-Splines) (Farin, 1990; Spink, 2000; Li et al., 2004) for the representation of the panel mid-surface/thickness distributions and stiffeners' reference curves/cross-sectional dimension distributions. In a reference plane, the mesh for any stiffener is first generated in a separate routine that creates its NURBS representation, and then the mesh for the plate is generated using automatic mesh generation algorithm. We have adapted DistMesh, a MATLAB code for generation of unstructured triangular /tetrahedral meshes by Persson and Strang (2004), with stiffeners' mesh points fixed during the plate meshing. The planar reference mesh for the stiffened panel is mapped into a curved NURBS surface by using bilinear interpolation. An interface between MSC.NASTRAN and MATLAB is developed to automatically transfer the data between the analysis and optimization processes, respectively. A simple but helpful MATLAB 3D display package is also developed for a better visualization of the initial and final designs.

The whole package, called *EBF3paneloptimization*, however, is not any isolated capability of a NURBS package, a simple DistMesh, the MSC.NASTAN, a NASTRAN/MATLAB interface, or a 3D panel display package, but an integrated package of all those advances. Without this integration, handling this arbitrarily curved stiffened panel optimization at hand will be a hard and time consuming job. MATLAB, the Language of Technical Computing with toolboxes of high performance for numerical simulations and graphic/external interfaces, is taken as the main programming language. The NURBS toolbox, DistMesh code, 3D display package, MSC.NASTRAN, etc, are taken as the modules of the whole package.

4.2.3 Capability and Limitation

Various examples were simulated to test the current sizing optimization capability, and to study effects of orientation, spacing, location, and curvature of a stiffener on the optimal designs to illustrate the strong need to perform an automatic placement (or shape) optimization of stiffeners for a panel.

By manually updating one or two design parameters that determine the control points of stiffeners' NURBS curves, we have performed some placement optimizations of the stiffeners for given end locations of stiffeners along the plate boundary edges. The pure shear, bi-normal, and complex combined in-plane loadings are considered.

4.3 Mathematical Aspects of Optimization of Stiffened Panels

4.3.1 Formulation of Optimization of Stiffened Panels

The optimization of EBF3 stiffened panels can be briefly formulated as follows, for instance:
Find X, which are a collection of the thickness distribution t of the plate, the cross-sectional dimension distributions, *e.g.* $(w,h)^{st}$, of a (blade) stiffener *st*, along the stiffener's axis, and the position vector distribution $\mathbf{c}^{st}$ of a point that represents the stiffener's axis or reference curve, to

Minimize:

$$F(\mathbf{X}) = M = \underset{\text{mass of plate}}{\rho^{\text{plate}}abt} + \sum_{st=1}^{N_{ST}} \underset{\text{mass of a stiffener}}{\rho^{st}L^{st}h^{st}w^{\text{st}}} \tag{4.1}$$

which is the mass, one of the possible objective functions of the stiffened panel,

Subjected to the constraints on the predetermined types of responses, *e.g.* buckling load factor,

$$\lambda \geq \lambda_{\mathrm{L}} \tag{4.2}$$

von-Mises stress constraint on the plate (and stiffeners),

$$\sigma_{\mathrm{L}} \leq \sigma_{\mathrm{von-mises}} \leq \sigma_{\mathrm{U}} \tag{4.3}$$

side constraints on size design variables,

$$t_L \leq t \leq t_U; \quad w^{\mathrm{st}}_{\mathrm{L}} \leq w^{\mathrm{st}} \leq w^{\mathrm{st}}_{\mathrm{U}}; \quad h^{\mathrm{st}}_{\mathrm{L}} \leq h^{\mathrm{st}} \leq h^{\mathrm{st}}_{\mathrm{U}} \tag{4.4}$$

and side constraints on the shape design variables

$$\mathbf{c}^{\mathrm{st}}_{\mathrm{L}} \leq \mathbf{c}^{\mathrm{st}} \leq \mathbf{c}^{\mathrm{st}}_{\mathrm{U}} \tag{4.5}$$

Here, all the pre-determined responses are evaluated by MSC.NASTRAN (MSC.Software, 2005), which also utilizes the DOT optimization algorithms from VR&D (1999) to solve the predetermined optimization problem.

4.3.2 Convergence of Optimization of Stiffened Panels

Slow convergence and instability of the solution are often encountered in numerical computations, which cannot be solved using different optimization parameters and starting points due to the ill-posed nature of the stiffened panel optimization problem. Firstly, Eq. (4.1) shows that the objective function of mass is ill-posed by itself and makes the Hessian matrix have a very large condition number. This can be understood from Eq. (4.1), in which the condition number of the Hessian is 100:

$$F(\mathbf{X}) = 10000x_1^2 + x_2^2 \tag{4.6}$$

Secondly, the different parts of the stiffened panel have very different contributions to the objective function, the total mass of the panel:

$$\underset{\text{mass of plate}}{\rho^{\mathrm{plate}}abt} \quad >> \quad \underset{\text{mass of a stiffener}}{\rho^{st}L^{st}h^{st}t^{\mathrm{st}}} \tag{4.7}$$

Thirdly, there are very different design sensitivities of the objective with respect to (wrt) different design variables:

$$\underset{\text{wrt plate thickness}}{\frac{\partial M}{\partial t} = \rho^{\mathrm{plate}}ab} \quad ; \quad \underset{\text{wrt stiffener height}}{\frac{\partial M}{\partial h^{st}} = \rho^{st}L^{st}w^{st}} \quad ; \quad \underset{\text{wrt stiffener thickness}}{\frac{\partial M}{\partial w^{st}} = \rho^{st}L^{st}h^{st}} \tag{4.8}$$

and

$$\frac{\partial M}{\partial t}\Bigg/\frac{\partial M}{\partial h^{st}} = \frac{a}{w^{st}} >> 1; \quad \frac{\partial M}{\partial t}\Bigg/\frac{\partial M}{\partial w^{st}} = \frac{a}{h^{\mathrm{st}}} >> 1 \tag{4.9}$$

for $\rho^{\mathrm{plate}} = \rho^{st}$ and $L^{st} = a = b$.

To elucidate the numerical techniques for overcoming the convergence problem, we first give a general formulation of the optimization problem in the given design space to

Find

$$\mathbf{X} = \begin{pmatrix} x_1 & x_2 & \cdots & x_n \end{pmatrix} \tag{4.10}$$

Minimize

$$\text{Objective} = F(\mathbf{X}) \tag{4.11}$$

Subjected to

$$g_j(\mathbf{X}) \leq 0; \quad \text{for} \quad j = 1, 2,...,m \tag{4.12}$$

$$x_i^{\mathrm{L}} \leq x_i \leq x_i^U; \quad \text{for} \quad i = 1, 2,..., \mathrm{n} \tag{4.13}$$

The first technique involves scaling of design variables (Arora, 1989):

$$\mathbf{X} = \mathbf{Q}\mathbf{D}\bar{\mathbf{X}} \tag{4.14}$$

Note that the columns of $\mathbf{Q}$ are the eigenvectors of the Hessian matrix $\mathbf{H}$ of $F(\mathbf{X})$. $\mathbf{D} = \mathrm{diag}[1/\lambda_i]$ with λ_i^2 as the eigenvalues of $\mathbf{H}$. After the scaling, the condition number of the Hessian will be 1, which makes the problem well-conditioned.

The second technique is the simple scaling and shifting of the objective:

$$F(\mathbf{X}) = \alpha_f \bar{F}(\mathbf{X}) + \beta_f \tag{4.15}$$

The shifting is done to cause comparable contributions to the objective function and the scaling is used to give comparable sensitivities of the objective and constraints with respect to the design parameters.

The last technique proposed here is the shifting of the constraints so that the gradients of the normalized constraints are scaled:

$$g_j(\mathbf{X}) = \alpha_{g_j} \bar{g}_j(\mathbf{X}) + \beta_{g_j} \tag{4.16}$$

In this study, a simplified version of the numerical techniques to solve the convergence problem is used and illustrated for one blade stiffener case, as follows:

- For the panel problem with only one blade stiffener:

$$\mathbf{X} = (t, h^{\mathrm{st}}, w^{\mathrm{st}}); \quad \text{the starting point:} \quad \mathbf{X}_0 = (t_0, h_0^{\mathrm{st}}, w_0^{\mathrm{st}}) \tag{4.17}$$

- In $\mathbf{X} = \mathbf{Q}\mathbf{D}\bar{\mathbf{X}}$, for initial testing purpose, assume:

$$\mathbf{Q} = \mathbf{I}; \quad \mathbf{D} = \begin{bmatrix} \alpha & 0 & 0 \\ 0 & 1 & 0 \\ 0 & 0 & \beta \end{bmatrix} \tag{4.18}$$

That is, the plate thickness is scaled as $t = \alpha\bar{t}$ and the stiffener width is scaled as

$w^{\mathrm{st}} = \beta \bar{w}^{\mathrm{st}}$;

$$\frac{\partial M}{\partial \bar{t}} \Bigg/ \frac{\partial M}{\partial h^{st}}\bigg|_0 = \frac{\alpha ab}{w_0^{st} L^{st}} = \frac{t_0 b}{w_0^{st} L^{st}} = 1; \quad \frac{\partial M}{\partial \bar{t}} \Bigg/ \frac{\partial M}{\partial \bar{w}^{st}}\bigg|_0 = \frac{\alpha ab}{\beta h_0^{st} L^{st}} = \frac{t_0 b}{w_0^{st} L^{st}} = 1 \tag{4.19}$$

for $\rho^{\mathrm{plate}} = \rho^{st}$, $L^{st} = a = b$, and $t_0 = w_0^{st}$ if $\alpha = t_0/a$ and $\beta = w^{\mathrm{st}}/h^{\mathrm{st}}$.

Or

$$\frac{\partial M}{\partial \bar{t}} \Bigg/ \frac{\partial M}{\partial h^{st}}\bigg|_0 = \frac{\alpha ab}{w_0^{st} L^{st}} = \frac{t_0 a}{w_0^{st} L^{st}} = 1; \quad \frac{\partial M}{\partial \bar{t}} \Bigg/ \frac{\partial M}{\partial \bar{w}^{st}}\bigg|_0 = \frac{\alpha ab}{\beta h_0^{st} L^{st}} = \frac{t_0 a}{w_0^{st} L^{st}} = 1 \tag{4.20}$$

for $\rho^{\mathrm{plate}} = \rho^{st}$, $L^{st} = a = b$, and $t_0 = w_0^{st}$ if $\alpha = t_0/b$ and $\beta = w^{\mathrm{st}}/h^{\mathrm{st}}$.

Therefore, we have the comparable design sensitivities of the objective.

- To have comparable design sensitivities of the objective and constraints:
  - Make a test run of one iteration and print out the design sensitivities;
  - Scale and shift the objective function.

The numerical examples later on will show the benefits of the scaling and shifting on improving the convergence of the stiffened panel optimization using MSC.NASTRAN.

4.3.3 NURBS Representation of Stiffened Panels

The present work implemented NURBS (Farin, 1990; Spink, 2000; Li et al., 2004) for the representation of the panel mid-surface/thickness distributions and stiffeners' reference curves/cross-sectional dimension distributions. A NURBS curve (Fig. 4.2) is expressed mathematically by

$$\mathbf{C}(t) = \frac{\sum_{i=0}^{n} N_{i,p}(t) w_i \mathbf{P_i}}{\sum_{i=0}^{n} N_{i,p}(t) w_i} \tag{4.21}$$

and a NURBS surface (Fig. 4.3) is represented by

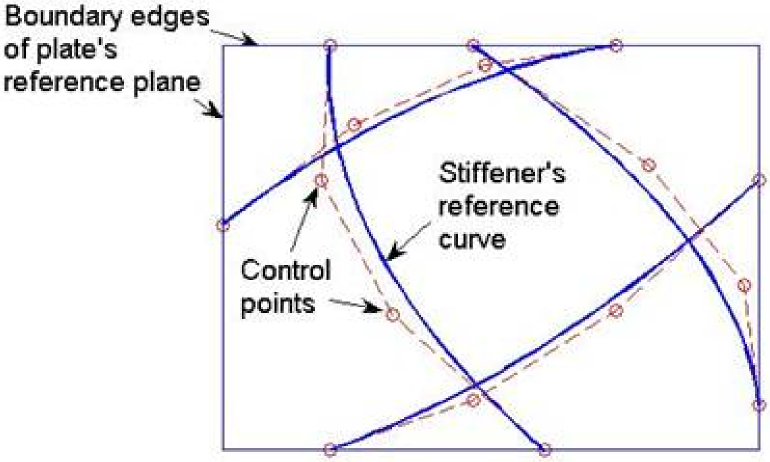

Figure 4.2: NURBS representation for stiffeners' reference curves.

$$\mathbf{S}(u,v) = \frac{\sum_{i=0}^{m}\sum_{j=0}^{n} N_{i,p}(u)N_{j,q}(v)w_{i,j}\mathbf{P_{i,j}}}{\sum_{i=0}^{m}\sum_{j=0}^{n} N_{i,p}(u)N_{j,q}(v)w_{i,j}} \tag{4.22}$$

where p and q are the polynomial degrees, $N_{i,p}$ and $N_{j,q}$ are the B-Spline basis functions,

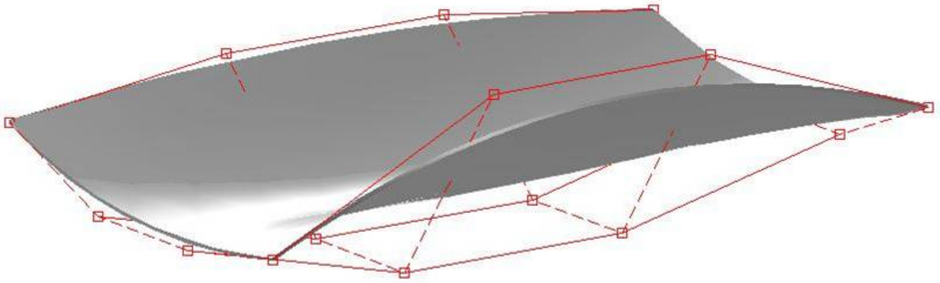

Figure 4.3: NURBS representation for panel's reference surface.

$\mathbf{P}_{i,j}$ (or $\mathbf{P}_i$) are control points; the weights $w_{i,j}$ of $\mathbf{P}_{i,j}$ (or w_i of $\mathbf{P}_i$) are the last coordinate of homogeneous point $\mathbf{P}^w_{i,j}$ (or $\mathbf{P}^w_i$)[1].

Now a brief introduction is given on how to move the control points of stiffeners' NURBS curves to change the shapes of the stiffeners' curves. In the conceptual and generalized sense, the control point (vector) of all stiffeners' NURBS curves can be moved from the initial position $\mathbf{x}_0$ in the direction $\mathbf{D}_\mathrm{C}$ a design step α to the current position $\mathbf{x}$ as follows:

$$\mathbf{x} = \mathbf{x}_0 + \mathbf{D}_\mathrm{C}\alpha \tag{4.23}$$

where

$$\mathbf{x} = \begin{bmatrix} \mathbf{x}^1 \\ \mathbf{x}^2 \\ \vdots \\ \mathbf{x}^{N_\mathrm{C}} \end{bmatrix}; \quad \mathbf{x}_0 = \begin{bmatrix} \mathbf{x}_0^1 \\ \mathbf{x}_0^2 \\ \vdots \\ \mathbf{x}_0^{N_\mathrm{C}} \end{bmatrix}; \quad \alpha = \begin{bmatrix} \alpha_1 \\ \alpha_2 \\ \vdots \\ \alpha_{N_\mathrm{DV}} \end{bmatrix} \tag{4.24}$$

and

$$\mathbf{D}_\mathrm{c} = \begin{bmatrix} \mathbf{d}_1^1 & \mathbf{d}_2^1 & \cdots & \mathbf{d}_{N_\mathrm{DV}}^1 \\ \mathbf{d}_1^2 & \mathbf{d}_2^2 & \cdots & \mathbf{d}_{N_\mathrm{DV}}^2 \\ \vdots & \vdots & \ddots & \vdots \\ \mathbf{d}_1^{N_\mathrm{C}} & \mathbf{d}_2^{N_\mathrm{C}} & \cdots & \mathbf{d}_{N_\mathrm{DV}}^{N_\mathrm{C}} \end{bmatrix} \tag{4.25}$$

Here N_C is the total number of control points for all stiffeners' NURBS curves, and N_DV is the total number of independent design variables or parameters.

---

[1] There are two different conventions for representing the control points in terms of their 4D coordinates (x, y, z, w):
Homogeneous, in which the coordinates represent the point's position in 4D space. Thus the point's 3D position is $(x/w, y/w, z/w)$.
Weighted Euclidean, in which the coordinates are already considered to have been divided through. Thus the first three components (x, y, z) directly represent the point's position in 3D space and the fourth w represents its weight.

4.3.4 Finite Element Meshing and Mapping

In a reference plane, the mesh for a stiffener is first generated in a separate routine that creates stiffeners' NURBS representations (Fig. 4.4a-b), and then the mesh for the plate is generated using an automatic mesh generation algorithm by adapting a *DistMesh*, a triangulation algorithm, developed by Persson and Strang (2004), with pre-generated stiffeners' mesh points fixed during the plate meshing (Fig. 4.4b). The planar reference mesh for the stiffened panel is mapped into a curved NURBS surface by using bilinear interpolation (Fig. 4.4c).

The current scheme allows the stiffeners to penetrate each other, which makes the meshing scheme simpler though it changes local load paths. As seen in Fig. 4.4, cut-outs are allowed using DistMesh. After meshing, the MSC.NASTRAN/MATLAB interface is used to automatically generate a NASTRAN input file for the stiffened panel optimization.

4.4 Numerical Studies on Optimal Blade Stiffened Panel Designs

EBF3paneloptimization has been used for numerous examples of stiffened panel optimization to confirm the important effects of the stiffeners' orientation, spacing, location, and curvature, etc., on the final/optimal design of a stiffened panel. The effects of intersection of stiffeners are not specially considered but they are included in the curvature effects. Two types of NASTRAN elements, CBAR and CQUAD4, are used to model blade stiffeners; however, CQUAD4 elements are used in all examples in which we consider the offset and the local buckling of a stiffener.

Both buckling and stress constraints (along with *side constraints* on design variables) are considered during the optimization, but only the buckling constraint is active in almost all

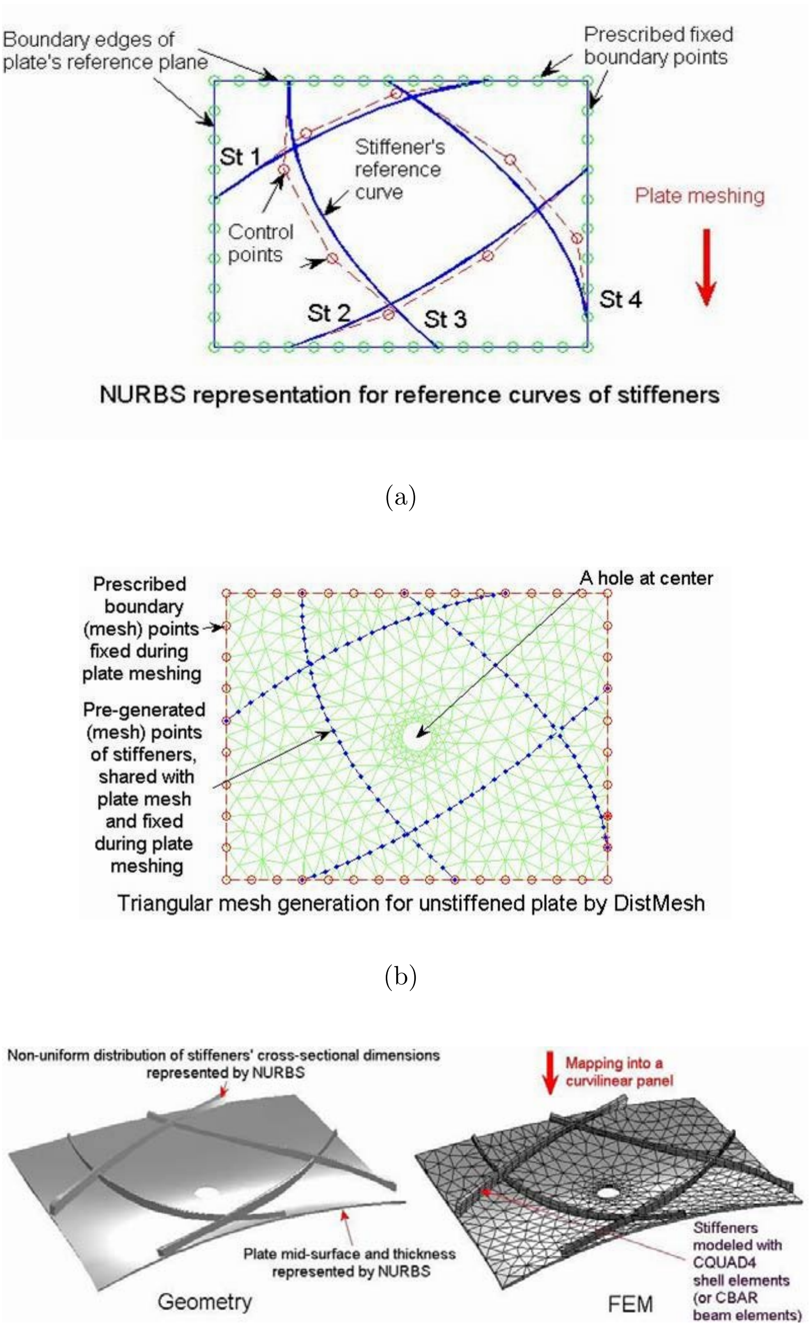

(a)

(b)

(c)

Figure 4.4: The meshing and mapping of a stiffened panel with a central hole.

cases for the uniformly distributed low level loads. Therefore, only buckling load and modes in final designs are shown in those cases. The default modified method of feasible directions (VR&D, 1999; MSC.Software, 2004; MSC.Software, 2005) is used unless it is mentioned otherwise. Optimization parameters are preset and not optimized. While addressing the relationship between the mass of an optimal design and the influencing factors, we only show relevant results. The final designs are only shown in the form of geometry and/or FEM 3D display, and design histories are selectively given when a special mention is desired. In many cases, the convergence is very difficult to achieve without using a special scaling technique to make design sensitivities comparable, and a maximum number of iterations (50 or 100) is usually met. Both the thickness of the unstiffened plate and the cross-sectional sizes of stiffeners are taken as design variables, but uniform cross-section of a stiffener is assumed unless mentioned otherwise. The offset of a stiffener is considered, and all the in-plane loads are added along the mid-surface of the unstiffened plate. Note that in this study all design points in the design space of placement design variables are results of sizing optimizations.

4.4.1 Orientation Effects

Panels that have a grid of stiffeners with a prescribed uniform or non-uniform pattern, such as *isogrid* or *geodesically* stiffened panels, are low-cost high-performance structures. Therefore, we first investigate the stiffeners' orientation effects on the optimal design of a stiffened panel by using two stiffeners under pure shear. The geometry, load, boundary conditions, material, and initial and bound values of designable sizes are shown in Fig. 4.5. To exclude the influence of other factors on the results, only two orientations of straight stiffeners are considered for brevity. In orientation I, the stiffeners' mid-curves are along the tensile direction of the stress field of the plate. The final design and the corresponding first four buckling modes are given in Fig. 4.6. It can be seen that the two stiffeners do not give good support for the plate to resist the buckling deformation and four buckling load factors

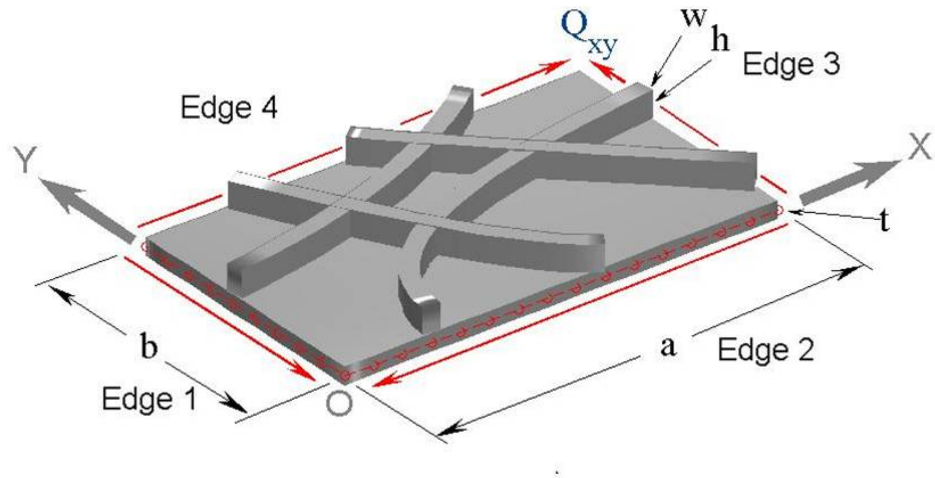

Figure 4.5: Geometrical dimensions ($a = 2.54$m; $b = 2.54$m), pure shear loading ($Q_{\mathrm{xy}} = 250$kN/m), and simply supported conditions of a blade stiffened panel. Both stiffeners and plate are made out of aluminum. Initial size and bounds: $t_0 = w_0 = 0.005$m; $h_0 = 5w_0$; $t_{\mathrm{b}} = w_{\mathrm{b}} = [0.0001, 0.1]$m; $h_{\mathrm{b}} = [0.0001, 0.5]$m.

are relatively far apart.

In orientation II, the stiffeners' mid-curves are in the compression direction of the stress field of the plate. The corresponding results are shown in Fig. 4.7. It can be clearly seen that the two stiffeners successfully support the plate and limit the buckling shapes within the smaller panes. The first few lower buckling modes are more clustered together with closer buckling loads. It implies that an optimal orientation is probably achieved there.

The panel mass decreases from 224kg in the case of orientation I (Fig. 4.6) to 144kg in the case of orientation II (Fig. 4.7). It is concluded that the orientation of a stiffener is an important factor influencing the optimal design.

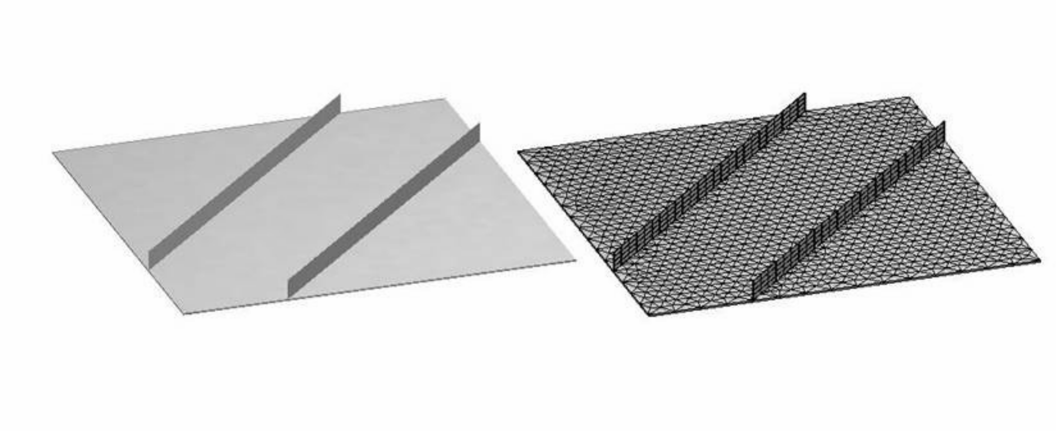

(a) Optimal design: $M_{\min} = 224$kg.

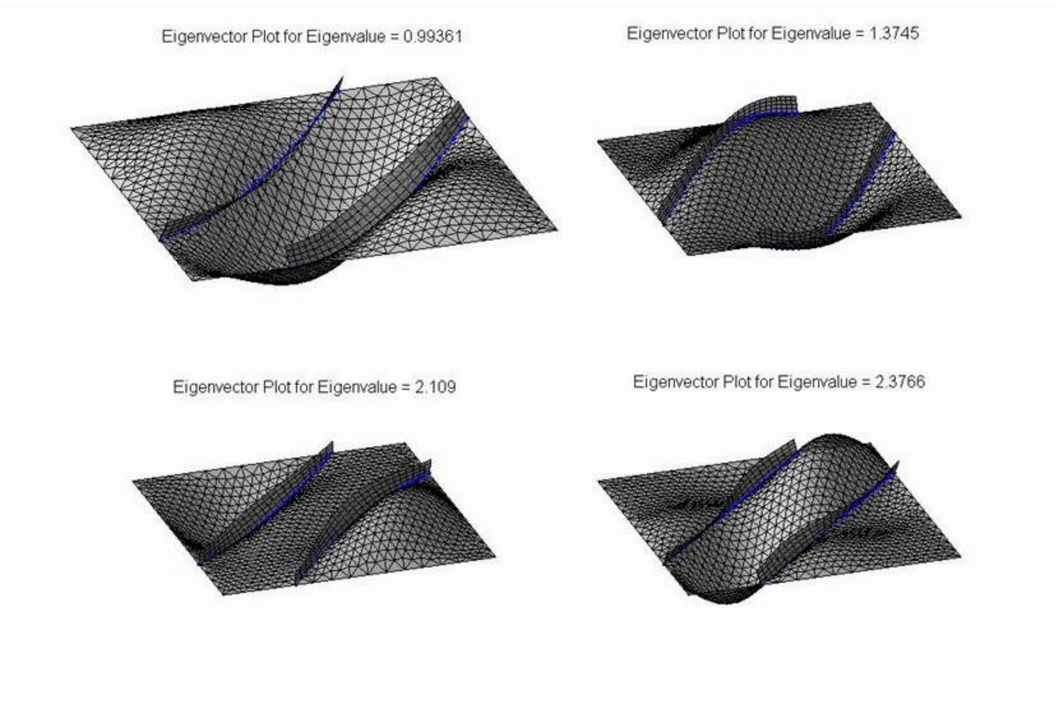

(b) First four buckling modes.

Figure 4.6: Effects of orientations of the stiffeners on the optimal designs. Orientation I: $M_{\min} = 224$kg.

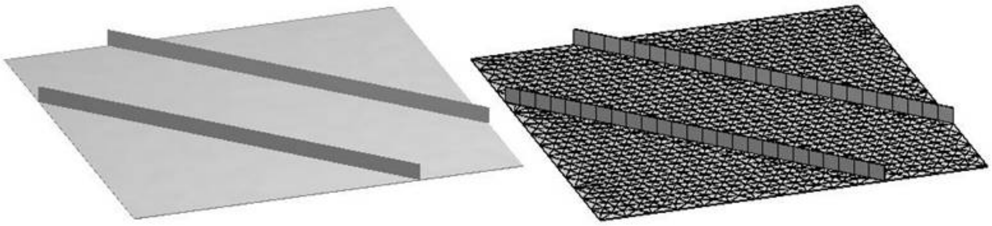

(a) Optimal design: $M_{\min} = 144$kg.

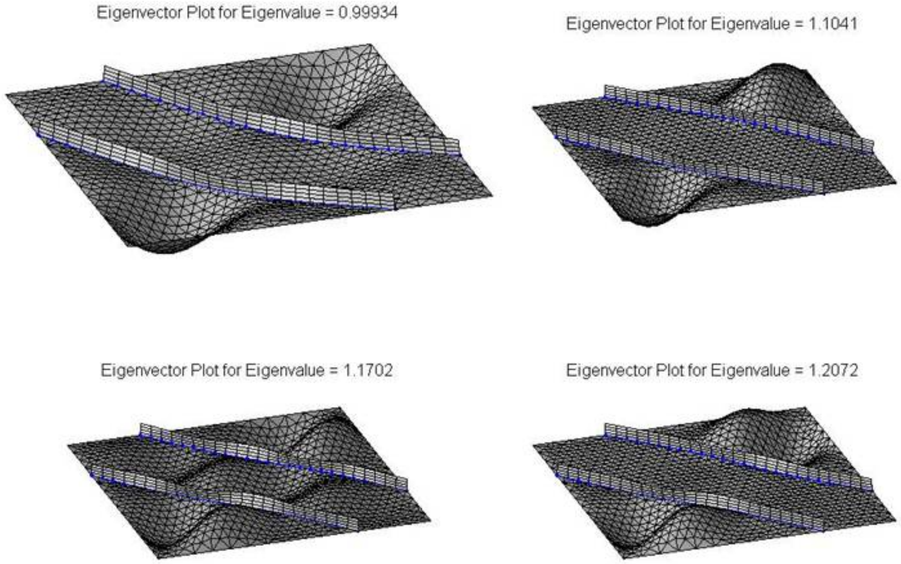

(b) First four buckling modes.

Figure 4.7: Effects of orientations of the stiffeners on the optimal designs. Orientation II: $M_{\min} = 144$kg.

4.4.2 Spacing Effects

The same data are given in Fig. 4.5 to study spacing effects. In fact, we first re-run the case of orientation II under the previous topic of "Orientation Effects", but using a less dense mesh for stiffeners, and obtain almost identical final design, as seen in Fig. 4.7 (Orientation I) and Fig. 4.8 (Spacing I). Then, we evenly place more stiffeners (with same less dense mesh for stiffeners) along the same orientation, and reduce the spacing of stiffeners by half. We observe a significant reduction of mass from 144kg for spacing I to 101kg for spacing II, and smaller (local) buckling dimples are obtained through the reduction of the spacing. Therefore, the spacing of stiffeners is another important factor influencing the optimal design. Too large a spacing reduces a stiffened panel to act like an unstiffened panel, and too small a spacing reduces it to act like an equivalent unstiffened plate with an increased thickness.

4.4.3 Location Effects

It is well known that placing stiffeners at wrong locations does not help support the plate; it will only increase the total mass of the panel. To illustrate this, we copy the results of Fig. 4.8 (Spacing I) into Fig. 4.9 (Location I), and locate the two stiffeners further apart as shown in Fig. 4.9 (Location II). We observe a large increase in mass from the original 144kg to 186kg and two smaller buckling dimples appear between the two stiffeners and form a larger local buckling dimple.

4.4.4 Curvature Effects

After we have studied the effects of orientation, spacing, and location placement of straight stiffeners on the optimal designs of stiffened panels, we further proceed to investigate the effects of the curvature of stiffeners on the optimal designs of panels. We can represent a

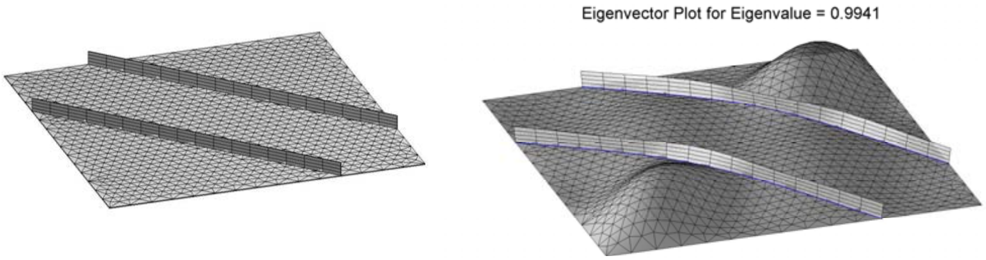

(a) Spacing I: Optimal design, $M_{\min} = 144$kg.

(b) Spacing I: First buckling mode.

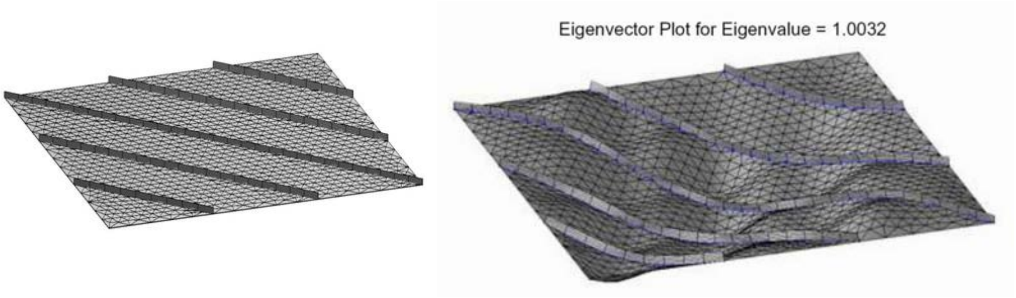

(c) Spacing II: Optimal design, $M_{\min} = 101$kg.

(d) Spacing II: First buckling mode.

Figure 4.8: Effects of spacing of the stiffeners on the optimal designs. Spacing II: $M_{\min} = 101$kg.

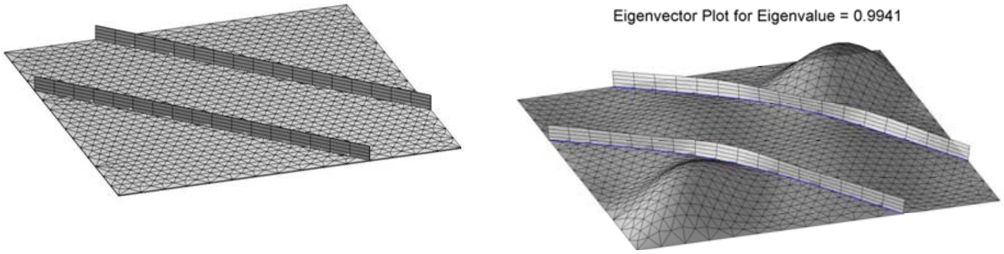

(a) Location I: Optimal design, $M_{\min} = 144$kg.

(b) Location I: First buckling mode.

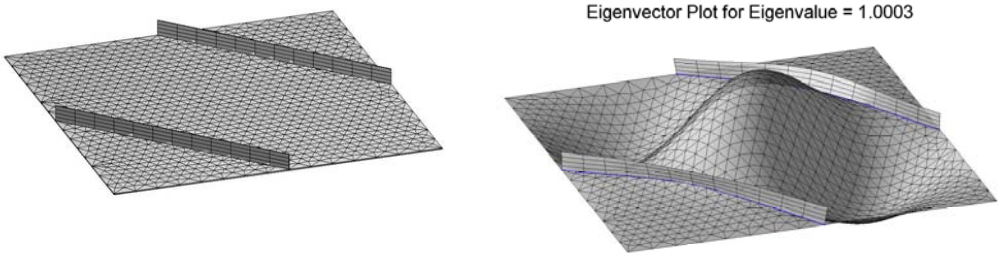

(c) Location II: Optimal design, $M_{\min} = 186$kg.

(d) Location II: First buckling mode.

Figure 4.9: Effects of location of the stiffeners on the optimal designs. Location I: $M_{\min} = 144$kg; Location II: $M_{\min} = 186$kg.

curved stiffener as an infinite number of inter-connected and intersected infinitesimal straight stiffeners.

Pure shearing

We first investigate the curvature effect on the final design of a stiffened panel under pure shear. Refer to Fig. 4.5 for planar dimensions, load and boundary conditions, etc. The two stiffeners are initially straight. Considering the symmetry, we use one design parameter α to control the motions of the mid-control points of both stiffeners' NURBS curves. Refer to Fig. 4.10 and Eq. (4.23)–Eq. (4.26) for initial control points and moving directions.

$$\mathbf{x}_0^1 = \begin{bmatrix} \frac{5.5}{15} \\ \frac{9.5}{15} \end{bmatrix}; \quad \mathbf{x}_0^2 = \begin{bmatrix} \frac{9.5}{15} \\ \frac{5.5}{15} \end{bmatrix}; \quad \mathbf{d}^1 = \mathbf{d}_1^1 = \begin{bmatrix} -\cos\frac{\pi}{4} \\ \sin\frac{\pi}{4} \end{bmatrix}; \quad \text{and} \quad \mathbf{d}^2 = \mathbf{d}_1^2 = \begin{bmatrix} \cos\frac{\pi}{4} \\ -\sin\frac{\pi}{4} \end{bmatrix} \tag{4.26}$$

Figures 4.11–4.13 shows the final designs and corresponding buckling modes for parameter α = -0.3, 0.0, and 0.8, respectively. It shows that though a bad placement of curvilinear stiffeners, refer, *e.g.* to Fig. 4.11 ($\alpha = -0.3$), may not reduce the mass compared to a placement of straight stiffeners, refer, *e.g.* to Fig. 4.12 ($\alpha = 0.0$), a good placement of curved stiffeners, refer, *e.g.* to Fig. 4.13 ($\alpha = 0.8$), may significantly reduce the mass. A diagram of minimum mass (M_{min}) vs. shape design parameter (α) is shown in Fig. 4.14. It can be seen that the global optimum is achieved around $\alpha = 0.8$, which corresponds to curvilinear placed stiffeners (Fig. 4.13), though a local minimum corresponds to straight stiffeners at $\alpha = 0.0$ (Fig. 4.12). It is evident that the curvature of a stiffener has a significant influence on the optimal design of a stiffened panel, though a curved stiffener is not always advantageous over a straight one. It also should be noticed that for placement optimization of stiffeners, one needs to consider multiple minima problems.

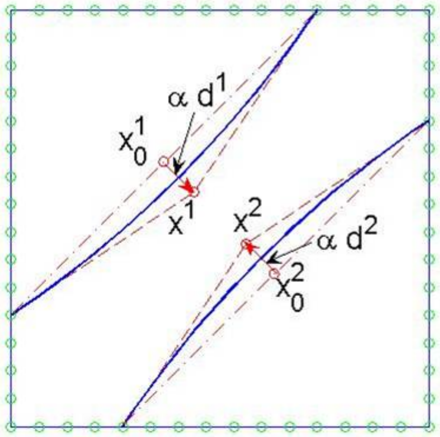

Figure 4.10: One design parameter α controls the motions of two mid control points $\mathbf{x^1}$ and $\mathbf{x^2}$ starting from $\mathbf{x_0^1}$ and $\mathbf{x_0^2}$ and by $\alpha\mathbf{d^1}$ and $\alpha\mathbf{d^2}$ for stiffeners 1 and 2, respectively.

Bi-normal loading - two stiffeners

We now investigate the curvature effect on the optimal design of a stiffened panel under a bi-normal loading. Fig. 4.15 gives planar dimensions, load and boundary conditions, etc. The two stiffeners are initially straight and located very close to the upper/lower boundary edges of the panel (location I). Considering the symmetry, we use one design parameter to control the motions of two mid control points of both stiffeners' NURBS curves, as shown in Fig. 4.16 and given by Eq. (4.27).

Figure 4.17 shows the optimal design and first buckling mode for each of the three placements of the two stiffeners. The first case shows that the pairs of stiffeners are badly placed initially, and they cannot effectively support the plate, therefore they almost vanish after optimization. However, from Fig. 4.18 it is seen that a minimum is approximately achieved when the design parameter $\alpha = 1.6$, where stiffeners jointly provide a better support

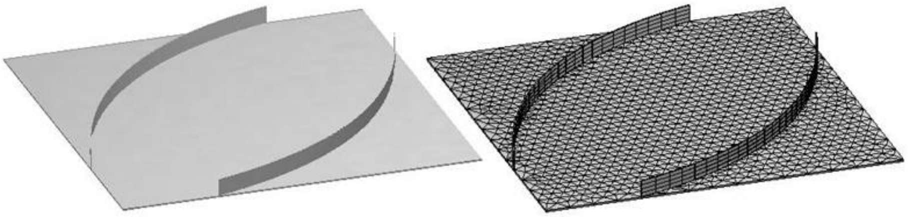

(a) Optimal design: $M_{\min} = 240\text{kg}$.

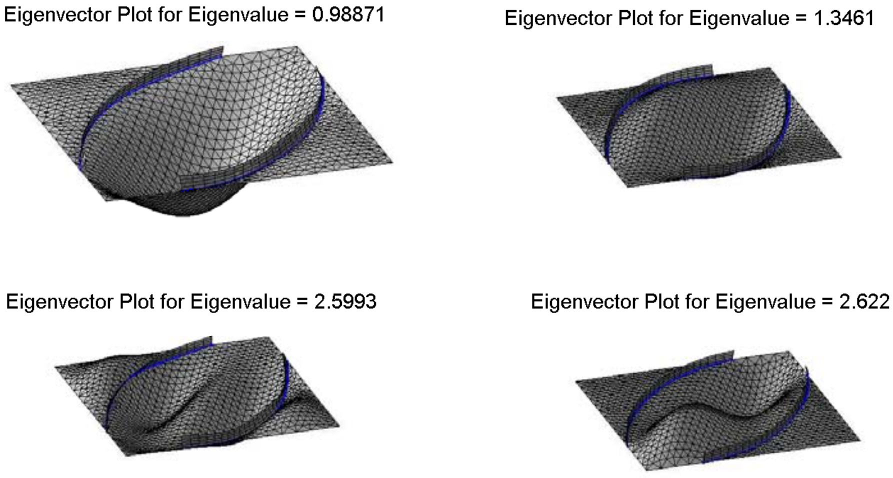

(b) First four buckling modes.

Figure 4.11: Effects of curvature of the stiffeners on the optimal designs. $\alpha = -0.3$: $M_{\min} = 240\text{kg}$.

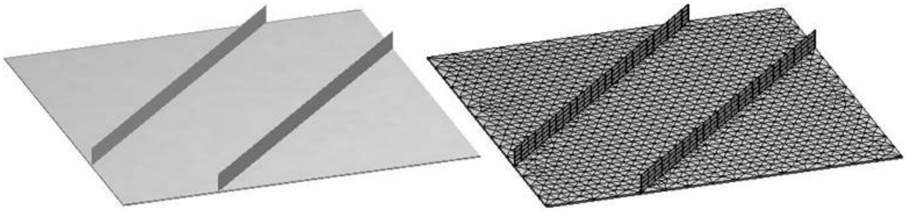

(a) Optimal design: $M_{\min} = 220\text{kg}$.

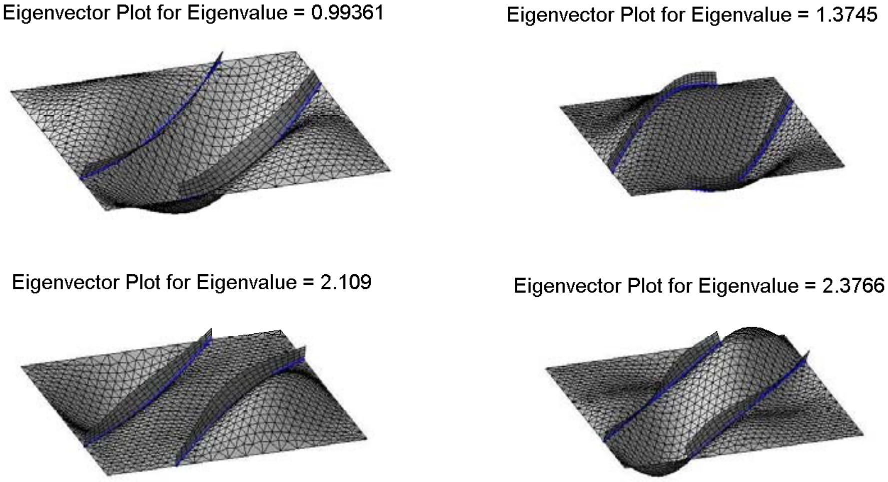

Eigenvector Plot for Eigenvalue = 0.99361

Eigenvector Plot for Eigenvalue = 1.3745

Eigenvector Plot for Eigenvalue = 2.109

Eigenvector Plot for Eigenvalue = 2.3766

(b) First four buckling modes.

Figure 4.12: Effects of curvature of the stiffeners on the optimal designs. $\alpha = 0.0$: $M_{\min} = 220\text{kg}$.

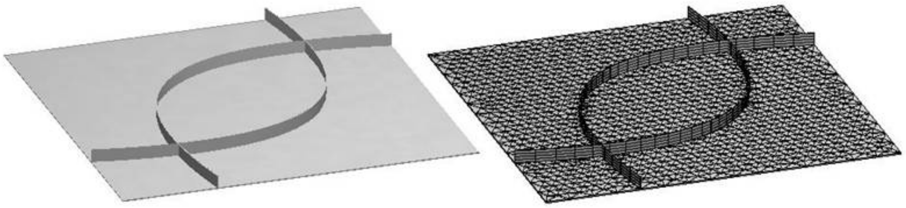

(a) Optimal design: $M_{\min} = 178$kg.

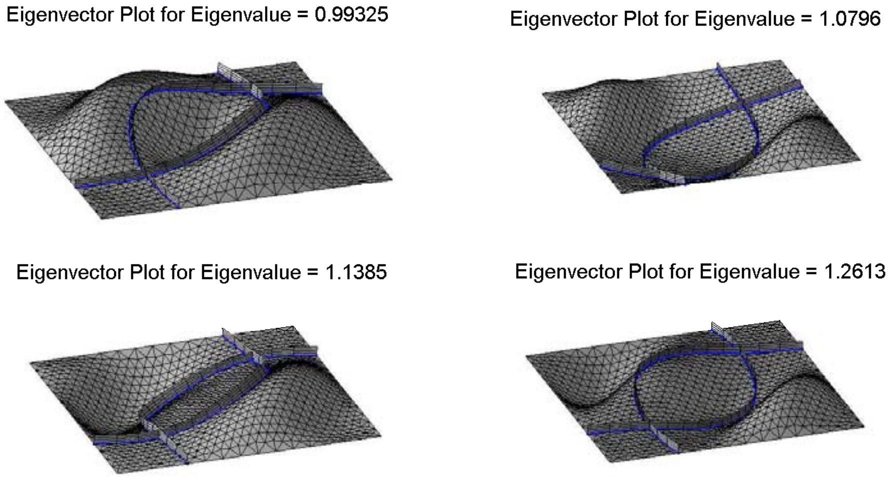

Eigenvector Plot for Eigenvalue = 0.99325

Eigenvector Plot for Eigenvalue = 1.0796

Eigenvector Plot for Eigenvalue = 1.1385

Eigenvector Plot for Eigenvalue = 1.2613

(b) First four buckling modes.

Figure 4.13: Effects of curvature of the stiffeners on the optimal designs. $\alpha = 0.8$: $M_{\min} = 178$kg.

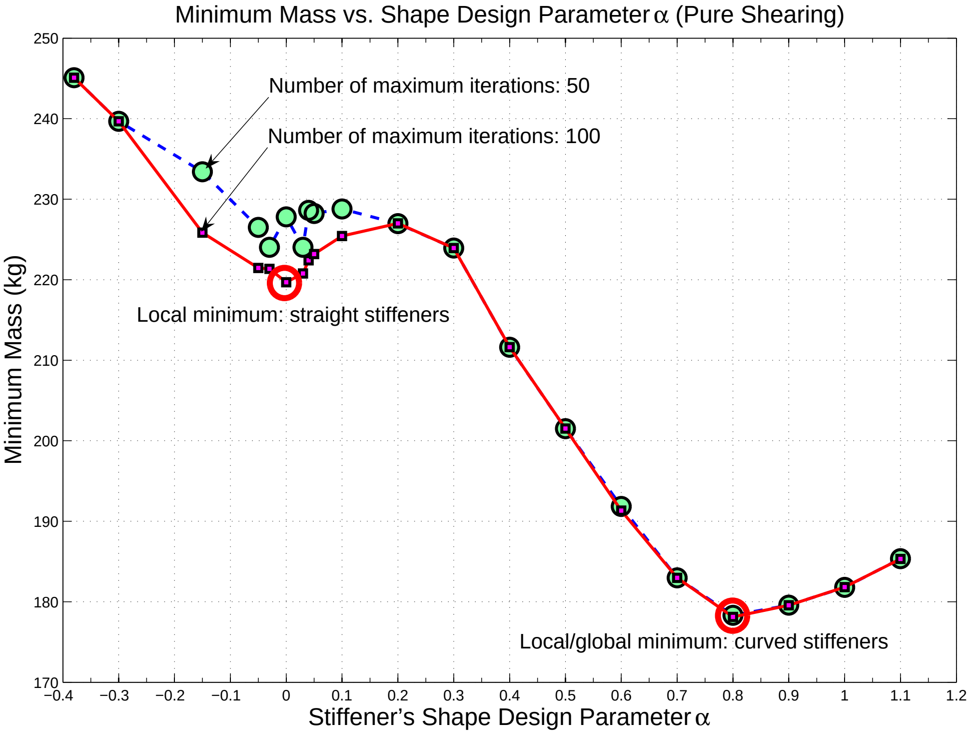

Figure 4.14: Diagram of minimum mass vs. shape design parameter α. Two minima are found. One corresponds to straight stiffeners at about $\alpha = 0.0$ with minimum mass $M_{\text{min}} = 220$kg. The global optimal shape corresponds to curvilinear stiffeners at about $\alpha = 0.8$ with a minimum mass $M_{\text{min}} = 178$kg, which is the minimum of the two minima.

and form a smaller buckling shape in the domain between the two stiffeners.

$$\mathbf{x}_0^1 = \begin{bmatrix} \frac{7.5}{15} \\ \frac{1}{15} \end{bmatrix}; \quad \mathbf{x}_0^2 = \begin{bmatrix} \frac{7.5}{15} \\ \frac{14}{15} \end{bmatrix}; \quad \mathbf{d}^1 = \mathbf{d}_1^1 = \begin{bmatrix} \cos\frac{\pi}{2} \\ \sin\frac{\pi}{2} \end{bmatrix}; \quad \text{and} \quad \mathbf{d}^2 = \mathbf{d}_1^2 = \begin{bmatrix} \cos\frac{\pi}{2} \\ -\sin\frac{\pi}{2} \end{bmatrix} \tag{4.27}$$

Now, let the two initially straight stiffeners move close to each other as shown in Fig. 4.19 (location II). We then make a similar thorough line search to obtain the diagram of minimum mass vs. shape design parameter α, as shown in Fig. 4.20. We again observe three local minima for the curvilinear placement of stiffeners. The global minimum is found at $\alpha = 0.10$ with a minimum mass $M_{\text{min}} = 197$kg, which is the minimum of all three minima (compared

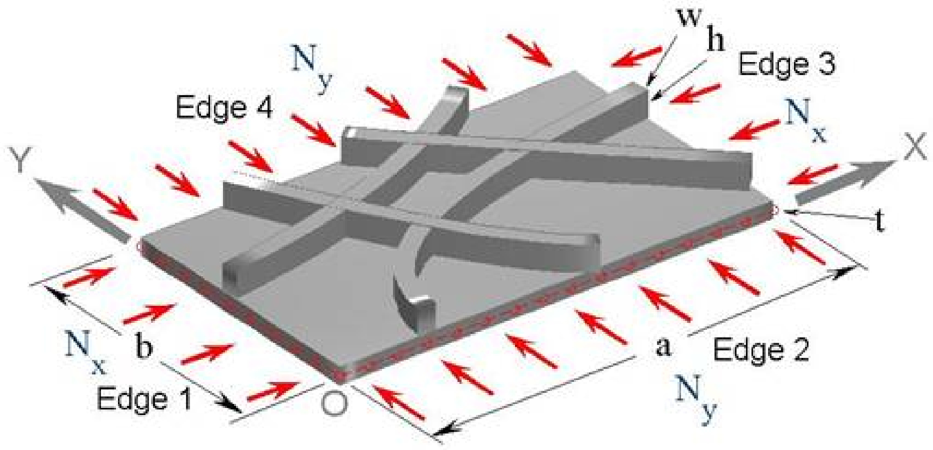

Figure 4.15: Geometrical dimensions ($a = 2.54\text{m}$; $b = 2.54\text{m}$), bi-normal loading ($N_\text{x} = 250\text{kN/m}; N_\text{y} = 0.2N_\text{x}$), and simply-supported conditions of a blade stiffened panel. Both stiffeners and plate are made out of aluminum. Initial size and bounds: $t_0 = w_0 = 0.005\text{m}$; $h_0 = 5w_0$; $t_\text{b} = w_\text{b} = [0.0001, 0.1]\text{m}$; $h_\text{b} = [0.0001, 0.5]\text{m}$.

with straight stiffeners at $\alpha = 0.0$ with $M_\text{min} = 205\text{kg}$).

For location III, let the two initially straight stiffeners move closer to each other so that the two stiffeners are evenly placed as shown in Fig. 4.21. Now, we make a similar thorough line search to obtain the diagram of minimum mass vs. shape design parameter α, as shown in Fig. 4.22. We again observe three local minima for the generally curvilinear placement of stiffeners. The global minimum is found to be straight stiffeners at $\alpha = 0.0$ with a minimum mass $M_\text{min} = 185\text{kg}$, which is the minimum of all three minima.

In this series of examples, we see that for fixed ends of stiffeners, curved stiffeners may better support the plate than straight stiffeners. That straight stiffeners sometimes are better is only a special case, just like a straight line is a special case of curves.

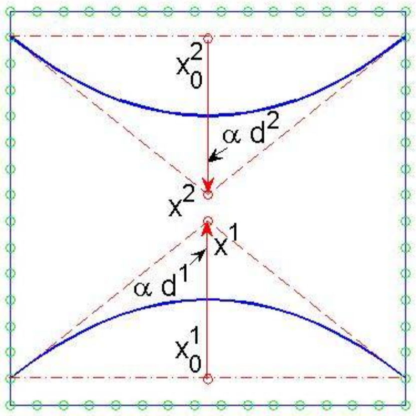

Figure 4.16: Location 1: The end points of the two stiffeners are close to the upper/lower edges of the panel and 13/15b apart from each other. One design parameter α controls the motions of two mid control points $\mathbf{x^1}$ and $\mathbf{x^2}$ starting from $\mathbf{x_0^1}$ and $\mathbf{x_0^2}$ and by $\alpha_1\mathbf{d^1}$ and $\alpha_2\mathbf{d^2}$ for stiffeners 1 and 2, respectively.

Bi-normal loading - four stiffeners: convergence study

Refer to Fig. 4.15 for planar dimensions, load (except that $N_\mathrm{y} = N_\mathrm{x}$) and boundary conditions, etc., with four initially straight and evenly placed stiffeners as shown in Fig. 4.23. Considering the symmetry, we use one design parameter to control the motions of the mid control points of the four stiffeners' NURBS curves. We use the thorough line search to get two sets of results to show the benefit of using scaling of the design variable and the scaling and shifting for responses as techniques to overcome the convergence problem. Figure 4.24 shows a comparison of the diagrams of minimum mass vs. shape design parameter as well as the numbers of design iterations required to converge. It is observed that in much of the design space, the optima of sizing optimizations are close to each other before and after the improvement of the convergence. In some regions, however, the optima obtained are obviously different. Generally speaking, after the improvement of the convergence, the minimum mass is reduced and the number of the iterations is reduced by about 50%. Figure 4.25 shows the optimal shapes obtained before and after the improvement of the convergence.

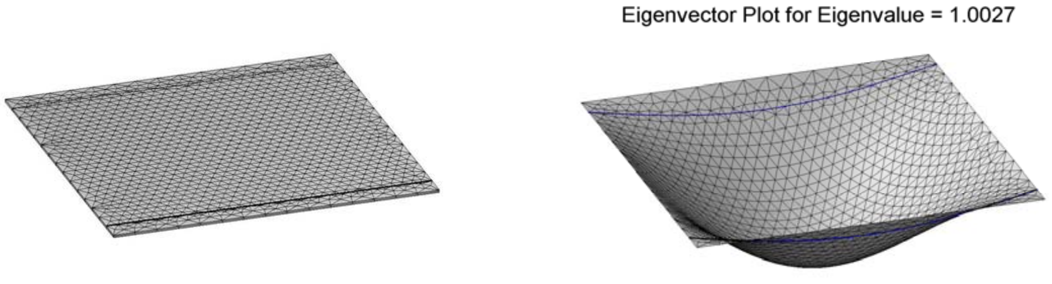

(a) $\alpha = 0.0$: Optimal design, $M_{\min} =$ 344kg.

(b) $\alpha = 0.0$: First buckling mode.

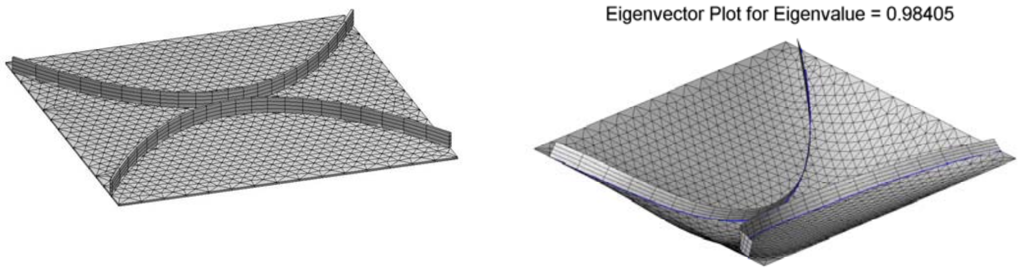

(c) $\alpha = 0.9$: Optimal design, $M_{\min} =$ 245kg.

(d) $\alpha = 0.9$: First buckling mode.

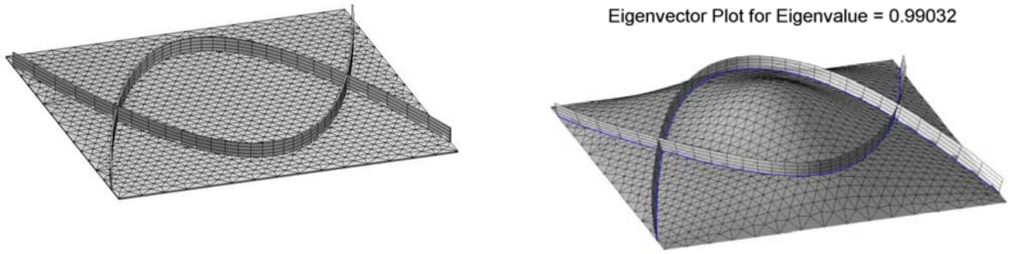

(e) $\alpha = 1.6$: Optimal design, $M_{\min} =$ 235kg.

(f) $\alpha = 1.6$: First buckling mode.

Figure 4.17: Location I: effects of curvature of the stiffeners on the optimal designs.

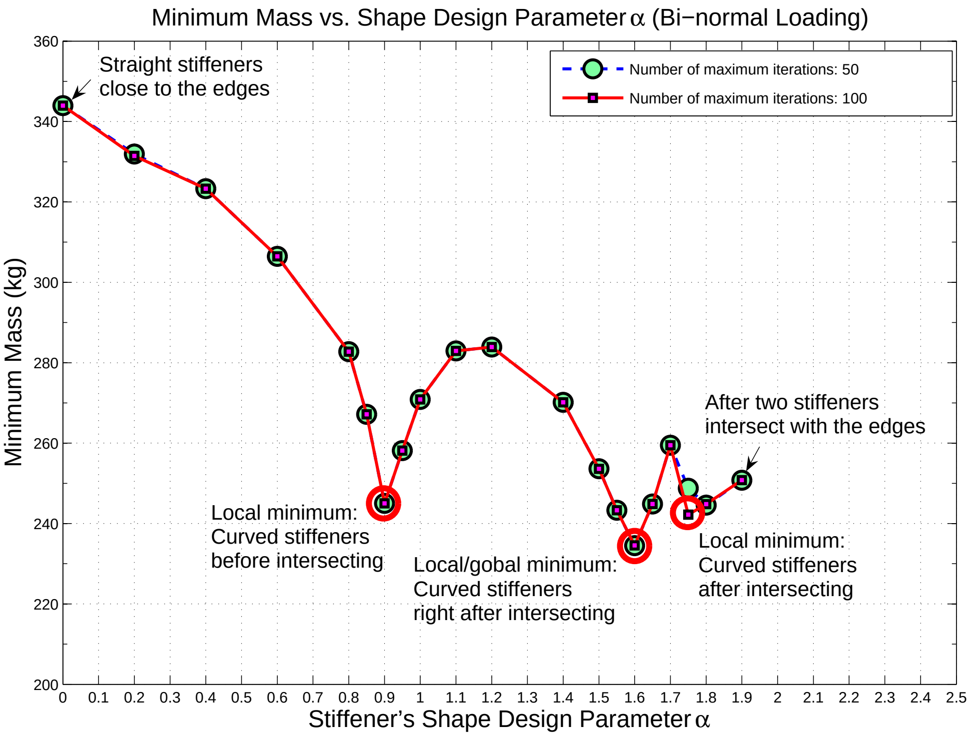

Figure 4.18: Location I: Diagram of minimum mass vs. shape design parameter α. The global optimal shape is achieved at about $\alpha = 1.60$ with a minimum mass $M_{\min} = 245$kg. The maximum number of iterations for size optimization is set to be 50 and 100.

Figure 4.26 shows the first four buckling modes of the optimal shapes obtained before and after the improvement of the convergence. Figure 4.27 show the comparison of the design histories for the optimal shapes before and after the improvement of the convergence.

Bi-normal loading - four stiffeners with a central hole

We have observed that in the case of uniform load and displacement boundary conditions and evenly placed stiffeners, traditional straight stiffeners sometimes give a better design than curved stiffeners. However, a disturbance to the uniformity of the boundary conditions or plate itself may change the above conclusion. For example, after an inclusion of a cutout

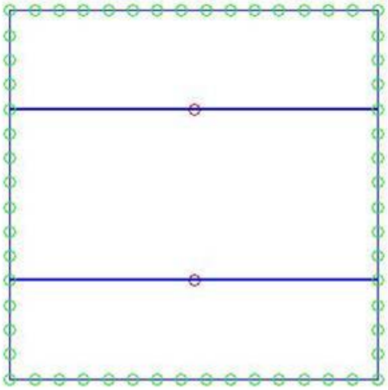

Figure 4.19: Location II: The end points of the two stiffeners are close to the upper/lower edges of the panel and 7/15b apart from each other. One design parameter α controls the motions of two mid control points $\mathbf{x^1}$ and $\mathbf{x^2}$ starting from $\mathbf{x_0^1}$ and $\mathbf{x_0^2}$ and by $\alpha_1\mathbf{d^1}$ and $\alpha_2\mathbf{d^2}$ for stiffeners 1 and 2, respectively. Also see Fig. 4.16.

in the plate, curved stiffeners may give a better design than the straight stiffeners.

We now investigate how an inclusion of a hole of radius 0.3m affects the optimal placement/shape design of stiffeners under a bi-normal loading. Refer to Fig. 4.15 for planar dimensions, load (except that $N_{\mathrm{y}} = 0.5N_{\mathrm{x}}$) and boundary conditions, etc., but with four initially straight and evenly placed stiffeners as shown in Fig. 4.28. Again, we use one design parameter α to control the motions of the mid control points of the four stiffeners' NURBS curves.

For comparison, we use the thorough line search to get the relationship between the minimum mass from sizing and the shape design parameter α for both the case without a hole and the case with a central hole (Fig. 4.29). For the case without a hole, we find the global minimum at $\alpha = 0.0$ with $M_{\mathrm{min}} = 190$kg, which corresponds to straight stiffeners. For the case with the central hole of radius 0.3m, however, we find the global minimum at $\alpha = 0.0725$ with $M_{\mathrm{min}} = 182$kg, which corresponds to curved stiffeners. Figures 4.30, 4.31 and 4.32 show the effect of a central hole of radius 0.3m on the optimal shape design of

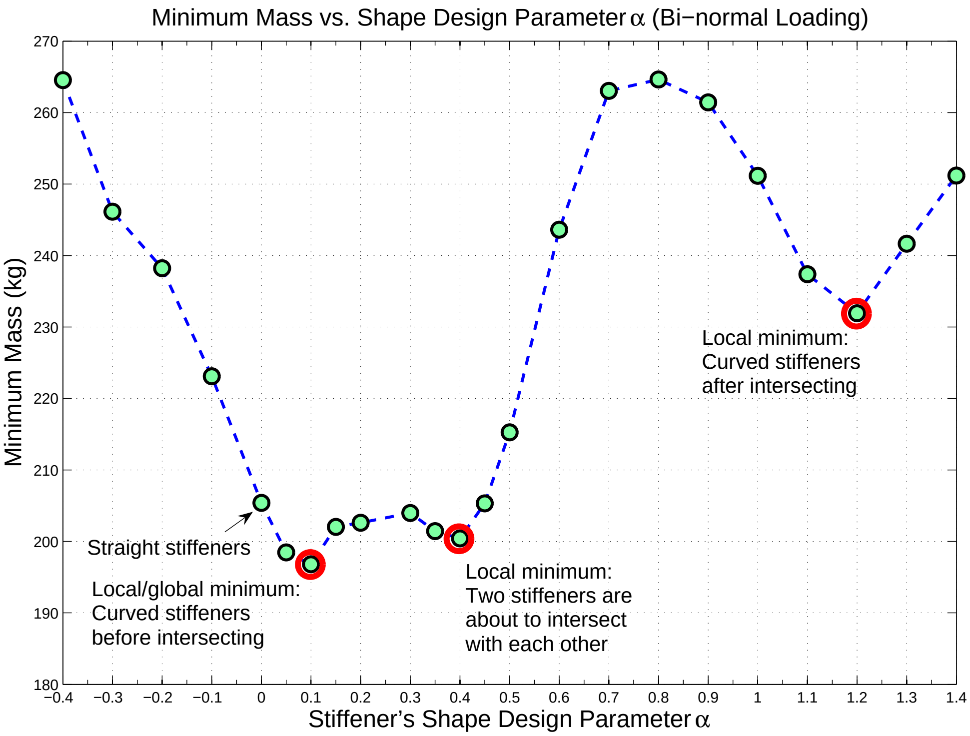

Figure 4.20: Location II: Diagram of minimum mass vs. shape design parameter α. The global optimal shape is achieved at about $\alpha = 0.10$ with a minimum mass $M_{\min} = 197$kg (compared with straight stiffeners $\alpha = 0.0$ with $M_{\min} = 205$kg). The maximum number of iterations for size optimization is set to be 100.

stiffeners.

It is observed that even though the loading is uniformly distributed, evenly placed straight stiffeners are not necessarily best designs.

Complex in-plane loading: bi-normal and shear loading

We finally use two shape design parameters to investigate the curvature effect on the final design of a stiffened panel under a complex in-plane load: bi-normal and shear loading. Refer to Fig. 4.33 for planar dimensions, load and boundary conditions, etc. Though the

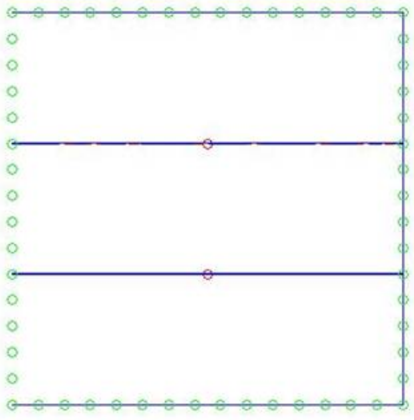

Figure 4.21: Location III: The end points of the two stiffeners are close to the upper/lower edges of the panel and $5/15b$ apart from each other. One design parameter α controls the motions of two mid control points $\mathbf{x^1}$ and $\mathbf{x^2}$ starting from $\mathbf{x_0^1}$ and $\mathbf{x_0^2}$ and by $\alpha_1\mathbf{d^1}$ and $\alpha_2\mathbf{d^2}$ for stiffeners 1 and 2, respectively. Also see Fig. 4.16.

loading is unsymmetrical, we retain a symmetric design with four initially straight stiffeners to simplify the conceptual study at hand. We use design parameter α_1 to control the shapes of mid-curves of the two stiffeners that are originally straight and evenly placed in the X - direction, and use design parameter α_2 to control the shapes of mid-curves of the two other stiffeners that are also originally straight and evenly placed in the Y-direction. Refer to Fig. 4.34 and Eqs. (4.28) and (4.29).

$$\mathbf{x}_0^1 = \begin{bmatrix} \frac{7.5}{15} \\ \frac{5}{15} \end{bmatrix}; \quad \mathbf{x}_0^2 = \begin{bmatrix} \frac{7.5}{15} \\ \frac{10}{15} \end{bmatrix}; \quad \mathbf{x}_0^3 = \begin{bmatrix} \frac{5}{15} \\ \frac{7.5}{15} \end{bmatrix}; \quad \text{and} \quad \mathbf{x}_0^4 = \begin{bmatrix} \frac{10}{15} \\ \frac{7.5}{15} \end{bmatrix} \tag{4.28}$$

$$\mathbf{d}_1^1 = \begin{bmatrix} \cos\frac{\pi}{2} \\ \sin\frac{\pi}{2} \end{bmatrix}; \quad \mathbf{d}_1^2 = \begin{bmatrix} \cos\frac{\pi}{2} \\ -\sin\frac{\pi}{2} \end{bmatrix}; \quad \mathbf{d}_2^3 = \begin{bmatrix} \cos 0 \\ \sin 0 \end{bmatrix}; \quad \text{and} \quad \mathbf{d}_2^4 = \begin{bmatrix} \cos\pi \\ \sin\pi \end{bmatrix} \tag{4.29}$$

As we are not performing an automatic placement optimization at this time, the two-parameters problem can be handled manually by dividing the interested square domain space by 11 × 11 grid points in the design space as shown in Fig. 4.35. We start from

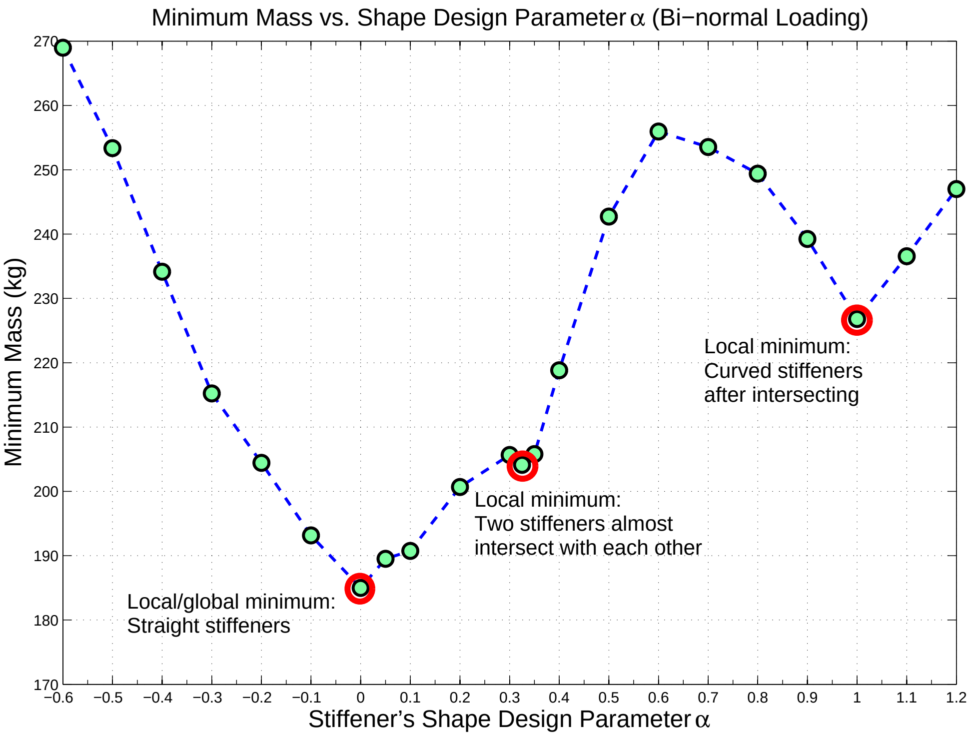

Figure 4.22: Location 3: Diagram of minimum mass vs. shape design parameter α. The global optimal shape is achieved at about $\alpha = 0.0$ with a minimum mass $M_{\text{min}} = 185$kg. The maximum number of iterations for size optimization is set to be 100.

the placement of straight stiffeners, *i.e.*, $\alpha_1 = \alpha_2 = 0$, as it is conventionally viewed as a potentially optimal placement for uniformly distributed loadings along the edges. We then vary the design point in the neighborhood and see if there is any reduction in the total mass. It happens that the initially straight stiffeners are a local optimal design (the dark square point inside the circle nearby the left-bottom corner in Fig. 4.35).

By intuition, we start from another design point, which represents a curvilinear placement of the stiffeners. By searching around using the "gradient" information of mass reduction or increase, we locate another local minimum design, *i.e.*, around $\alpha_1 = 0.7$ and $\alpha_2 = 1.3$ (the dark square point inside the circle near the right-top corner in Fig. 4.35). Figure 4.36 shows

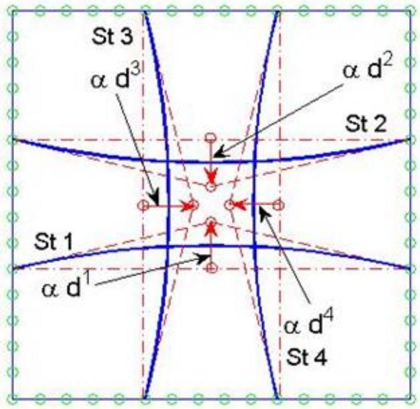

Figure 4.23: One design parameter α controls the shapes of the NURBS curves of four stiffeners, which are initially straight ($\alpha = 0.0$) and evenly spaced.

the final designs of the two local minima for the two-parameters case. Although both are local minima, the curvilinear placement of the stiffeners has a lower mass ($M_{\min} = 179$kg) than the straight one ($M_{\min} = 187$kg). Figure 4.37 show the first four buckling modes of the two minima, respectively.

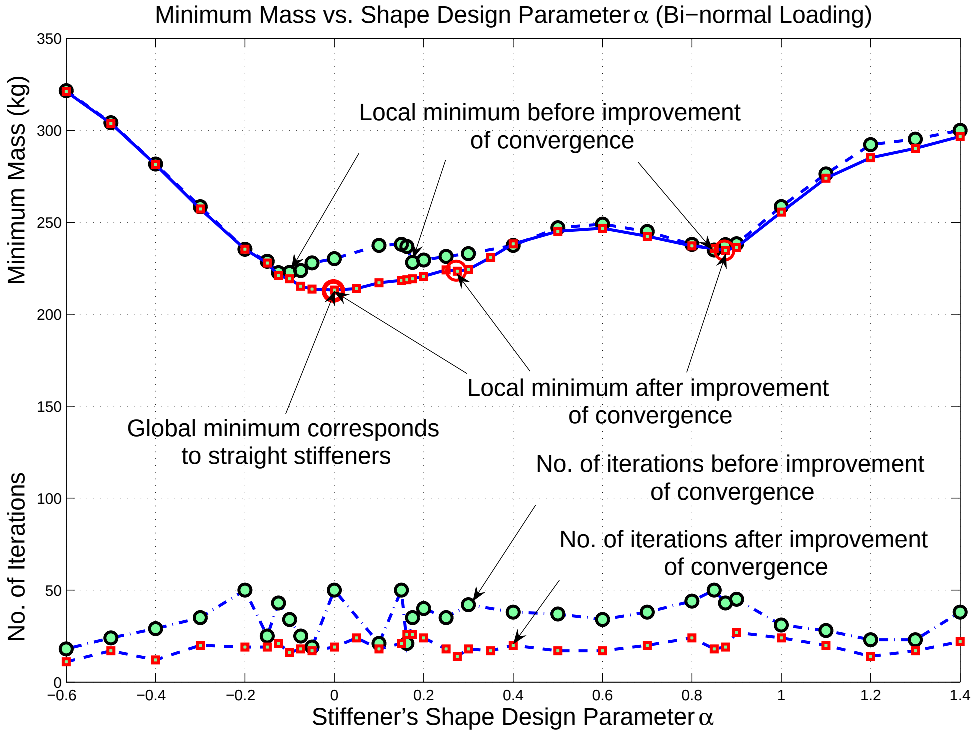

Figure 4.24: A comparison of diagrams of minimum mass vs. shape design parameter α before and after the improvement of the convergence. After the improvement of the convergence, three local minima are found. One corresponds to straight stiffeners at about $\alpha = 0.0$ with a minimum mass $M_{\text{min}} = 213\text{kg}$ which is also the global minimum. The other two local minima correspond to curvilinear stiffeners at about $\alpha = 0.275$ with a minimum mass $M_{\text{min}} = 223\text{kg}$, and at about $\alpha = 0.875$ with a minimum mass $M_{\text{min}} = 235\text{kg}$.

4.5 Conclusions and Future Work

This chapter presents many numerical results from a study on unitized panels with straight and curvilinear stiffeners. An integrated approach to achieve optimal design of stiffened panels under various practical requirements is adopted in the MATLAB environment. The codes with several capabilities, such as NURBS (for geometric model), DistMesh (for mesh generation), 3D display (for visualization of the stiffened panel), and MSC.NASTRAN, are used as subroutines or subprograms.

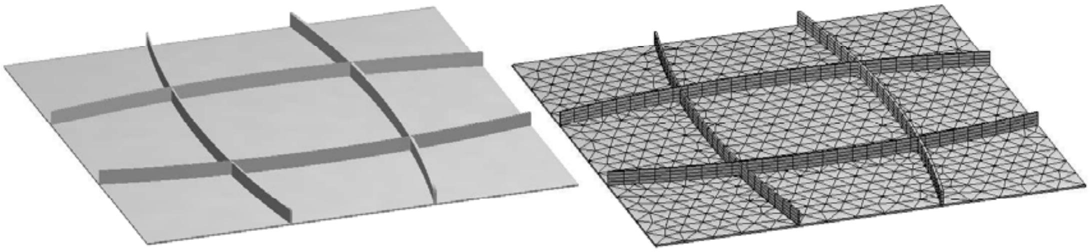

(a) Before the improvement of the convergence – global minimum: $\alpha = -0.1$; $M_{\min} = 233$kg; optimal shape: curved stiffeners.

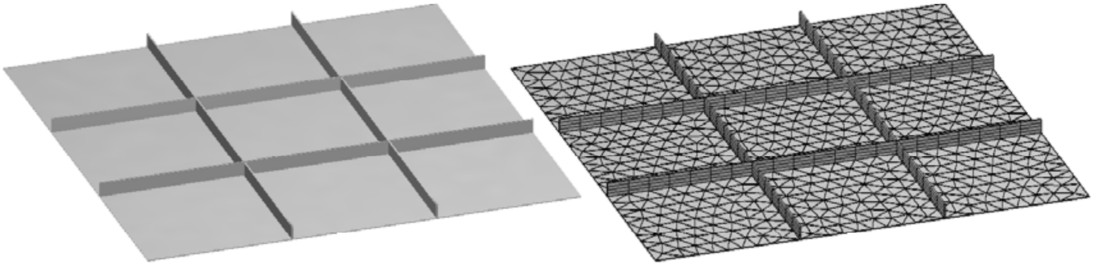

(b) After the improvement of the convergence – global minimum: $\alpha = 0.0$; $M_{\min} = 213$kg; optimal shape: curved stiffeners.

Figure 4.25: A comparison of optimal designs before and after the improvement of the convergence.

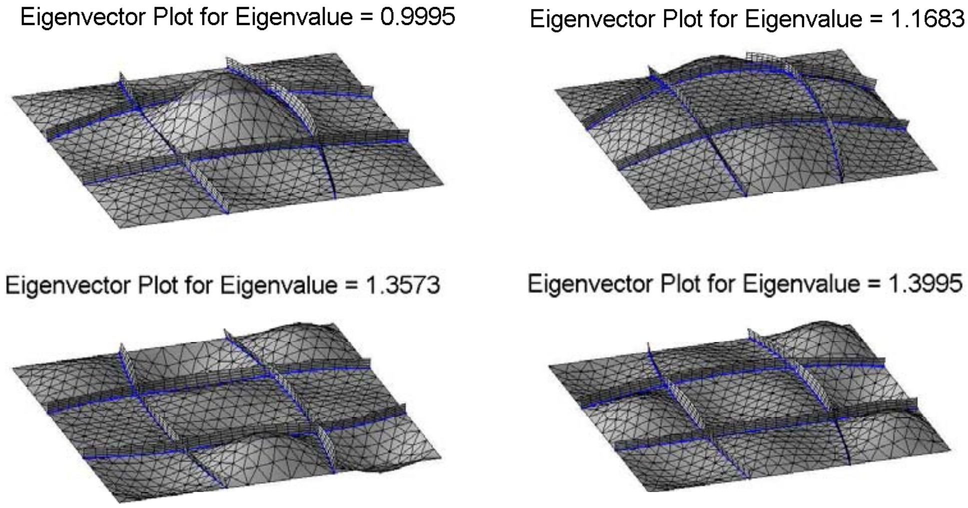

(a) Before the improvement of the convergence.

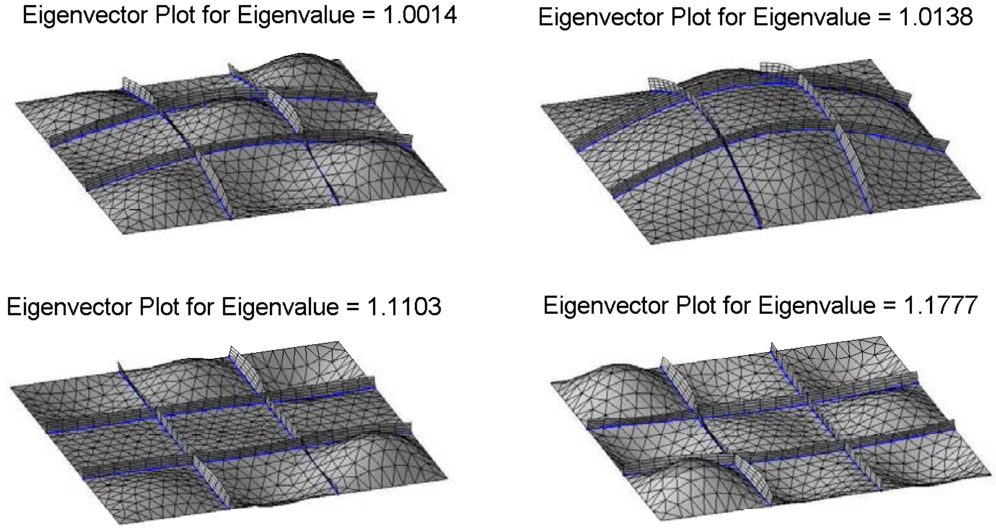

(b) After the improvement of the convergence.

Figure 4.26: A comparison of the first four buckling modes before and after the improvement of the convergence.

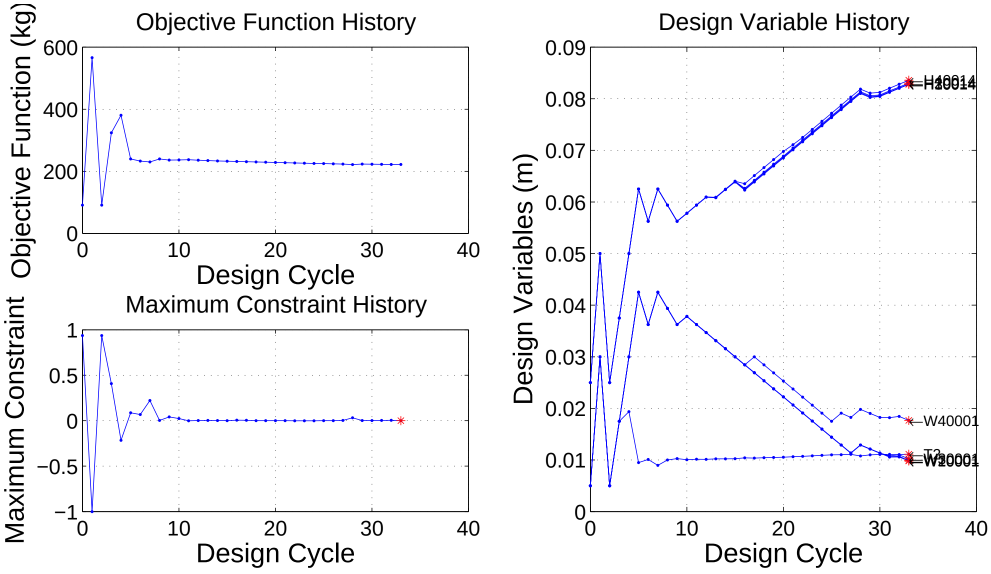

(a) Before the improvement of the convergence.

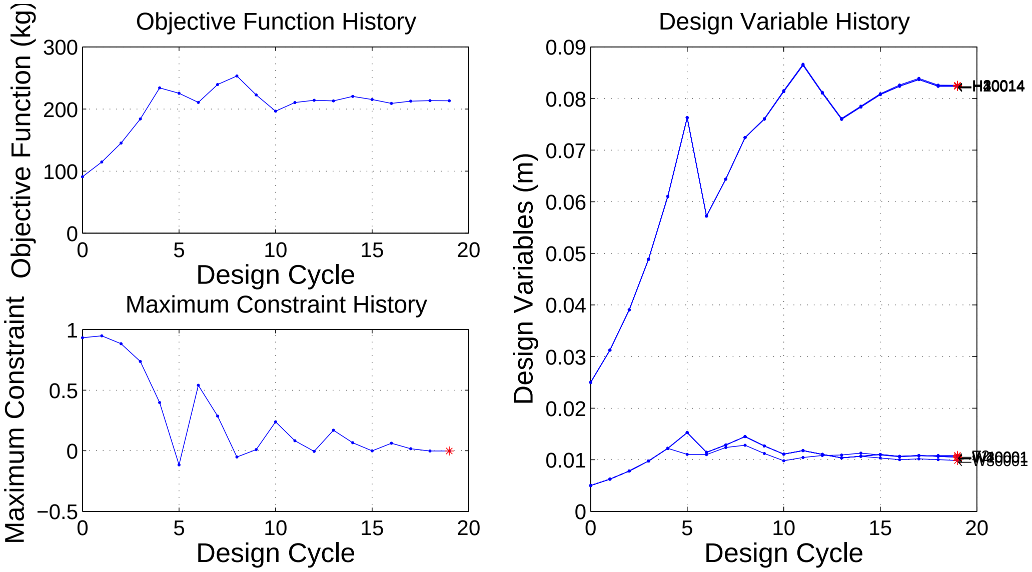

(b) After the improvement of the convergence.

Figure 4.27: A comparison of the design histories before and after the improvement of the convergence.

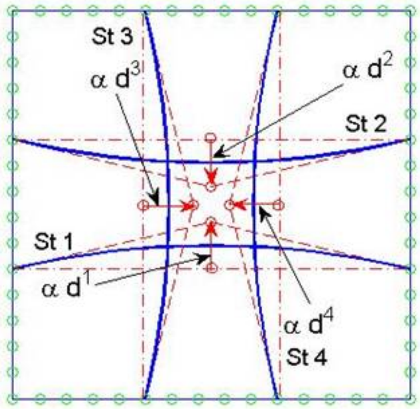

Figure 4.28: One design parameter α controls the shapes of the NURBS curves of four stiffeners, which are initially straight ($\alpha = 0.0$) and evenly spaced.

Numerical studies on optimal stiffened panel designs are made to investigate the effects of certain factors, such as orientation, spacing, location, and curvature, on the optimal designs.

We observe that a curvilinear placement of stiffeners sometimes gives a better design than straight stiffeners. A curvilinear placement of stiffeners is equivalent to an orientation, spacing, location, and intersection placement of infinitesimal straight stiffeners. It also plays a role in topology optimization due to the change of stiffeners' intersections.

Therefore, it is necessary to perform an automatic placement optimization of generally curvilinear stiffened panels and use global optimization techniques to find the best design among multiple local optima, which are common for optimal designs of stiffened panels.

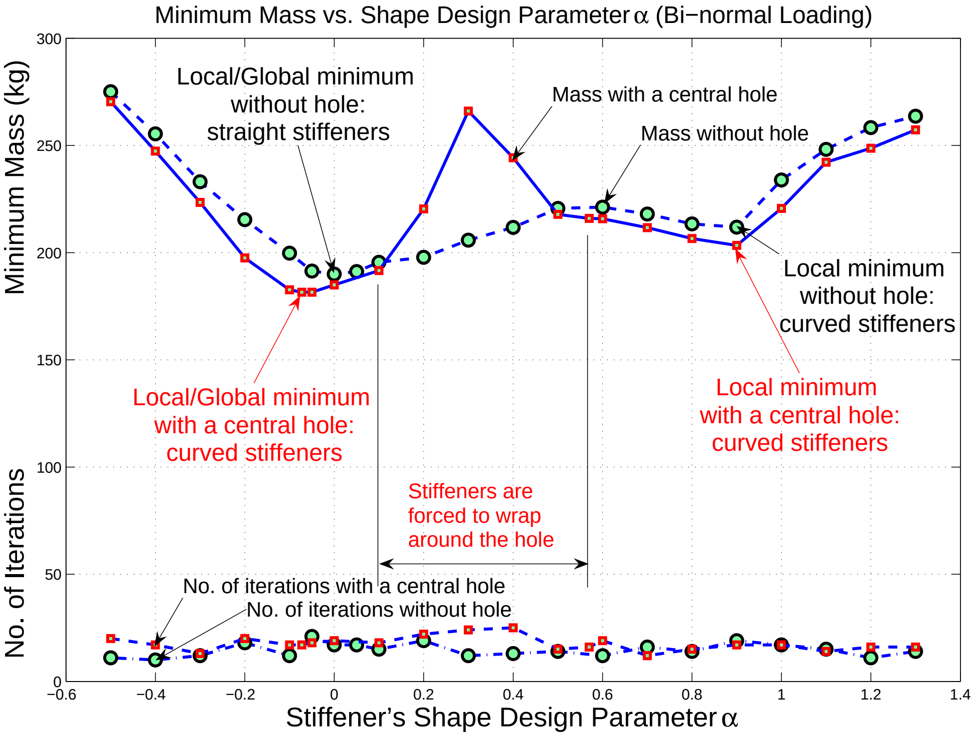

Figure 4.29: Variation of minimum mass vs. shape design parameter α. The global optimal shape is achieved at about $\alpha = 0.0$ with a minimum mass $M_{\mathrm{min}} = 190\mathrm{kg}$. An inclusion of a central hole of radius 0.3m results in curvilinear stiffeners as the global optimal placement, achieved at about $\alpha = -0.0725$ with a minimum mass $M_{\mathrm{min}} = 182\mathrm{kg}$.

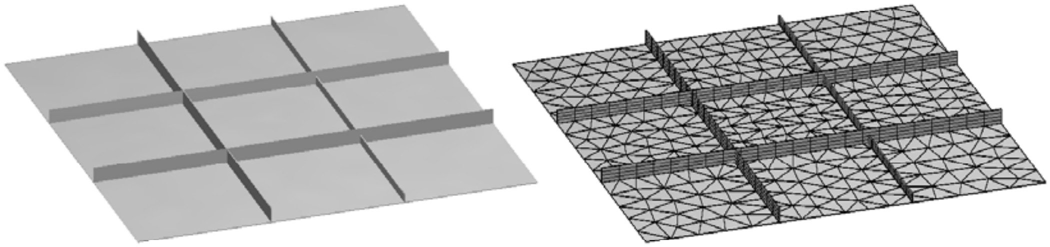

(a) Before the inclusion of the central cutout – global minimum: $\alpha = 0.0$; $M_{\min} = 190$kg; optimal shape: straight stiffeners.

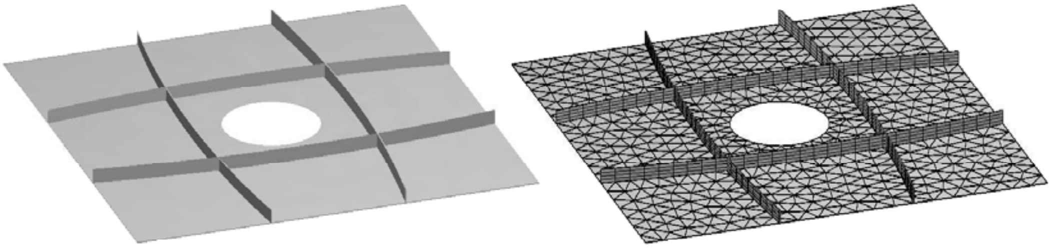

(b) After the inclusion of the central cutout – global minimum: $\alpha = 0.0725$; $M_{\min} = 182$kg; optimal shape: curved stiffeners.

Figure 4.30: A comparison of optimal designs before and after the inclusion of the central cutout of radius 0.3m.

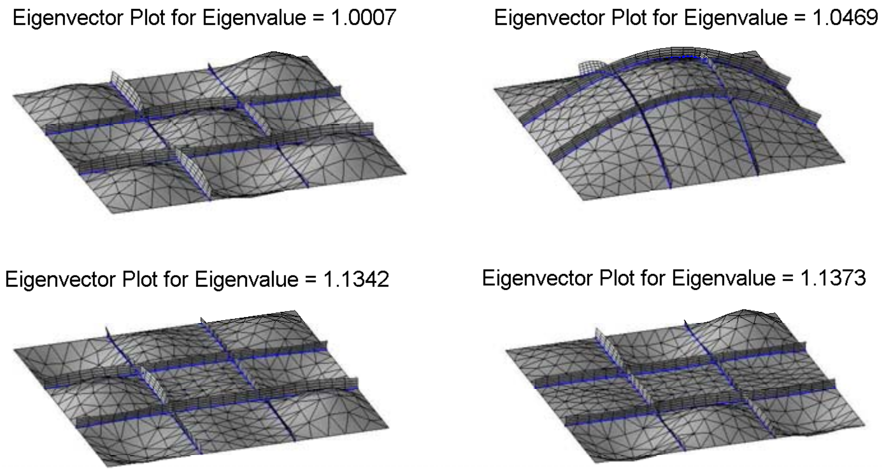

(a) Before the inclusion of the central cutout.

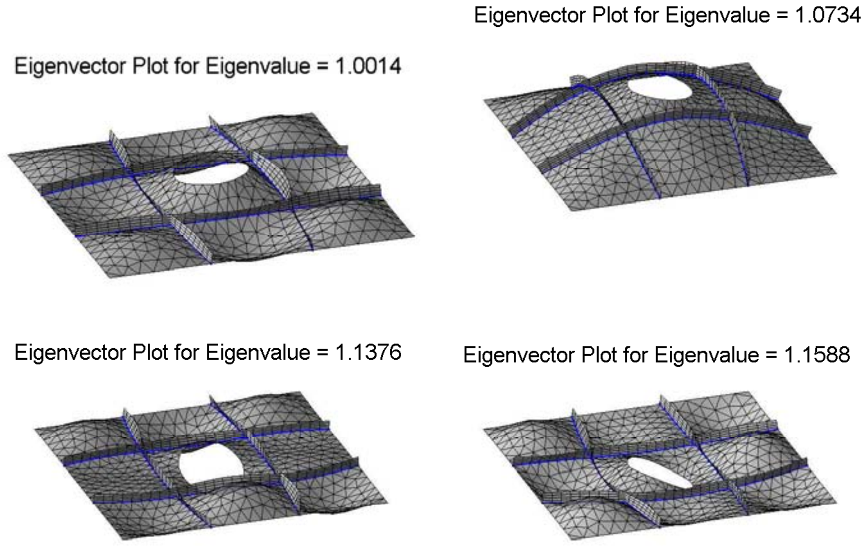

(b) After the inclusion of the central cutout.

Figure 4.31: A comparison of first four buckling modes before and after the inclusion of the central cutout of radius 0.3m.

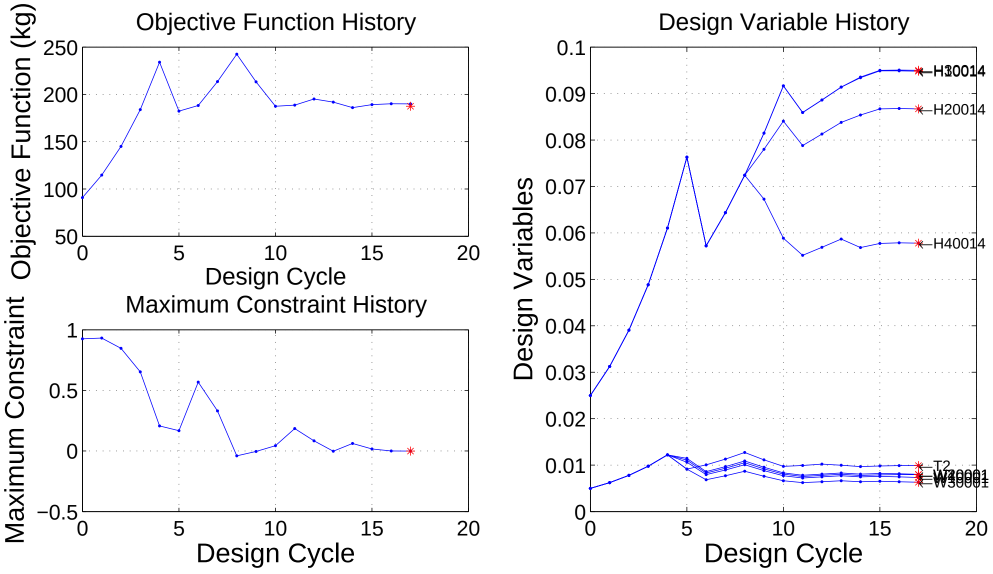

(a) before the inclusion of the central cutout.

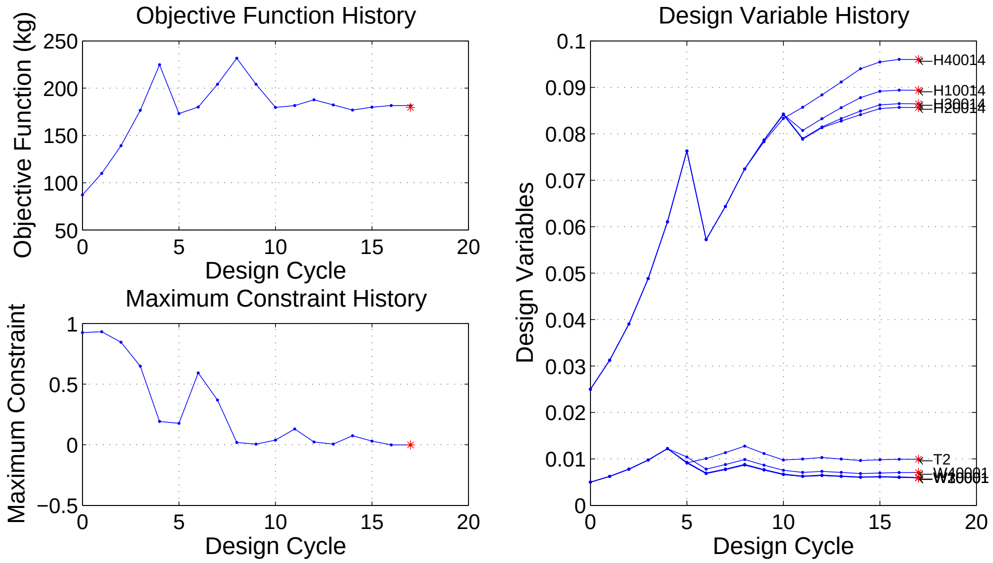

(b) After the inclusion of the central cutout.

Figure 4.32: A comparison of design histories before and after the inclusion of the central cutout of radius 0.3m.

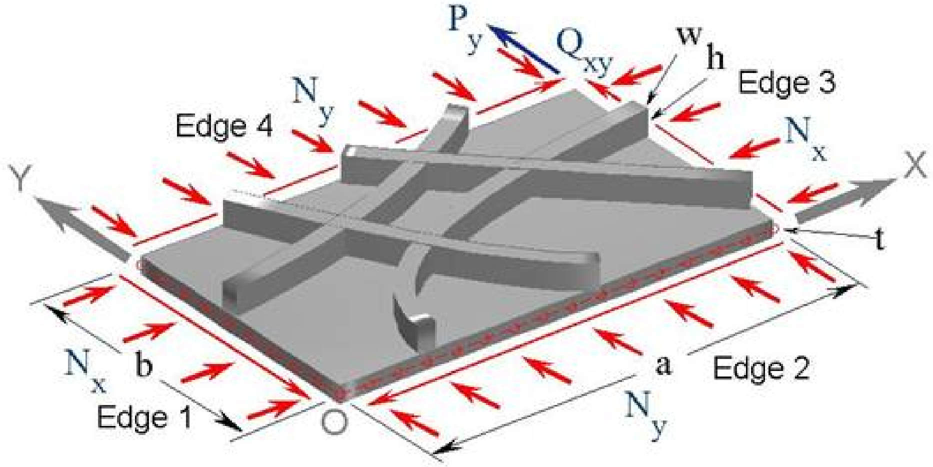

Figure 4.33: Geometrical dimensions ($a = 2.54$m; $b = 2.54$m), bi-normal and shear loading ($N_{\mathrm{x}} = 250$kN/m; $N_{\mathrm{y}} = 0.2N_{\mathrm{x}}$; $Q_{\mathrm{xy}} = 0.5N_{\mathrm{x}}$; $P_{\mathrm{y}} = 0$), and simply supported conditions of a blade stiffened panel. Both stiffeners and plate are made out of aluminum. Initial size and bounds: $t_0 = w_0 = 0.005$m; $h_0 = 5w_0$; $t_{\mathrm{b}} = w_{\mathrm{b}} = [0.0001, 0.1]$m; $h_{\mathrm{b}} = [0.0001, 0.5]$m.

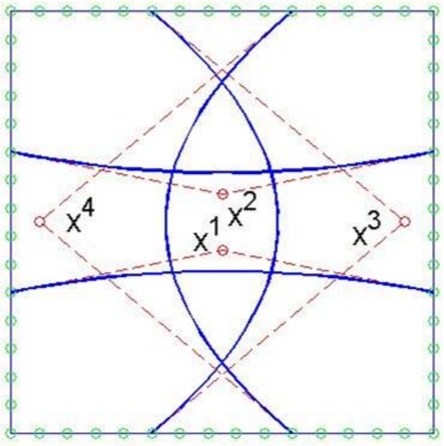

Figure 4.34: Design parameter α_1 controls the motions of two mid control points $\mathbf{x^1}$ and $\mathbf{x^2}$ starting from $\mathbf{x_0^1}$ and $\mathbf{x_0^2}$ by $\alpha_1\mathbf{d_1^1}$ and $\alpha_1\mathbf{d_1^2}$ for stiffeners 1 and 2, respectively. Design parameter α_2 controls the motions of two mid control points $\mathbf{x^3}$ and $\mathbf{x^4}$ starting from $\mathbf{x_0^3}$ and $\mathbf{x_0^4}$ by $\alpha_2\mathbf{d_2^3}$ and $\alpha_2\mathbf{d_2^4}$ for stiffeners 3 and 4, respectively.

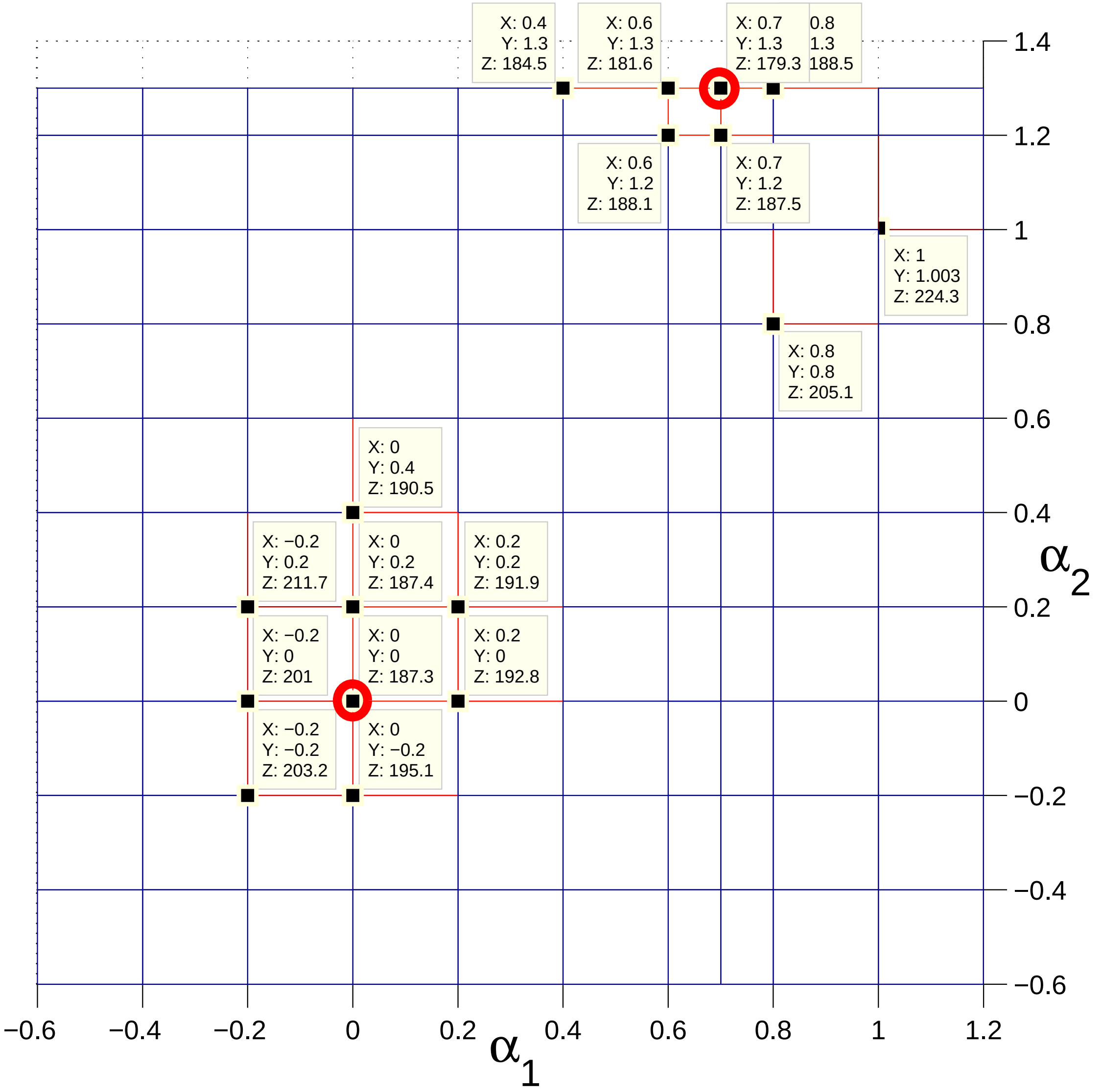

Figure 4.35: Design space of two design parameters: $\alpha_1 = X$ and $\alpha_2 = Y$, with corresponding minimum mass: $M_{\text{min}} = Z$. Two local minima are found as shown as the dark squares inside the circles from 17 discrete points on the 11×11 grids. The maximum number of iterations for size optimization is set to be 100.

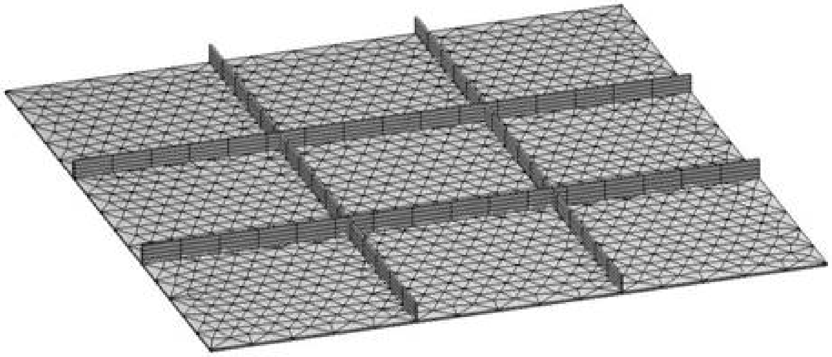

(a) Minimum 1 at $\alpha_1 = 0.0$ and $\alpha_2 = 0.0$. Minimum mass: $M_{\min} =$ 187kg

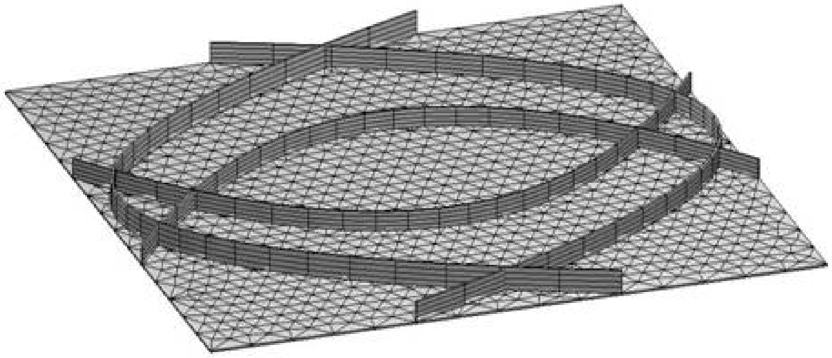

(b) Minimum 2 at $\alpha_1 = 0.7$ and $\alpha_2 = 1.3$. Minimum mass: $M_{\min} =$ 179kg

Figure 4.36: Two local minima vs. two design parameters.

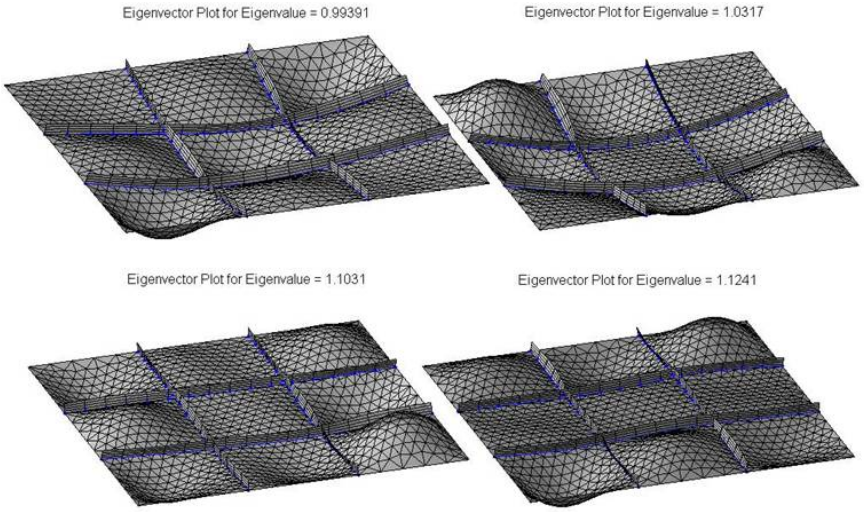

(a) First four buckling modes for minimum 1 at $\alpha_1 = 0.0$ and $\alpha_2 = 0.0$ - straight stiffeners

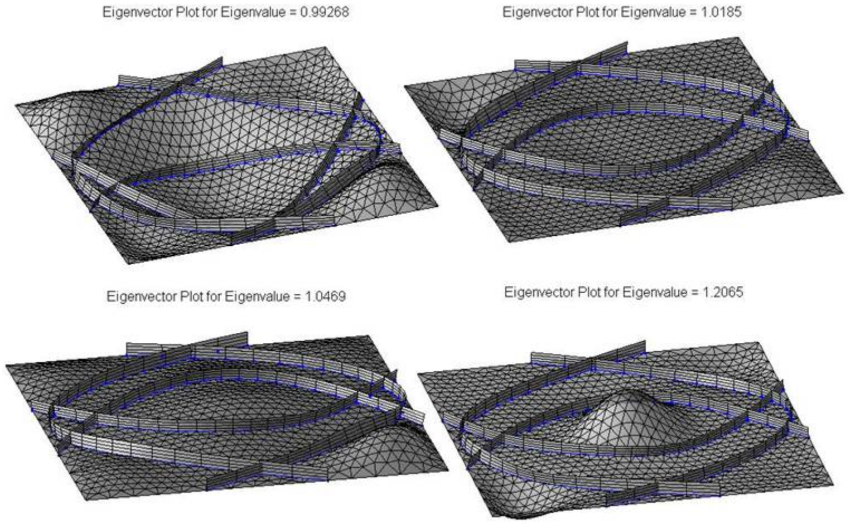

(b) First four buckling modes for minimum 2 at $\alpha_1 = 0.7$ and $\alpha_2 = 1.2$ - curved stiffeners

Figure 4.37: First four buckling modes for minimum 1 and minimum 2.

Chapter 5
Summary and Conclusions

This dissertation dealt with some inverse problems in structural mechanics, searching for causes of observed or desired effects where some regularizations are usually needed to handle the common ill-posed conditions.

Three application fields are covered in this work.

The **first one** is load updating for finite element models, where boundary displacements or strains are assumed given from a *noise-free* measurement and least squares fitting is used to identify load parameters. Therefore, the ill-conditioned problem itself is classified as one with non-unique solutions or high condition number.

The formulation of the load updating is first made for geometrically linear and nonlinear finite element models of beams or frames by using a previously developed four-noded curved beam element. For the purpose of basic studies, the unknown applied load within an element is represented by a linear combination of integrated Legendre polynomials, the coefficients of which are the parameters to be extracted using assumed measured displacements or strains. The inverse problem is formulated as an expanded Least Squares solution problem where the difference between the calculated and measured displacements or strains is minimized, with some intuitive Tikhonov-type regularization terms for enforcing C^0 continuity and smoothing for the extracted load. The limited memory variable metric optimizer L-BFGS-B is used to solve the ill-conditioned least squares problem. The benefits of regularization using the four-noded beam element, polynomials of lower order for load representation, using relative measurement data, richer measured data, smoothing, and enforcing C^0 continuity are to change the underdetermined problem to an overdetermined one. The basic idea is to overcome the ill-posedness of the identification problem by reducing the relative model order or the relative number of unknown variables of the system for given precision.

An extended work (Li and Kapania, 2004) is also made for general finite element models based on MSC.NASTRAN where both plate and solid structures can be handled. The reduced number of the unknown load parameters is used to regularize the ill-conditioned load updating problem, and the parametrization of load is made crossing the element boundary by using NURBS (Non-uniform Rational B-Splines) to represent the load distribution.

The present conclusions may be applied to the measurement based load updating for general finite element models when the measured data are pre-smoothed or the noise in the data is pre-filtered out.

The **second problem** is the placement optimization of a spatially distributed sensing fiber optic sensor for a smart bed using a Genetic Algorithms (GA), where the sensor performance is maximized subjected to constraints on the length of the optical fiber and its maximum initial curvature. The sensor performance function is simplified as the full length integration of the absolute curvature change due to the spatial perturbation from a subject's movement. The problem of the placement of an infinite number of infinitesimal sensing fiber segments is replaced by the problem of the placement of a finite number of the control points since the fiber optic cable is represented by a NURBS curve.

Due to the common problem of multiple solutions for the placement of sensors, a simple binary-coded Genetic Algorithm (GA) is used for the placement of this distributed sensing fiber optic sensor as an illustration to use a GA for a NURBS design. The fitness function of the GA is defined in the sense of the exact penalty function method, where the length and maximum initial curvature of the fiber curve are limited by prescribed upper bounds.

A Java tool is developed as an interactive research and design tool for the fiber optic sensor using GAs.

Two simple examples were given for the placement optimization of the distributed sensing optical fiber for an integrated smart bed. The first example had 6 control points of the NURBS curve for the sensing fiber curve of 2m. The spatial perturbation to the mattress and the sensing fiber was from perturbating a control point of the NURBS for the mattress surface. The second example had 25 control points for the sensing fiber's NURBS curve of 4m. The mattress deformation and its perturbation were calculated using MSC.NASTRAN under a given body pressure and its perturbation. The smart bed was modeled as an elastic mattress core, ignoring effects of both the flexible mattress cover and the sensing optical fiber. This made it possible to perform only a single FEA to obtain the mattress surface deformation for the placement optimization of the sensor, which is important for using a GA that needs a large number of generations. Both examples gave updated placements of the sensors with improved sensor performance.

The further work includes the considerations of (1) using real-valued coded GA with a special treatment for constraints, (2) the variation of the body pressure distribution, (3) the multiple loadings and multiple constraints, and (4) the large initial deformation of the mattress.

Though the specific example is for clinical use, the distributed sensing fiber optic sensor and associated placement methodology can also be used in pilot/passenger seats and structures for flight vehicles. The other potential use is the placement of Fiber Bragg Grating (FBG) sensors for health monitoring structures in both aerospace engineering and civil engineering.

The **third problem** is the size and placement optimization on unitized panels with straight and curvilinear stiffeners, subject to buckling and stress constraints.

The present work uses NURBS for the panel and stiffener representation. The mesh for the panel is generated using an automatic mesh generation algorithm by adapting DistMesh, a triangulation algorithm, while the mesh for stiffeners is pre-generated and fixed. An interface between NASTRAN and MATLAB is developed to automatically transfer the data between the analysis and optimization processes, respectively. An integrated approach to achieve optimal design of stiffened panels under various practical requirements is adopted in the MATLAB environment. The codes with several capabilities, such as NURBS (for geometric model), DistMesh (for mesh generation), 3D display (for visualization of the stiffened panel), and MSC.NASTRAN, are used as subroutines or subprograms. The collection of those codes is called *EBF3paneloptimization*.

The optimization consists of minimizing the weight of the stiffened panel, with design variables being the thickness of the plate and height and width of the stiffener as well as the placement of the stiffeners, subject to buckling and stress constraints under in-plane and out-of-plane loads.

Numerical studies on optimal stiffened panel designs are performed to investigate the effects of certain factors, such as orientation, spacing, location, and curvature, on the optimal designs.

We observe that a curvilinear placement of stiffeners sometimes gives a slightly better design than straight stiffeners. A curvilinear placement of stiffeners is equivalent to an orientation, spacing, location, and intersection placement of infinitesimal straight stiffeners. It also plays a role in topology optimization due to the change of stiffeners' intersections.

Numerical results also show that the stiffened panel optimization is an ill-posed inverse problem with slow convergence due to a large condition-number of the Hessian for the objective function. The simplified scaling of the design variables, and the scaling and shifting of the objective and constraints, are used as techniques to overcome the slow convergence problem. Besides, the non-uniqueness of the optimal designs and a need for a global optimization are also illustrated.

Future work could include the automation of the placement optimization of the stiffeners, more practical types of stiffeners, as well as more practical design objectives and constraints, such as vibration frequencies, acoustic power/pressure, and panel flutter.

The outcome of the present research and the code *EBF3paneloptimization* are being used for trade-off study of some panel designs used for EBF3 research.

Appendix A
Legendre Polynomials

Let $\alpha = 0, 1, \cdots, N_c^e$

$$L_\alpha(x) \equiv \frac{1}{2^\alpha \alpha!} \frac{d^\alpha}{dx^\alpha}(x^2-1)^\alpha \tag{A.1}$$

be the α-*th* Legendre polynomial, and

$$\tilde{L}_\alpha(x) \equiv \gamma_\alpha \int_{-1}^{x} L_\alpha(x)dx \quad \text{for} \quad \alpha \geq 2 \tag{A.2}$$

be the α-*th* integrated Legendre polynomial with

$$\gamma_\alpha = \sqrt{\frac{(2\alpha-3)(2\alpha-1)(2\alpha+1)}{4}} \tag{A.3}$$

By definition,

$$\begin{aligned} \tilde{L}_0(x) &= \frac{1+x}{2} \\ \tilde{L}_1(x) &= \frac{1-x}{2} \end{aligned} \tag{A.4}$$

The properties

$$\begin{aligned}
L_\alpha(x) &= \frac{2\alpha-1}{\alpha} x L_{\alpha-1}(x) - \frac{\alpha-1}{\alpha} L_{\alpha-2}(x); \quad (L_0(x)=1, \quad L_1(x)=x) \\
\int_{-1}^{1} L_\alpha(x) L_\beta(x) dx &= \delta_{\alpha\beta} \frac{2}{2\alpha+1} \\
\tilde{L}_\alpha(x) &= \sqrt{\frac{(2\alpha+1)(2\alpha-3)}{4(2\alpha-1)}} (L_\alpha(x) - L_{\alpha-2}(x)) \\
\tilde{L}_\alpha(-1) &= 0 \\
\tilde{L}_\alpha(1) &= 0
\end{aligned} \tag{A.5}$$

are true for $\alpha \geq 2$.

In the integral, all powers lower than n of the Legendre polynomial yield zero when integrated against the cosine (because of the orthogonality of the cosines.)

Appendix B
Load Coefficient Matrix at the Element Level

In general, for our geometrically nonlinear FEM for the 3-D case, we can start with the state equation of a nonlinear structural system (Kapania and Li, 2003a):

$$\mathbf{R}(\mathbf{a}, \mathbf{c}, \lambda) = \mathbf{q}_{\text{int}}(\mathbf{a}) - \lambda \mathbf{q}_{\text{ext0}}(\mathbf{a}, \mathbf{c}) = 0. \tag{B.1}$$

where $\mathbf{R}$ is the residual vector, $\mathbf{q}_{\text{int}}$ the nodal internal force vector, $\mathbf{q}_{\text{ext0}}$ the nodal external load vector calculated at the applied load level, λ the proportional nodal loading factor, $\mathbf{a} = \mathbf{a}(\mathbf{c}, \lambda)$ the nodal displacement vector, and $\mathbf{c}$ the load (force) coefficient vector: $\mathbf{q}_{\text{int}}$ and $\mathbf{q}_{\text{ext0}}$ are summed from the nodal internal and external load vectors contributed by an element $e \in [1, N_{\text{elm}}]$:

$$\mathbf{q}^e_{\text{int}} = \begin{bmatrix} \mathbf{q}^e_{\text{int}1} \\ \vdots \\ \mathbf{q}^e_{\text{int}I^{\text{e}}_{\text{node}}} \\ \vdots \\ \mathbf{q}^e_{\text{int}N^{\text{e}}_{\text{node}}} \end{bmatrix} \quad \text{and} \quad \mathbf{q}^e_{\text{ext0}} = \begin{bmatrix} \mathbf{q}^e_{\text{ext01}} \\ \vdots \\ \mathbf{q}^e_{\text{ext0}I^{\text{e}}_{\text{node}}} \\ \vdots \\ \mathbf{q}^e_{\text{ext0}N^{\text{e}}_{\text{node}}} \end{bmatrix} \tag{B.2}$$

respectively, where

$$\mathbf{q}^e_{\text{int}I^{\text{e}}_{\text{node}}} = \begin{bmatrix} \mathbf{P}^e_{\text{int}I^{\text{e}}_{\text{node}}} \\ \mathbf{M}^e_{\text{int}I^{\text{e}}_{\text{node}}} \end{bmatrix} \tag{B.3}$$

where

$$\mathbf{P}^e_{\text{int}I^{\text{e}}_{\text{node}}} = \int_0^1 N_{I^{\text{e}}_{\text{node}},\xi} \mathbf{n}^e \mathrm{d}\xi \tag{B.4}$$

and

$$\mathbf{M}^e_{\mathrm{int}I^{\mathrm{e}}_{\mathrm{node}}} = \int_0^1 (N_{I^{\mathrm{e}}_{\mathrm{node}},\xi}\mathbf{m}^e - N_{I^{\mathrm{e}}_{\mathrm{node}}}\hat{\boldsymbol{\varphi}}^e_{,\xi}\mathbf{n}^e)\mathrm{d}\xi \tag{B.5}$$

are the nodal internal force and moment vectors at node $I^{\mathrm{e}}_{\mathrm{node}}$ contributed by element e, respectively; and

$$\mathbf{q}^e_{\mathrm{ext}0I^{\mathrm{e}}_{\mathrm{node}}} = \begin{bmatrix} \mathbf{P}^e_{\mathrm{ext}0I^{\mathrm{e}}_{\mathrm{node}}} \\ \mathbf{M}^e_{\mathrm{ext}0I^{\mathrm{e}}_{\mathrm{node}}} \end{bmatrix} \tag{B.6}$$

where

$$\begin{aligned} \mathbf{P}^e_{\mathrm{ext}0I^{\mathrm{e}}_{\mathrm{node}}} &= \int_0^1 N_{I^{\mathrm{e}}_{\mathrm{node}}}[\boldsymbol{\mathcal{N}}^e_{\mathrm{g}} + \boldsymbol{\mathcal{N}}^e_{\mathrm{d}}\sin(\mathbf{d}^e, \boldsymbol{\varphi}^e_{0,s}) + \boldsymbol{\Lambda}^e\bar{\boldsymbol{\mathcal{N}}}^e_{\mathrm{p}}]\mathcal{J}^e\mathrm{d}\xi \\ &= \int_0^1 N_{I^{\mathrm{e}}_{\mathrm{node}}}[\boldsymbol{\mathcal{N}}^e_{\mathrm{g}} + \boldsymbol{\mathcal{N}}^e_{\mathrm{d}}\sin(\mathbf{d}^e, \boldsymbol{\varphi}^e_{0,s}) + \boldsymbol{\mathcal{N}}^e_{\mathrm{p}}]\mathcal{J}^e\mathrm{d}\xi \end{aligned} \tag{B.7}$$

and

$$\mathbf{M}^e_{\mathrm{ext}0I^{\mathrm{e}}_{\mathrm{node}}} = \mathbf{0} \tag{B.8}$$

are the nodal external force and zero moment vectors at node $I^{\mathrm{e}}_{\mathrm{node}}$ contributed by the distributed force acting on element e at the applied load level, respectively.

Assume that

$$\boldsymbol{\mathcal{N}}^e_l = \mathbf{c}^{le}_\alpha P_\alpha(\xi_1) \tag{B.9}$$

where P_α are the basis functions, taken to be the integrated Legendre polynomials; $\alpha = 1, 2, \cdots, N^e_c$ (summation convention holds for α) with N^e_c as the number of basis functions considered for each element, and $\mathbf{c}^{le}_\alpha$ are the load (force) coefficient vectors for each element, and the subscript $l = \mathrm{g}, \mathrm{d}, \mathrm{p}$ identifies the load type, *i.e.*, the self-weight load, snow load, and pressure load, respectively (for $l = \mathrm{p}$, the material form $\bar{\boldsymbol{\mathcal{N}}}^e_{\mathrm{p}}$ is used instead of the spatial form $\boldsymbol{\mathcal{N}}^e_{\mathrm{p}}$).

Now let's consider the dependency of the three components of the force coefficient vector, *e.g.* $\mathbf{c}^{le}_\alpha$. We know from Eq. (B.9) that $\mathbf{c}^{le}_\alpha$ determine both the direction and the amplitude of the external force distribution over an element. We consider three cases:

1). The 1-D case, *i.e.*, the direction of $\mathbf{c}^{le}_\alpha$ is given over the element by the vector $\mathbf{d}^{le}_1$:

$$\mathbf{c}^{le}_\alpha = x^{le}_{1\alpha}\mathbf{d}^{le}_1 \tag{B.10}$$

2). The 2-D case, *i.e.*, the plane of $\mathbf{c}^{le}_\alpha$ is same over all α and given by the vectors $\mathbf{d}^{le}_1$ and $\mathbf{d}^{le}_2$:

$$\mathbf{c}^{le}_\alpha = x^{le}_{1\alpha}\mathbf{d}^{le}_1 + x^{le}_{2\alpha}\mathbf{d}^{le}_2 \tag{B.11}$$

3). The more general 3-D case, *i.e.*, the direction of $\mathbf{c}^{le}_{N\alpha}$ is unknown:

$$\mathbf{c}^{le}_\alpha = x^{le}_{1\alpha}\mathbf{d}^{l}_1 + x^{le}_{2\alpha}\mathbf{d}^{l}_2 + x^{le}_{3\alpha}\mathbf{d}^{l}_3 \tag{B.12}$$

where $\mathbf{d}^l_i = \mathbf{e}_i \quad \text{for} \quad l = \mathrm{g}, \mathrm{d}$ (self-weight load and snow load); $\mathbf{d}^l_i = \mathbf{t}_i \quad \text{for} \quad l = \mathrm{p}$ (pressure load).

Collectively, we can combine the three cases into one form:

$$\mathbf{c}^{le}_\alpha = \mathbf{D}^{le}\mathbf{x}^{le}_\alpha \tag{B.13}$$

where $\mathbf{x}^{le}_\alpha$ are called independent force coefficient vectors.

Therefore,

$$\mathbf{P}^e_{\mathrm{ext}0I^{\mathrm{e}}_{\mathrm{node}}} = \int_0^1 N_{I^{\mathrm{e}}_{\mathrm{node}}}[\mathbf{c}^{\mathrm{ge}}_\alpha P_\alpha(\xi_1) + \mathbf{c}^{\mathrm{de}}_\alpha P_\alpha(\xi_1)\sin(\mathbf{d}^e, \boldsymbol{\varphi}^e_{0,s}) + \boldsymbol{\Lambda}^e\mathbf{c}^{\mathrm{pe}}_\alpha P_\alpha\xi_1)]\mathcal{J}^e \mathrm{d}\xi \tag{B.14}$$

The variations with respect to load (force) coefficient vectors:

$$\delta_c\mathbf{P}^e_{\mathrm{ext}0I^{\mathrm{e}}_{\mathrm{node}}} = \mathbf{F}^{\mathrm{ge}}_{cI^{\mathrm{e}}_{\mathrm{node}}\alpha}\delta\mathbf{c}^{\mathrm{ge}}_\alpha + \mathbf{F}^{\mathrm{de}}_{cI^{\mathrm{e}}_{\mathrm{node}}\alpha}\delta\mathbf{c}^{\mathrm{de}}_\alpha + \mathbf{F}^{\mathrm{pe}}_{cI^{\mathrm{e}}_{\mathrm{node}}\alpha}\delta\mathbf{c}^{\mathrm{pe}}_\alpha \tag{B.15}$$

where, noticing that $\mathbf{I}_3$ denotes the identity tensor of order two,

$$\begin{aligned}
\mathbf{F}^{\mathrm{ge}}_{cI^{\mathrm{e}}_{\mathrm{node}}\alpha} &= \int_0^1 \mathbf{I}_3 N_{I^{\mathrm{e}}_{\mathrm{node}}} P_\alpha(\xi_1)\mathcal{J}^e \mathrm{d}\xi \\
\mathbf{F}^{\mathrm{de}}_{cI^{\mathrm{e}}_{\mathrm{node}}\alpha} &= \int_0^1 \mathbf{I}_3 N_{I^{\mathrm{e}}_{\mathrm{node}}} P_\alpha(\xi_1)\sin(\mathbf{d}^e, \boldsymbol{\varphi}^e_{0,s})\mathcal{J}^e \mathrm{d}\xi \\
\mathbf{F}^{\mathrm{pe}}_{cI^{\mathrm{e}}_{\mathrm{node}}\alpha} &= \int_0^1 \boldsymbol{\Lambda}^e N_{I^{\mathrm{e}}_{\mathrm{node}}} P_\alpha(\xi_1)\mathcal{J}^e \mathrm{d}\xi
\end{aligned} \tag{B.16}$$

For a single node of an element,

$$\delta_c \mathbf{q}^e_{\mathrm{ext}0 I^{\mathrm{e}}_{\mathrm{node}}} = \tilde{\mathbf{F}}^{\mathrm{ge}}_{cI^{\mathrm{e}}_{\mathrm{node}}\alpha}\delta\mathbf{c}^{\mathrm{ge}}_\alpha + \tilde{\mathbf{F}}^{\mathrm{de}}_{cI^{\mathrm{e}}_{\mathrm{node}}\alpha}\delta\mathbf{c}^{\mathrm{de}}_\alpha + \tilde{\mathbf{F}}^{\mathrm{pe}}_{cI^{\mathrm{e}}_{\mathrm{node}}\alpha}\delta\mathbf{c}^{\mathrm{pe}}_\alpha \tag{B.17}$$

where

$$\tilde{\mathbf{F}}^{le}_{cI^{\mathrm{e}}_{\mathrm{node}}\alpha} = \begin{bmatrix} \mathbf{F}^{le}_{cI^{\mathrm{e}}_{\mathrm{node}}\alpha} \\ \mathbf{0} \end{bmatrix} \tag{B.18}$$

For a single element e with N^e_{node} nodes contributed by load type l, noticing Eq. (B.13),

$$\begin{aligned}
\delta_c \mathbf{q}^{le}_{\mathrm{ext}0} &= \tilde{\mathbf{F}}^{le}_c \delta\mathbf{c}^{le} \\
&= \tilde{\mathbf{F}}^{le}_{c\alpha}\delta\mathbf{c}^{le}_\alpha
\end{aligned} \tag{B.19}$$

$$\begin{aligned}
\delta_x \mathbf{q}^{le}_{\mathrm{ext}0} &= \tilde{\mathbf{F}}^{le}_x \delta\mathbf{x}^{le} \\
&= \tilde{\mathbf{F}}^{le}_{x\alpha}\delta\mathbf{x}^{le}_\alpha \\
&= \tilde{\mathbf{F}}^{le}_{c\alpha}\mathbf{D}^{le}\delta\mathbf{x}^{le}_\alpha
\end{aligned} \tag{B.20}$$

where

$$\tilde{\mathbf{F}}^{le}_x = \begin{bmatrix} \tilde{\mathbf{F}}^{le}_{x1} & \cdots & \tilde{\mathbf{F}}^{le}_{xN_c} \end{bmatrix}, \quad \tilde{\mathbf{F}}^{le}_{x\alpha} = \tilde{\mathbf{F}}^{le}_{c\alpha}\mathbf{D}^{le}, \quad \tilde{\mathbf{F}}^{le}_{c\alpha} = \begin{bmatrix} \tilde{\mathbf{F}}^{le}_{c1\alpha} \\ \vdots \\ \tilde{\mathbf{F}}^{le}_{cN^e_{node}\alpha} \end{bmatrix}, \quad \text{and} \quad \delta\mathbf{x}^{le} = \begin{bmatrix} \delta\mathbf{x}^{le}_1 \\ \vdots \\ \delta\mathbf{x}^{le}_{N^e_c} \end{bmatrix}$$

Appendix C
The Derivatives of the Displacements with Respective to Load Coefficient Vector

In the *linearized* incremental form, the state equation can be written as

$$\mathbf{R} + \Delta\mathbf{R} = \mathbf{0} \tag{C.1}$$

and

$$\begin{aligned} \Delta\mathbf{R} &= \Delta_a\mathbf{R} + \Delta_x\mathbf{R} + \Delta_\lambda\mathbf{R} \\ &= \mathbf{R}_{,\mathbf{a}}\Delta\mathbf{a} + \mathbf{R}_{,\mathbf{x}}\Delta\mathbf{x} + \mathbf{R}_{,\lambda}\Delta\lambda \end{aligned} \tag{C.2}$$

where the linearized increment operator Δ has been decomposed into three parts: the linearized increment Δ_a due to a change in $\mathbf{a}$, linearized increment Δ_x (or Δ_c) due to a change in $\mathbf{x}$ (or $\mathbf{c}$), and linearized increment Δ_λ due to a change in λ. The Jacobians $\mathbf{R}_{,\mathbf{a}}$, $\mathbf{R}_{,\mathbf{x}}$, and $\mathbf{R}_{,\lambda}$ are the *partial* derivatives of the residual $\mathbf{R}$ with respect to the state vector $\mathbf{a}$, load design vector $\mathbf{x}$, and load factor λ, respectively:

$$\mathbf{R}_{,\mathbf{a}} = \mathbf{R}_{,\mathbf{a}}(\mathbf{a}, \mathbf{x}, \lambda) = \mathbf{q}_{\mathrm{int},\mathbf{a}} - \lambda\mathbf{q}_{\mathrm{ext0},\mathbf{a}} \tag{C.3}$$

$$\mathbf{R}_{,\mathbf{c}} = \mathbf{R}_{,\mathbf{x}}(\mathbf{a}, \mathbf{x}, \lambda) = \mathbf{q}_{\mathrm{int},\mathbf{x}} - \lambda\mathbf{q}_{\mathrm{ext0},\mathbf{x}} = -\lambda\mathbf{q}_{\mathrm{ext0},\mathbf{x}} \tag{C.4}$$

and

$$\mathbf{R}_{,\lambda} = \mathbf{R}_{,\lambda}(\mathbf{a}, \mathbf{x}) = -\mathbf{q}_{\mathrm{ext0}} \tag{C.5}$$

Also, $\mathbf{R}_{,\mathbf{a}}$ is known as the tangential stiffness matrix of the system:

$$\mathbf{K}_{\mathrm{T}} = \mathbf{K}_{\mathrm{T}}(\mathbf{a}, \mathbf{x}, \lambda) = \mathbf{R}_{,\mathbf{a}} \tag{C.6}$$

which is *nonsymmetric* for a general loading case, *e.g.* when the pressure load is considered.

Therefore, we can write the *augmented* linearized incremental state equation as

$$\mathbf{R} + \mathbf{R}_{,\mathbf{a}}\Delta\mathbf{a} + \mathbf{R}_{,\mathbf{x}}\Delta\mathbf{x} + \mathbf{R}_{,\lambda}\Delta\lambda = \mathbf{0} \tag{C.7}$$

The residual vector vanishes at the equilibrium for given load factor λ:

$$\mathbf{R} = \mathbf{0} \tag{C.8}$$

Thus, we have the *augmented* linearized incremental state equation at equilibrium:

$$\mathbf{K}_{\mathrm{T}}\Delta\mathbf{a} + \mathbf{R}_{,\mathbf{x}}\Delta\mathbf{x} = \mathbf{0} \tag{C.9}$$

or

$$\mathbf{K}_{\mathrm{T}}\Delta\mathbf{a} - \lambda\mathbf{q}_{\mathrm{ext0},\mathbf{x}}\Delta\mathbf{x} = \mathbf{0} \tag{C.10}$$

or

$$\mathbf{a}_{,\mathbf{x}} = \lambda\mathbf{K}_{\mathrm{T}}^{-1}\mathbf{q}_{\mathrm{ext0},\mathbf{x}} \tag{C.11}$$

where $\mathbf{a}_{,\mathbf{x}}$ is the sensitivity of displacement vector with respect to the load design vector $\mathbf{x}$ and $\mathbf{q}_{\mathrm{ext0},\mathbf{x}}$ is the global force coefficient matrix, which is obtained by the assembling operation using the relations given in Eqs. (B.15-B.21).

Appendix D
The Derivatives of the Strains with Respect to Load Coefficient Vector

For the translational strain vector in the material form, one has, noticing Section 3.3 of Kapania and Li (2003a),

$$\begin{aligned}\Delta_x\bar{\boldsymbol{\varepsilon}} &= \bar{\boldsymbol{\varepsilon}}_{,x_\alpha}\Delta x_\alpha \\ &= \boldsymbol{\Lambda}^t(\Delta_x\boldsymbol{\varphi}_{,\xi_1} + \hat{\boldsymbol{\varphi}}_{,\xi_1}\Delta_x\mathbf{w}) \\ &= \boldsymbol{\Lambda}^t[(\boldsymbol{\varphi}_{,\xi_1})_{,x_\alpha} + \hat{\boldsymbol{\varphi}}_{,\xi_1}\mathbf{w}_{,x_\alpha}]\Delta x_\alpha \\ &= (\mathbf{e}_j\otimes\mathbf{t}_j)[(\boldsymbol{\varphi}_{,\xi_1})_{,x_\alpha} + \hat{\boldsymbol{\varphi}}_{,\xi_1}\mathbf{w}_{,x_\alpha}]\Delta x_\alpha \\ &= \{\mathbf{t}_j\cdot[(\boldsymbol{\varphi}_{,\xi_1})_{,x_\alpha} + \hat{\boldsymbol{\varphi}}_{,\xi_1}\mathbf{w}_{,x_\alpha}]\}\mathbf{e}_j\Delta x_\alpha \end{aligned} \tag{D.1}$$

For the bending strain vector in the material form, one has

$$\begin{aligned}\Delta_x\bar{\boldsymbol{\kappa}} &= \bar{\boldsymbol{\kappa}}_{,x_\alpha}\Delta x_\alpha \\ &= \boldsymbol{\Lambda}^t\Delta_x\mathbf{w}_{,\xi_1} \\ &= \boldsymbol{\Lambda}^t(\mathbf{w}_{,\xi_1})_{,x_\alpha}\Delta x_\alpha \\ &= [\mathbf{t}_j\cdot(\mathbf{w}_{,\xi_1})_{,x_\alpha}]\mathbf{e}_j\Delta x_\alpha \end{aligned} \tag{D.2}$$

For the position vector of the mid-curve of the deformed beam, one has

$$\begin{aligned}
\Delta_x \boldsymbol{\varphi} &= \boldsymbol{\varphi}_{,x_\alpha} \Delta x_\alpha \\
&= \Delta_x (\boldsymbol{\varphi}_0 + \mathbf{u}) \\
&= \Delta_x \boldsymbol{\varphi}_0 + \Delta_x \mathbf{u} \\
&= \Delta_x \mathbf{u} \\
&= \mathbf{u}_{,x_\alpha} \Delta x_\alpha
\end{aligned} \tag{D.3}$$

$$\begin{aligned}
\Delta_x \boldsymbol{\varphi}_{,\xi_1} &= (\boldsymbol{\varphi}_{,\xi_1})_{,x_\alpha} \Delta x_\alpha \\
&= (\boldsymbol{\varphi}_{,x_\alpha})_{,\xi_1} \Delta x_\alpha
\end{aligned} \tag{D.4}$$

For the incremental rotation vector, one has

$$\Delta_x \mathbf{w} = \mathbf{w}_{,x_\alpha} \Delta x_\alpha \tag{D.5}$$

and

$$\begin{aligned}
\Delta_x \mathbf{w}_{,\xi_1} &= (\mathbf{w}_{,\xi_1})_{,x_\alpha} \Delta x_\alpha \\
&= (\mathbf{w}_{,x_\alpha})_{,\xi_1} \Delta x_\alpha
\end{aligned} \tag{D.6}$$

At the element level,

$$(\boldsymbol{\varphi}^e_{,\xi_1})_{,x_\alpha} = N_{I,\xi_1} \boldsymbol{\varphi}^e_{I,x_\alpha} = N_{I,\xi_1} \mathbf{u}^e_{I,x_\alpha} \tag{D.7}$$

$$\mathbf{w}^e_{,x_\alpha} = N_I \mathbf{w}^e_{I,x_\alpha} \tag{D.8}$$

$$(\mathbf{w}^e_{,\xi_1})_{,x_\alpha} = N_{I,\xi_1} \mathbf{w}^e_{I,x_\alpha} \tag{D.9}$$

where $N_I = N_I(\xi)$ is the Lagrangian interpolation function of node I.

References

Abdullah, M., A. Richardson, and J. Hanif (2001). "Online Monitoring of Highway Bridge Construction Using Fiber Bragg Grating Sensors". *Earthquake Engineering & Structural Dynamics 30*(8), 1167–1184.

Ahmadian, H., J. Mottershead, and M. Friswell (1998). "Regularisation Methods for Finite Element Model Updating". *Mechanical Systems and Signal Processing 12*(1), 47–64.

Arora, J. (1989). *Introduction to Optimum Design.* New York: McGraw-Hill Publishing Co.

Avitabile, P. (2000). "Model-updating – Endless Possibilities". *Sound and Vibration 34*(9), 20–28.

Banks, H. (2002). "Tutorial on Differential Equation Modeling and Inverse Problems". In *Inverse Problem Methodology in Complex Stochastic Models September 2002 - January 2003, Statistical and Applied Mathematical Sciences Institute:* `http://www.samsi.info/talks/inverse/Inverse-Banks.pdf`.

Barnardo, C. and P. Maincon (2004). "Inverse Finite Element Eethods - Part IV: Sensitivity to Modelling errors". In A. Zingoni (Ed.), *CD Proceedings of Second International Conference on Structural Engineering, Mechanics and Computation, SEMC 2004.*

Bates, D. and D. Watts (1988). *Nonlinear Regression and Its Applications.* New York: Wiley.

Bonnet, M. and A. Constantinescu (1996). "Identification of Planar Cracks by Complete Overdetermined Data: Inversion Formulae". *Inverse Problems 12*(5), 553–563.

Bonnet, M. and A. Constantinescu (2005). "Inverse Problems in Elasticity". *Inverse Problems 21*(2), R1–R50.

Brakhage, H. (1987). "On Ill-Posed Problems and The Method of Conjugate Gradients". In *Engl and Groetsch (1987).*

Burger, M. and W. Muhlhuber (2002). "Iterative Regularization of Parameter Identification Problems by Sequential Quadratic Programming Methods". *Inverse Problems 18*(4), 943–969.

Byrd, R., P. Lu, J. Nocedal, and C. Zhu (1995). "A Limited Memory Algorithm for Bound Constrained Optimization". *SIAM Journal on Computing 16*(5), 1190–1208.

Chen, S. and M. Geradin (1996). "Dynamic Force Identification for Beamlike Structures Using an Improved Dynamic Stiffness Method". *SIAM Journal on Computing 3*(3), 183–191.

Chiroiu, C., L. Munteanu, V. Chiroiu, P. Delsanto, and M. Scalerandi (2000). "A Genetic Algorithm for Determination of the Elastic Constants of a Monoclinic Crystal". *Inverse Problems 16*(1), 121–132.

Chock, J. and R. Kapania (2003). "Load Updating for Finite Element Models". *AIAA Journal 41*(9), 1667–1673.

Chock, J. and R. Kapania (2004). "Finite Element Load Updating for Plates". In *Paper AIAA-2004-2004, 45th AIAA/ASME/ASCE/AHS/ASC Structures, Structural Dynamics, and Materials Conference and Exhibit April 19-22, 2004*, Palm Springs, CA.

Davisy, M., A. Kerseyy, J. Sirkisz, and E. Friebeley (1996). "Shape and Vibration Mode Sensing Using a Fiber Optic Bragg Grating Array ". *Smart Materials and Structures 5*(6), 759–765.

Dunn, S. (1976). *Technique for Unique Optimization of Dynamic Finite Element Models.* New York: Academic Press.

Eller, M. (1996). "Identification of Cracks in Three-Dimensional Bodies by Many Boundary Measurements". *Inverse Problems 12*(4), 395–408.

Elliott, K., J. Juang, and J. Robinson (1988). "Force Prediction Using Singular Decomposition". In *Proceedings of the 6th International Modal Analysis Conference*, pp. 1582–1588.

Engl, H. and C. W. Groetsch (1987). *Inverse and Ill-Posed Problems.* Orlando: Academic Press.

Engl, H. and P. Kugler (2003). "Nonlinear Inverse Problems: Theoretical Aspects and Some Industrial Applications". In *Inverse Problems: Computational Methods and Emerging Applications Tutorials:* `http://www.ipam.ucla.edu/publications/invtut/invtut_hengl_pkugler.pdf`.

Eriksson, J. and M. Gulliksson (2003). "Local Results for the Gauss-Newton Method on Constrained Rank-Deficient Nonlinear Least Squares". *Mathematics of Computation 73*(248), 1865–1883.

Ewing, R., T. Lin, and Y. Lin (1999). "A Mixed Least-Squares Method for an Inverse Problem of a Nonlinear Beam Equation". *Inverse Problems 15*(1), 19–32.

Fabunmi, J. (1986). "Effects of Structural Modes on Vibratory Force Determination by the Pseudoinverse Technique". *AIAA Journal 24*(3), 504–509.

Farin, G. (1990). *Curves and Surfaces for Computer Aided Geometric Design: A Practical Guide*. New York: 2nd Ed. Academic Press, Inc.

Faupel, M. (1998). GAJIT - A Simple Java Genetic Algorithms Package: `http://www.micropraxis.com/gajit/index.html`.

Feijoo, G., A. Oberai, , and P. Pinsky (2004). "An Application of Shape Optimization in the Solution of Inverse Acoustic Scattering Problems". *Inverse Problems 20*(1), 199–228.

Frecker, M. (2003). "Recent Advances in Optimization of Smart Structures and Actuators". *Journal of Intelligent Material Systems and Structures 14*(4–5), 207–216.

Friswell, M. and J. Mottershead (1995). *Finite Element Model Updating in Structural Dynamics*. Kluwer Academic Publishers.

Gerdon, G. and Z. Gürdal (1985). "Optimal Design of Geodesically Stiffened Composite Cylindrical Shells". *AIAA Journal 23*(11), 1753–1761.

Gladwelly, G. (1997). "Inverse Vibration Problems for Finite-Element Models". *Inverse Problems 13*(2), 311–322.

Grall, B. and Z. Gürdal (1992). "Optimal Design of Geodesically Stiffened Composite Cylindrical Shells". NASA-CR-190608.

Gregory, D., T. Priddy, and D. Smallwood (1986). "Experimental Determination of the Dynamic Forces Acting on Non-Rigid Bodies". In *SAE Technical Paper Series, Paper 861791, Aerospace Technology Conference and Expo, SAE*, Warrendale, PA.

Guo, H.-Y., L. Zhang, L.-L. Zhang, and J.-X. Zhou (2004). "Optimal Placement of Sensors for Structural Health Monitoring Using Improved Genetic Algorithms". *Smart Materials and Structures 13*(3), 528–534.

Gürdal, Z. and G. Gerdon (1993). "Optimal Design of Geodesically Stiffened Composite Cylindrical Shells". *Composites Engineering 3*(12), 1131–1147.

Gürdal, Z., R. Haftka, and P. Hajela (1999). *Design and Optimization of Laminated Composite Materials*. New York: John Wiley & Sons, Inc.

Hanke, M. (1995). *Conjugate Gradient Type Methods for Ill-Posed Problems*. Harlow, Essex: Longman Scientific & Technical.

Hansen, P. and D. O'Leary (1993). "The Use of the L-Curve in the Regularization of Discrete Ill-Posed Problems". *SIAM Journal on Scientific Computing 14*(6), 1487–1503.

Hasanov, A. and A. Mamedov (1994). "An Inverse Problem Related to the Determination of Elastoplastic Properties of a Plate". *Inverse Problems 10*(3), 601–615.

Hemez, F. and C. Farhat (1994). “An Energy Based Optimum Sensor Placement Criterion and Its Application to Structure Damage Detection”. In *Proceedings of 12th International Modal Analysis Conference*, Honolulu, HI: Society of ExperimentalMechanics.

Hillary, B. and D. Ewins (1984). “The Use of Strain Gauges in Force Determination and Frequency Response Function Measurements”. In *Proceedings of the 2nd Internal Modal Analysis Conference*, pp. 627–634.

Hiramoto, K., H. Doki, and G. Obinata (2000). “ Optimal Sensor/Actuator Placement for Active Vibration Control Using Explicit Solution of Algebraic Riccati Equation”. *Journal of Sound and Vibration 229*(5), 1057–1075.

Holland, J. (1975). *Adaptation in Natural and Artificial Systems.* Ann Arbor: The University of Michigan Press.

Houck, C., J. Joines, and K. G.M. (1995). A Genetic Algorithm for Function Optimization: A Matlab Implementation: `http://www.ie.ncsu.edu/mirage/GAToolBox/gaot/papers/gaotv5.ps`.

Johnson, C. (1998a). “Identification of Unknown Static Load Distributions on Beams from Measurements”. In *Southeastern Conference on Theoretical and Applied Mechanics (19th)*, Volume 19, pp. 159–171.

Johnson, C. (1998b). “Identification of Unknown, Time-Varying Forces/Moments in Dynamics and Vibration Problems Using a New Approach to Deconvolution”. *Shock and Vibration 5*, 181–197.

Johnson, C. (1998c). “The Necessary and Sufficient Conditions for Unknown Force/Moment Identification”. In *Southeastern Conference on Theoretical and Applied Mechanics (19th)*, Volume 19, pp. 192–203.

Kaipio, J., V. Kolehmainen, M. Vauhkonen, and E. Somersalo (1999). “Inverse Problems with Structural Prior Information”. *Inverse Problems 15*(3), 713–729.

Kammer, D. (1991a). “Effect of Model Error on Sensor Placement for On-Orbit Modal Identification of Large Space Structures”. In *Paper AIAA-1991-1180, 32nd AIAA/ASME/ASCE/AHS/ASC Structures, Structural Dynamics, and Materials Conference, Apr. 8-10, 1991*, Baltimore, MD.

Kammer, D. (1991b). “Sensor Placement for On-Orbit Modal Identification and Correlation of Large Space Structures ”. *Journal of Guidance, Control, and Dynamics 14*(2), 251–259.

Kammer, D. and R. Brillhart (1994). “Optimal Sensor Placement for Modal Identification Using System-Realization Methods”. In *AIAA-1994-1730 , AIAA/ASME Adaptive*

Structures Forum , Apr. 21-22, 1994, Technical Papers (A94-23227 05-39), Washington, American Institute of Aeronautics and Astronautics, 1994, Hilton Head, SC.

Kapania, R. and J. Li (2003a). "A Formulation and Implementation of Geometrically Exact Curved Beam Elements Incorporating Finite Strains and Finite Rotations". *Computational Mechanics 30*(5–6), 444–459.

Kapania, R. and J. Li (2003b). "On a Geometrically Exact Curved/Twisted Beam Theory under Rigid Cross-Section Assumption". *Computational Mechanics 30*(5-6), 428–443.

Kim, Y.-Y. and R. Kapania (2004, January). *"Inverse Problems in Structural Damage Identification, Structural Optimization, and Optical Medical Imaging Using Artificial Neural Networks"*. Ph. D. thesis, Aerospace Engineering, Virginia Polytechnic Institute and State University, Blacksburg, VA.

Law, S. and Y. Fang (2001). "Moving Force Identification: Optimal State Estimation Approach". *Journal of Sound and Vibration 239*(2), 233–254.

Li, J. and R. Kapania (2004). "Load Updating for Finite Element Models Using Reduced Number of Unknown Load Coefficients". In *Paper IAA-2004-4559, 10th AIAA/ISSMO Multidisciplinary Analysis and Optimization Conference, August 30-September 1, 2004*, Albany, NY.

Li, J., R. Kapania, and W. Spillman Jr (2004). "Placement Optimization of Fiber Optic Sensors for a Smart Bed Using Genetic Algorithms". In *Paper AIAA-2004-4334, 10th AIAA/ISSMO Multidisciplinary Analysis and Optimization Conference, Aug. 30-Sep. 1, 2004*, Albany, NY.

Lim, T. (1991). "Sensor Placement for On-Orbit Modal Identification". In *Proceedings 32nd AIAA/ASME/ASCE/AHS/ASC Structures, Structural Dynamics, and Materials Conference*, Reston, VA: American Institute of Aeronautics and Astronautics, pp. 247–261.

Lin, Y.-B., C.-L. Pan, Y.-H. Kuo, K.-C. Chang, and J.-C. Chern (2005). "Online Monitoring of Highway Bridge Construction Using Fiber Bragg Grating Sensors". *Smart Materials and Structures 14*(5), 1075–1082.

Louis, A. (1999). "A Unified Approach to Regularization Methods for Linear Ill-Posed Problems". *Inverse Problems 15*(2), 489–498.

Maincon, P. (2004a). "Inverse FEM I: Estimating Loads and Structural Response from Measurements". In A. Zingoni (Ed.), *CD Proceedings of Second International Conference on Structural Engineering, Mechanics and Computation, SEMC 2004.*

Maincon, P. (2004b). "Inverse FEM II: Dynamic and Non-Linear Problems". In A. Zingoni (Ed.), *CD Proceedings of Second International Conference on Structural Engineering, Mechanics and Computation, SEMC 2004.*

Maree, J. and P. Maincon (2004). “Inverse Finite Element Methods - Part III: Sensitivity to Measurement Set-Up”. In A. Zingoni (Ed.), *CD Proceedings of Second International Conference on Structural Engineering, Mechanics and Computation, SEMC 2004*.

Markus, A., G. Renner, and J. Vancza (1997). “Spline Interpolation with Genetic Algorithms”. In *Proceedings of 1997 International Conference on Shape Modeling and Applications, March 3-6, 1997*, Aizu-Wakamatsu, Japan, pp. 47–54.

Michalewicz, Z. (1994). *Genetic Algorithms + Data Structures = Evolution Programs. AI Series*. New York: Springer-Verlag.

Michell, A. (1904). “The Limits of Economy of Material in Framed Structures”. *Philosophical Magazine 8*(47), 589–597.

Miller, R. (1998). “ Optimal Sensor Placement via Gaussian Quadrature”. *Applied Mathematics and Computation 97*(1), 79–91.

Miller, R., R. Miller, and B. Brown (1997). *Beyond ANOVA: Basics of Applied Statistics.* Boca Raton, FL: Chapman & Hall.

Mottershead, J. and M. Friswell (1993). “Model Updating in Structural Dynamics: A Survey”. *Journal of Sound and Vibration 167*(2), 347–375.

Mroz, Z. and A. Garstecki (2005). “Optimal Loading Conditions in the Design and Identification of Structures. Part 1: Discrete Formulation”. *Structural and Multidisciplinary Optimization 29*(1), 1–18.

MSC.Software (2004). “MSC NASTRAN 2004-Sensitivity and Optimization Users Guide”. MSC Software Corporation, Los Angeles, CA.

MSC.Software (2005). “MSC NASTRAN 2005-Quick Reference Guide”. MSC Software Corporation, Los Angeles, CA,.

Nicol, K. and D. Rusteberg (1993). “Pressure Distribution on Mattresses”. *Journal of Biotechnology 26*(12), 1479–1486.

Padula, S. and R. Kincaid (1999). “Optimization Strategies for Sensor and Actuator Placement”. NASA/TM-1999-209126.

Park, H. and Y. Park (1994). “Transient Response of an Impacted Beam and Indirect Impact Force Identification Using Strain Measurements”. *Shock and Vibration 1*, 267–278.

Persson, P.-O. and G. Strang (2004). “A Simple Mesh Generator in MATLAB”. *SIAM Review 46*(2), 329–345.

Pilkey, W. and J. Kalinowski (1972). “Identification of Shock and Vibration Forces”. In *System Identification of Vibrating Structures, ASME*, pp. 73–86.

Prosser, W. (2003). "Development of Structural Health Management Technology for Aerospace Vehicles". NASA-2003-jannaf-whp.

Rattray, R., D. Burns, and E. Salin (1999). "Peak Fitting and Deconvolution for Determination of the Impulse Response Function of the Sample Introduction System in Flow Injection Inductively Coupled Plasma Spectrometry". *Applied Spectroscopy 53*(12), 1642–1645.

Renton, W., D. Olcott, W. Roeseler, R. Batzer, W. Baron, and A. Velicki (2004). "Future of Flight Vehicle Structures (2002-2023)". *Journal of Aircraft 41*(5), 986–998.

Rieder, A. (1999). "On the Regularization of Nonlinear Ill-Posed Problems via Inexact Newton Iterations". *Inverse Problems 15*(1), 309–327.

Ring, W. (1999). "Identification of the Load of a Partially Breaking Beam from Inclination Measurements". *Inverse Problems 15*(4), 1003–1020.

Roberts, A. and E. Garboczi (2002). "Elastic Properties of Model Random Three-Dimensional Open-Cell Solids". *Journal of the Mechanics and Physics of Solids 50*(1), 33–55.

Sabatier, P. (1995). "A Patchwork Approach to Problems with Boundary Measurements". *Inverse Problems 11*(6), 1233–1245.

Schmitt, L. (1960). "Structural Design by Systematic Synthesis". In *Proceedings of 2nd Conference on Electronic Computation. ASCE*, New York, pp. 105–122.

Schulze, M. and E. Sachs (2002, August). *"Parameter Identification for Underdetermined Systems Arising in Option Pricing Models and Neural Networks"*. Ph. D. thesis, Mathematik, Universität Trier, D-54286 Trier.

Snieder, R. (1998). "The Role of Nonlinearity in Inverse Problems". *Inverse Problems 14*(3), 387–404.

Spillman Jr., W., M. Mayer, J. Bennett, J. Gong, K. Meissner, B. Davis, R. Claus, A. Muelenaer Jr., and X. Xu (2004). "A 'Smart' Bed for Non-Intrusive Monitoring of Patient Physiological Factors". *Journal of Measurement Science & Technology 15*, 1614–1620.

Spink, M. (2000). NURBS Toolbox for SCILAB and MATLAB: `http://www.aria.uklinux.net/nurbs.php3`.

Starkey, J. and G. Merrill (1989). "On the Ill-conditioned Nature of Indirect Force-Measurement Techniques". *Journal of Modal Analysis 4*(3), 103–108.

Stevens, K. (1987). "Force Identification Problems - An Overview". In *Proceedings of the 1987 Society for Experimental Mechanics Spring Conference on Experimental Mechanics*, pp. 838–844.

Taminger, K. and R. Hafley (2003). “Electron Beam Freeform Fabrication: A Rapid Metal Deposition Process”. In *3rd Annual Automotive Composites Conference*, Troy, Michigan.

Tikhonov, A. and V. Arsenin (1977). *Solutions of Ill-Posed Problems*. New York: Wiley.

Trivailo, P., G. Dulikravich, S. D., and T. Gilbert (2004). “Inverse Problem of Aircraft Structural Parameter Estimation: Application of Neural Networks”. In *Inverse Problems, Design and Optimization Symposium*, Rio de Janeiro, Brazil.

Trivailo, P., T. Gilbert, E. Glessich, and D. Sgarioto (2004). “Inverse Problem of Aircraft Structural Parameter Identification: Application of Genetic Algorithms Compared with Artificial Neural Networks”. In *Inverse Problems, Design and Optimization Symposium*, Rio de Janeiro, Brazil.

Udd, E., W. Schulz, J. Seim, J. Corones, and H. Laylor (February 1998). “Fiber Optic Sensors for Infrastructure Applications”. Technical Report SPR 374 (Final), Oregon Department of Transportation.

Udwadia, F. and J. Garba (1985). “Optimal Sensor Locations for Structural Identification”. In *Proceedings of JPL Workgroup on Identification and Control of Flexible Space Structures*, San Diego, CA, pp. 247–261.

VR&D (1999). “DOT, Design Optimization Tools Users Manual, Version 5.0”. Research & Development, Inc., Colorado Springs, CO,.

Walpole, R. and R. Myers (1989). *Probability and Statistics for Engineers and Scientists*. New York: 4th ed., Macmillan Publishing Company.

Wang, M., T. Kreitinger, and H. Luo (1987). “Force Identification from Structural Response”. In *Proceedings of the 1987 SEM Spring Conference on Experimental Mechanics*, Houston, TX, pp. 851–855.

Worden, K. and A. Burrows (2001). “Optimal Sensor Placement for Fault Detection”. *Engineering Structures 23*(8), 885–901.

Wouwer, A., N. Point, S. Porteman, and M. Remy (2000). “An Approach to the Selection of Optimal Sensor Locations in Distributed Parameter Systems”. *Journal of Process Control 10*(4), 291–300.

Zhang, H., B. Lennox, P. Goulding, and A. Y.-T. Leung (2000). “A Float-Encoded Genetic Algorithm Technique for Integrated Optimization of Piezoelectric Actuator and Sensor Placement and Feedback Gains”. *Smart Materials and Structures 9*(4), 552–557.

Zhu, C., R. Byrd, L. P., and J. Nocedal (February 1994). “L-BFGS-B: FORTRAN Subroutines for Large Scale Bound Constrained Optimization”. Technical Report NAM-11, EECS Department, Northwestern University.

Vita

Jing Li

Jing Li was born in Jinzhou, Liaoning province, China on July 13, 1961. Jinzhou was a county when he was born, became a district of Dalian City later on, and is a city now.

At the age of six and half he left to Heilongjiang province with his family, and he lived there for about 13 years until 1980.

He finished his B.S. degree in 1984 and M.S. degree in 1987 both in Aircraft Engineering at Northwestern Polytechnical University, Xi'an, China.

He was appointed to work as a structural/mechanical engineer from 1987 to 1995, and was the Manager from 1993 to 1995 for the aft-fuselage group in the Department of Structures, Shenyang Aircraft Research Institute, Shenyang, China.

For a new challenge, he came to the USA fall 1995 as an international student. After some ups-and-downs, at the end of 2000, he obtained his M.S. degree in Aerospace Engineering at Virginia Polytechnic Institute and State University, with Dr. Rakesh K. Kapania as his adviser.

One of his major accomplishments in his life took place on May of 1999 in the Town of Blacksburg, Virginia, when he began to believe in God and His Christ Jesus. He was baptized in the Name of the Lord Jesus Christ on July 25, 1999. God delivered him through the lowest valley in his secular life.

From January to July of 2002, he was enrolled at University of Northern Virginia, Manassas, VA, and took 4 courses in Computer Science/Information Systems Technology.

In August of 2002, he got re-admission to the Department of Aerospace and Ocean Engineering, Virginia Polytechnic Institute and State University, to continue his Ph.D program under the supervision of Dr. Rakesh K. Kapania. He finished the defense for his Ph.D degree in Aerospace Engineering by December 1, 2005.

He has been a member of American Institute of Aeronautics and Astronautics.